UNIVERSITY OF OKLAHOMA

GRADUATE COLLEGE

# SEISMIC METHODS APPLIED TO STRUCTURAL INTERPRETATION

A DISSERTATION

SUBMITTED TO THE GRADUATE FACULTY

in partial fulfillment of the requirements for the

Degree of

DOCTOR OF PHILOSOPHY

By

JIANJUN LI

Norman, Oklahoma

2019

SEISMIC METHODS APPLIED TO STRUCTURAL INTERPRETATION

A DISSERTATION APPROVED FOR THE
SCHOOL OF GEOSCIENCES

BY THE COMMITTEE CONSISTING OF

Dr. Shankar Mitra, Chair

Dr. Kurt Marfurt

Dr. Brett Carpenter

Dr. Michael Behm

Dr. Xingru Wu

ACKNOWLEDGEMENTS

First, I would like to thank my advisor Dr. Shankar Mitra. I have been studying with him for more than five years, including two years for the master's degree and the rest for the PhD degree. I really appreciate him for accepting me five years ago and giving me an opportunity to continue my journey on geosciences. He has mentored me in many ways to help me success. Without his support, my PhD career would not be possible. "Five years" sounds like a long time, but it's only a quarter of his career at OU. It is pleasant to work with him, and I really enjoyed my PhD life. Hearing his retirement, I am sorry for those students who did not have a chance to take his classes. A lot of my friends were telling me that they learned a lot in his class. It's my honor to be one of his students, and I will always be his student. I will keep his words in mind and continue learning in my future career.

Next, I would like to thank my dissertation committee members: Dr. Kurt Marfurt, Dr. Brett Carpenter, Dr. Michael Behm, and Dr. Xingru Wu. They were always there when I needed them. They have provided critical comments on my defense and this dissertation. This dissertation would not be in a good shape without them. In addition, I would like to thank other professors who have taught and helped me through my master's and PhD years: Dr. Ze'ev Reches, Dr. Roger Slatt, Dr. Matthew Pranter, Dr. Xiaowei Chen, Dr. Michael Soreghan. I can confidently call myself a geoscientist because of them. And to the department office staffs, thank you for keeping everything working and answering my silly questions.

About my friends, I cannot emphasize enough how important they are. My school life would not be that enjoyable without them. Through these years, I have friends all over the world. It was a mixed feeling to see a lot of my friends graduating previously. On the one

hand, I was happy for them. On the other hand, I knew I would not be able to meet them in person frequently any more. Now I am graduating from the school, it's a different type of mixed feeling. Anyway, I will miss my school because my friends and I had a great time here. Also, to my friends at Aramco in Houston and Chesapeake in OKC, thank you so much for accepting me as an intern and giving me great summers. I am looking forward to my continued career at Chesapeake in the near future. I wish all my friends and their families a beautiful and bright future.

Last but not the least, I want to express my greatest gratitude to my parents: Luo Li and Jun Sun. They have given me everything they can give. They keep supporting me unconditionally. It's painful for parents to send their only kid to study in a totally different country. I have been studying in US for more than seven years. These seven years in US plus two years in Beijing are exchanged for two bachelor's degrees, one master's degree and one PhD degree. I wish they are proud of what I have achieved so far, and I will keep making them proud. Mom and dad, although you can't read this in English right now, I want both of you to know that you are the best parents in the world.

TABLE OF CONTENTS

LIST OF TABLES

LIST OF FIGURES

# ABSTRACT

Seismic modeling and seismic attribute assisted interpretation are conducted to illustrate the use of seismic methods in structural interpretation. Pre-stack time migration (PSTM) seismic modeling is used to study common pitfalls and artifacts associated with the pre-stack time migrated seismic data in common fold-thrust structures. Fault-bend fold models are well imaged but with gentle "pull-ups" due to the lateral velocity variance. Fault - propagation folds exhibit significant footwall "pull-ups" and poor imaging of the steep front limbs. The maximum slip (S) on the fault plays an important role on the dip of the front limbs of trishear fault-propagation folds, and therefore the imaging quality of the front limbs. The fault propagation to slip ratio (P/S ratio) has a lesser influence on the signature of the fault and front limbs. Lateral thickness changes in the high velocity salt or low velocity mobile shale substrate associated with detachment and faulted-detachment folds cause "pull-ups", "push-downs" and other artifacts. The structures seen on the seismic are also sensitive to the accuracy of the root-mean-square (RMS) velocity used for migration, whereby errors in velocity analysis cause distortion in the resulting geometry of the structures.

We also conducted seismic attribute analysis using advanced fault probability attribute on a 3D seismic survey in the Great South Basin, New Zealand. The attribute sharpens the discontinuities associated with polygonal faults which are difficult to interpret due to their complex planiform geometry. Four separate polygonal fault patterns are recognized based on the mechanism of formation and the slope of the faulted units at the time of formation. The formation of the polygonal fault systems in the Great South Basin is related to volume reduction and shear failure due to the opal-A to opal-CT transition within the sediments.

# CHAPTER 1: INTRODUCTION

Seismic imaging of subsurface structures are widely used in the oil and gas industry. Structural interpretation of seismic data is an essential element in exploration and development. Despite the long history of using seismic data to interpret structures, there are still barriers between seismic processing and seismic interpretation. This dissertation studies some seismic methods that can be applied to structural interpretation, including seismic modeling, seismic processing, and seismic attribute analysis.

Seismic modeling and Kirchhoff pre-stack time migration (PSTM) methods are adopted to produce synthetic seismic data which is used to illustrate comparisons between the geological models with time- and depth-migrated seismic data, and to identify and understand the common artifacts and pitfalls associated with the interpretation of natural examples. A series of fold-thrust structures including fault-bend folds, fault-tip fault-propagation folds and trishear fault-propagation folds (Chapter 2), and detachment folds (Chapter 3) (Suppe, 1983; Suppe, 1985; Jamison, 1987; Suppe and Medwedeff, 1990; Mitra, 1990; Erslev, 1991; Mitra, 2002) are modeled. Each style has its own complexities and challenges: fault-bend folds exhibit thrust faults with stair-step trajectories; fault-tip and trishear fault-propagation folds have steep to overturned front limbs; detachment folds are especially challenging because of the involvement of salt or shale substrates in addition to the complex structures. These fold-thrust structures also share a lot of similarities in geometries which lead to difficulties in correctly interpreting them in field seismic data, especially with low signal-to-noise ratios. PSTM seismic modeling methods allow for the evaluation of different structural elements and the testing of velocity errors in the

processing procedure. The comparison with natural examples enables a better interpretation of real seismic data.

Seismic attributes can help interpreters to better visualize the structures. They convert certain seismic signatures like discontinuities into more visible features like coherence (Marfurt et al., 1998). The interpretation of complex 3D structures like polygonal fault systems (PFS) can be assisted by using seismic attributes. An advanced fault probability attribute (Qi et al., 2017), which integrates multiple seismic attributes, is applied to a 3D seismic survey in the Great South Basin, New Zealand (Chapter 4). A detailed structural analysis of the PFS is developed using the attributes analysis results.

Chapter 2 has been published in Interpretation as *Li, J., & Mitra, S. (2019). Seismic Modeling and Expression of Common Fold-Thrust Structures. Interpretation, 8(1), 1-39.*

Chapter 4 has been published in Marine and Petroleum Geology as *Li, J., Mitra, S., & Qi, J. (2020). Seismic analysis of polygonal fault systems in the Great South Basin, New Zealand. Marine and Petroleum Geology, 111, 638-649.*

## REFERENCES


Erslev, E. A. (1991). Trishear fault-propagation folding. Geology, 19(6), 617-620.

Jamison, W. R. (1987). Geometric analysis of fold development in overthrust terranes. Journal of Structural Geology, 9(2), 207-219.

Marfurt, K. J., Kirlin, R. L., Farmer, S. L., & Bahorich, M. S. (1998). 3-D seismic attributes using a semblance-based coherency algorithm. Geophysics, 63(4), 1150-1165.

Mitra, S. (1990). Fault-propagation folds: geometry, kinematic evolution, and hydrocarbon Traps (1). AAPG Bulletin, 74(6), 921-945.

Mitra, S. (2002). Structural models of faulted detachment folds. AAPG bulletin, 86(9), 1673-1694.

Qi, J., Machado, G., & Marfurt, K. (2017). A workflow to skeletonize faults and stratigraphic features. Geophysics, 82(4), O57-O70.

Suppe, J. (1983). Geometry and kinematics of fault-bend folding. American Journal of science, 283(7), 684-721.

Suppe, J. (1985). Principles of structural geology. Prentice Hall.

Suppe, J., & Medwedeff, D. A. (1990). Geometry and kinematics of fault-propagation folding. Eclogae Geologicae Helvetiae, 83(3), 409-454.

# CHAPTER 2: SEISMIC MODELING AND EXPRESSION OF COMMON FOLD-THRUST STRUCTURES


## ABSTRACT

We conducted seismic modeling of common fold-thrust structures to understand the common geological parameters influencing seismic data, and to understand the common pitfalls associated with interpreting pre-stack time (PSTM) and depth (PSDM) migrated data. Mode 1 fault-bend folds are generally well imaged in PSTM data, provided the correct migration velocities are used for the dipping back and front limbs. Seismic pull-ups of the footwall related to lateral velocity variations can result in problems in interpreting the fault geometry and the subthrust area underlying the crest. Fault-tip fault-propagation folds also show significant footwall pull-ups and also show poor to no imaging of the steep front limbs. The geometry of trishear fault-propagation folds is dependent on both the maximum slip on the fault (S) and the fault propagation to slip ratio (P/S ratio). We found that the slip has a strong influence on the dip of the front limb, and therefore the quality of imaging; whereas the P/S ratio, which controls the degree of folding versus thrust faulting, has only a secondary effect. For the front limb, only the area near the synclinal axial plan is well imaged, so that the fault geometry and extent of propagation are typically difficult to interpret. The front limb dips are also sensitive to the accuracy of the RMS velocity model used for migration. Lower velocities result in steeper dipping reflectors, whereas higher velocities result in shallower dips. Pre-stack depth migration generally provides better imaging of the structures; however, both the accuracy and quality of the image are dependent on the velocity models and interpretation derived from the PSTM data.

## Introduction

Seismic imaging of subsurface structures commonly involves common-midpoint stacking (CMP) of reflection data followed by time migration (post-stack time migration) or time migration of gathers preceding the stacking process (pre-stack time migration). The latter approach provides better images and is increasingly used with the availability of more computer power and speed. Both processes result in time sections which contain distortions related to lateral velocity variations within the structure. Interpretation of seismic data must therefore incorporate an understanding of these distortions and the resulting pitfalls. Pre-stack depth migration involves the conversion of data directly to the depth domain before stacking and is the most advanced technique in seismic migration. However, this process of depth conversion is very sensitive to the velocity model, which is itself dependent on the incorporation of a correct geological model of the pre-stack time migration.

The problem of seismic interpretation of time-migrated data is particularly significant for fold-thrust structures which involve complex relationships between folds and thrust faults, significant lateral velocity variations caused by juxtaposition of high velocity against low-velocity units, and the common occurrence of steep bed dips.

In this paper, virtual seismic data produced by 2D seismic forward modeling is used to illustrate comparisons of geological models with the seismic time and depth images, and to identify and understand the common artifacts and distortions associated with seismic data. Fold-thrust belt structures discussed in this study include fault-bend folds, and both fault-tip and trishear fault propagation folds (Suppe, 1983; Suppe, 1985; Jamison, 1987; Suppe and Medwedeff, 1990; Mitra, 1990; Erslev, 1991). The effects of fault geometry,

slip, and propagation distance on the seismic image are also analyzed for trishear folds, along with the sensitivity of the seismic images to the accuracy of velocity picking.

## Common fold-thrust structures

The seismic expression of three types of common fold-thrust structures will be discussed in this study: fault-bend folds (Figure 2.1a), fault-tip fault-propagation folds (Figure 2.1b), and trishear fault-propagation folds (Figure 2.1c).

### *Fault-bend folds*

Fault-bend folding refers to the folding of beds as they pass through bends in faults. The thrust fault follows bedding-parallel detachments in weak units and climbs through more competent units along ramps forming a stair-step trajectory. Movement of the hanging wall over the fault bends results in an anticline-syncline pair (Rich, 1934; Dahlstrom, 1969). Suppe (1983) developed a kinematic model for fault-bend folds, assuming constant line lengths and thicknesses of units. Mode 1 structures are characterized by a flat crest with front limbs that are slightly steeper than the back limbs, whereas mode 2 structures have steeper front limbs.

### *Fault-tip fault propagation folds*

Fault-tip fault-propagation folds form when a thrust fault loses slip and terminates up section by transferring its shortening to a fold developing at the fault tip. The resulting anticline has a gently-dipping back limb and a steep to overturned front limb. It has a tight geometry within the faulted units marked by a single anticlinal axial plane, which branches into two axial planes, forming a flat-topped structure within the unfaulted units. The fault terminates at the frontal synclinal axis of the structure. The fault propagation to slip ratio (P/S ratio) for a fault-tip fold is controlled only by the dip of the ramp (Hardy, 1997). More

complex forms of this structure may result from the breakthrough of faults after the formation of the fault-propagation fold.

Quantitative models for fault-propagation folds can be self-similar or time-variant (Jabbour et al., 2012). Self-similar fault-tip folds (Suppe, 1985) maintain a constant front limb dip and exhibit constant thickness and lengths of beds with progressive evolution. Time-variant fault-tip folds show variable front limb dips with progressive deformation and are associated with thickness variations confined to the front limb (Suppe and Medwedeff, 1990; Jamison, 1987) or in different parts of the structure depending on the stage of evolution (Mitra, 1990).

***Trishear fault-propagation folds***

The trishear model (Erslev, 1991) offers an alternative mechanism for the formation of fault-propagation folds, with slip on the thrust fault dissipated within a triangular deformation zone bounded by an anticlinal and synclinal axial surface. The trishear zone is sheared with progressive deformation and deforms by non-parallel folding and the development of secondary thrust faults. The model requires the transfer of material from the anticlinal to the synclinal axial surface with progressive deformation. The front limb beds generally thicken relative to the back limb in the early stages of evolution, and thin in the late stages. They also steepen with progressive deformation, with stratigraphically higher beds dipping at a lower angle than stratigraphically lower beds at each stage, resulting in a fan-shaped geometry of the beds on the front limb.

The kinematic models of Hardy and Ford (1997) and Almendinger (1998) consider the case of trishear deformation ahead of a planar thrust related to a fault bend fold, with the deformation restricted to unfaulted beds ahead of the fault tip, so that the instantaneous

deformation zone sweeps through the unfaulted beds within a progressively narrowing trishear zone. Brandenburg (2013) developed trishear models for curved faults. His models provide a better fit to some natural examples, such as the Turner Valley Anticline.

The kinematic evolution of trishear folds is non-unique and depends on the slip on the fault and the fault propagation-slip ratio (P/S ratio). If the P/S ratio is constant, the fault length and the width of the back limb increases with increasing fault slip. The front limb experiences thinning, and the dip of the front limb increases. The P/S ratio controls the degree of folding versus faulting in the structure. With increasing P/S ratio, the fault length increases, and the dip of the front limb decreases. The length of the back limb remains constant. For all structures deeper units always have steeper dips than shallower units on the front limb, so that the beds exhibit a fan-shaped pattern.

**Previous seismic modeling studies**

Seismic forward modeling (Withjack and Pollock, 1984; Fagin, 1991; Alaei, 2012) has been used to study the seismic expression of a number of extensional, contractional, and salt structures. There are two commonly used modeling methods: ray-trace modeling and wave-equation modeling. Ray-trace modeling uses ray paths to represent the propagation of the seismic wave front. The advantage of this method is that it saves computing time and shows the association between the reflection points and the shots and receivers (Fagin, 1991). However, it lacks continuity of events especially when the rays along the edge of the structure are hard to capture. Withjack and Pollock (1984) used ray-trace modeling to study the effect of the dip of the fault surfaces and strata, sediment velocities, as well as the fault displacements on the seismic expression of extensional rift structures.

Wave equation modeling studies the propagation and reflection of the wave front and therefore correlates directly to the actual propagation of the seismic waves in natural cases. Morse et al. (1991) used finite-difference acoustic wave-equation modeling to study the seismic expression of the fault-related folds because of the difficulties in tracing rays through the laterally complex models. Alaei and Petersen (2007) also run acoustic wave-equation modeling on a geological model of a regional section from the Zagros fold-thrust belt. They included structural and stratigraphic details in the model and stated that those details enabled better simulation of the data.

## Seismic modeling method

### *Velocity model set up*

Structural models of fault-bend folds (Figure 2.1a), fault-tip fault-propagation folds (Figure 2.1b), and trishear fault-propagation folds (Figure 2.2) were built, and seismic velocities were assigned to the models. The frame of each model is 5000 m long and 3000 m deep. The thickness of all layers is 100 m, except for the bottom two layers which are 200 m and 300 m, respectively. The interval velocity is kept constant along stratigraphic horizons, varying from 2500 m/s for the background velocity to 5300m/s for the deepest layer, so that the velocity increment is 200 m/s between adjacent layers.

The model configuration is kept simple with uniformly thick beds (100 m) maintaining constant velocities which increase progressively with depth. The wavelet frequency is 25 Hz which is standard for high resolution seismic acquisition applied in the field. With that frequency and the interval velocity setup, the vertical resolution $\lambda/4$ is much better than 100 m. Therefore, vertically, the layers can be resolved without tuning effects. In natural examples, the bedding thickness may vary, and the velocity may not be constant within the

layer, adding more complexity to the problem. With layer thinner than $\lambda/4$, the tuning effect will cause constructive or destructive interference between two adjacent bedding reflectors, so that it will be more difficult to connect beds on either side of the thrust fault and correctly interpret on the front limb. Stacking velocity errors will further amplify the tuning problems. In addition, if the acoustic impedance contrast is not as distinct as in the model, stronger reflectors may overshadow dimmer reflectors. All of these factors are important in controlling the quality of the seismic models. However, because the main purpose of this paper is to address the effects of structural geometry and position on the seismic models, the above factors are beyond the scope of the paper and not addressed.

For the fault bend fold model (Figure 2.1a), the dip of the footwall ramp and the back limb is 20°, whereas the dip of the front limb is 23.2° (Mode 1), so that the model is line-length balanced (Suppe, 1983). The fault-tip fault-propagation fold is a line-length balanced self-similar fold (Suppe, 1985), and has an overturned front limb (Figure 2.1b). The dip of the back limb and the footwall ramp is 20°. The fault propagation to slip ratio (P/S ratio) is ramp dip dependent and is 1.7 for this model. The slip is 1000 m, therefore the length of the fault ramp is 1700 m. The sharp bends along axial surfaces are rounded to reduce diffraction artifacts in the seismic model.

For the trishear fault-propagation fold model, the structural geometry is dependent on both the total fault slip (S) as well as the fault propagation/slip ratio (P/S ratio). Therefore, a matrix of five structural models (Figure 2.2) was used with the slip ranging from 1000 meters to 3000 meters (with a constant P/S ratio of 3), and the P/S ratio ranging from 2-4 (with a constant slip of 2000 meters). With increasing fault slip and constant P/S ratio, the fault length increases, and the front limb acquires steeper dips and experiences thinning.

With increasing P/S ratio and a constant slip, the fault length increases, and the front limb dip decreases. In all models, the front limb dips increase for stratigraphically higher units. The sensitivity of the seismic models to the P/S ratio and slip (S) are analyzed by comparing these different models.

***Seismic forward modeling***

2D Seismic forward modeling using Kirchhoff pre-stack time migration (PSTM) is conducted for fault-bend fold and fault-propagation folds (fault-tip and trishear models). The complete workflow of a seismic forward model used in this study involves three major steps (Figure 2.3): forward modeling, developing an average velocity model from the interval velocities, and migration.

The forward modeling requires building a velocity model in depth. The model is polygon based therefore each velocity variance is bounded within a polygon. A simple velocity polygon includes P and S-wave velocity, and density. The velocity models in depth are built, and elastic wave forward modeling is conducted. The shotgathers and wave propagation snapshots are saved for processing and further analysis. The detailed parameters of the elastic wave forward modeling are shown in Table 2.1.

Time migration of the shotgathers needs an RMS velocity model in the time domain. The average velocity in the time domain, which simulates a "perfect" velocity picking process, is used. The shot gathers are migrated and processed using pre-stack time migration with the average velocity in time. After the PSTM, Kirchhoff pre-stack depth migration (PSDM) is also conducted for trishear fault-propagation fold models using the smoothed interval velocity models.

## PSTM results

### *Fault-bend fold*

A Mode 1 fault-bend fold (Suppe, 1983) with gently-dipping front and back limbs is modeled in the study. The PSTM seismic model of the fault-bend fold model shows that every part of the original fault-bend fold structure can be easily recognized in the seismic data (Figure 2.4b). The flat-ramp-flat shape of the fault can be traced although there is some distortion related to the pull-up of the deeper units and the fault, so that the fault appears to be folded. A good fault plane reflector is imaged for a significant part of the fault ramp and upper flat, where there is a strong contrast in interval velocities between the hanging wall and footwall units. Observations of numerous published seismic sections suggest that the fault plan reflectors are usually not well imaged on real data due to the high level of noise (Shaw et al., 2005). Mode 1 fault-bend folds related to steeper ramps, and Mode 2 folds, which form either by transition from fault-propagation or detachment folding to fault-bend folding, or by late-stage rotation of the front limb, will typically show poorer imaging of the steep front limb. These more complex structures were not modeled in the present study.

### *Fault-tip fault-propagation fold*

A self-similar fault-tip fault-propagation fold (Suppe, 1985) was modeled in the study (Figure 2.4d). The PSTM seismic model shows good imaging of the undeformed strata, the back limb, and the transition to the flat crest. The fault ramp is also well imaged because of the contrast between the hanging wall and footwall interval velocities. The front limb of the structure is steep to overturned and results in no imaging and a blank triangular zone.

The “pull-up” effect is also distinct for subthrust strata, particularly under the frontal part of the ramp.

The no-data zone within the front limb of the structure could either be correctly interpreted as steeply-dipping unfaulted beds or as a faulted limb with gentler dips in a natural case (Mitra and Mount, 1998; Shaw et al., 2005). Depending on the accuracy of the velocities and the migration of data along the upper and lower edges of the no-data zone, tails of noise curving upwards along the synclinal axis and downward along the anticlinal synclinal axes may further confuse the interpretation (Onajite, 2014). Time-variant models are characterized by changes in front-limb dip with progressive evolution. Therefore, they may show some variation in the quality of imaging of the front limb.

In the next section, different scenarios for multiple trishear models with different front limb dips and different amounts of fault propagation are discussed to obtain a better standing of the no-data zone on the front limb.

***Trishear fault-propagation folds***

Seismic modeling of five trishear fault-propagation folds with varying P/S ratios and S values is conducted to study the seismic expression of a complete suite of structural possibilities. The angle between the anticlinal and synclinal axial surfaces and the fault were fixed in the models, so the effects of varying apical angles are not considered.

Models 1-3:

Models 1-3 (Figure 2.5) show the seismic expression of trishear structures with increasing slip (1000-3000 m) for a constant P/S ratio of 3. For model 1, the slip is of the hanging wall is 1000 m. Since the P/S ratio is 3, the length of the thrust fault is 3000 m.

The dip of the back limb and the thrust fault ranges from 20° to 30°. The dip of the front limb ranges from 53° to 62°.

The PSTM seismic data of model 1 (Figure 2.5b) shows that the undeformed layers outside the crest and the back limbs are well imaged. The front limb is relatively well imaged for the unfaulted units, except for the steepest dipping segments at the boundary with the hinge, which show dimmed reflections. The faulted units have steeper dips, and this combined with the discontinuities associated with faulting results in poor imaging. The fault is not well imaged and some of the footwall beds are overmigrated. Units under the crest show a distinct pull up due to the contrast in lateral velocities.

In model 2, the slip on the fault is 2000 m, so that the length of the fault is 6000 m (Figure 2.5c). As a result, the back limb is longer, and the dip of the front limb ranges from 65° to overturned.

The PSTM data of Model 2 (Figure 2.5d) shows good imaging of the back limb and the undeformed parts of the model away from the crest of the structure. However, the front limb of the structure shows no reflection because of the high dips of the strata. The "pull-up" effect of this model is more pronounced, because of the greater relief of the structure. The fault is well imaged, but footwall strata appear to be poorly migrated.

Model 3 has a slip of 3000 m, so that the length of the fault is 9000 m. Therefore, it has the longest back limb and greatest relief (Figure 2.5e). The fault breaks through all the layers. The dip of the front limb of the shallowest layer is 80° and most of the beds are overturned. The dip of the back limb ranges from 20° to 42°.

The front limb is not imaged because of the very steep to overturned dips (Figure 2.5f). The fault plane is well imaged but footwall strata under the fault appear to be poorly

migrated and may result in an incorrect interpretation of this zone. The “pull-up” effect is greatest in this model because of the high relief.

Models 4, 2, 5:

Models 4, 2, and 5 have the same slip (2000 m), but varying P/S ratios of 2, 3, and 4 (Figure 2.6a, c, and e). Therefore, the main difference between the geological models is the extent of fault propagation, which in turn results in different amounts of folding versus faulting.

The PSTM models (Figure 2.6b, d, and f) show very little difference in the imaging of the front and back limb, as well as the footwall strata under the fault. The modeled fault has a shorter length in model 4 than 2 and 5, but, 2 and 5 show about the same fault length. This is because the velocity contrast across the fault is not significantly different from that across an overturned limb and underlying gently dipping beds for the same amount of fault slip.

Wave propagation analysis:

Figure 2.7 includes two snapshots of wave propagation together with the shot gathers for different shots of Model 2. For each case, the left is the snapshot, while the right is the shot gather. From the snapshot, it is possible to trace the propagation of the wave front and where the reflections in the shotgather come from. These images show that the front limb is not imaged well, because there is insufficient energy bounce back from the beds, and the waves are reflected back from the front limb at low angles, so the receivers do not record them. In the shot gather, we can see wide low amplitude zones for front limb reflections. On the other hand, the reflections from the back limb are quite strong and are recorded by the receivers, since the dip of the back limb is smaller than the front limb.

Summary of trishear models and interpretation implications:

The matrix of trishear models with varying slip and P/S ratios provide a representative suite of models for summarizing the imaging of these structures with PSTM processing. The back limbs with their relatively low dips and the undeformed parts of the structure away from the anticlinal crest are relatively well imaged.

The front limb which is marked by the axial surfaces which bound the trishear zone is generally poorly imaged because of steep dips. The dips of the beds are primarily determined by the slip on the fault, and only secondarily by the P/S ratio. Therefore, trishear folds with small amounts of fault slip show better imaging of the front limb than those with large amounts of fault slip, for a constant P/S ratio. Furthermore, the quality of imaging decreases with increasing depth because of the beds dip more steeply in deeper units. The P/S ratio controls the dips of the front limb to a lesser extent, so there are limited changes in the seismic images for different P/S ratios for a constant fault slip.

Fault reflections are segmented because there are no velocity differences across the fault for parts of the fault. The reflection coefficient is negative for the fault reflections compared to the bedding reflections because they involve a decreasing velocity. The reflectors are longer and more continuous with higher P/S ratios.

A “fault shadow” is commonly referred to as the zone of unreliable seismic imaging under faults (Fagin, 1996; Hatchell, 2000). The footwalls of the faults are poorly imaged because of the fault shadow effect. The reflectors in these areas are commonly overmigrated and can lead to incorrect interpretations of the footwall geometry. The bounding axial surfaces of the trishear zones are marked by sharp dip changes. As a result, tails of incorrectly migrated reflectors are present in these zones and can lead to errors in

the interpretation of front limb dips. All models are marked by a pull up under the fold crest caused by lateral variations in velocity. The magnitude of the pull up is greatest for faults with the largest slip.

***Velocity error analysis***

The velocity spectrum method is a common way to pick stacking velocities for pre-stack time migration. The CMP gather transformed from offset in the two-way time domain to the stacking velocity in the two-way zero-offset time domain (Taner and Koehler, 1969). Each trace in the velocity-stack gather is a stack of the traces in the CMP gather using a constant-velocity normal moveout (NMO) correction (Yilmaz, 2001). The velocity that should be used to stack the event in the input CMP gather is highlighted with a stacked amplitude in the spectrum. For real data, when the signal-to-noise ratio of the input data is low, the stacked amplitude may not show clear results, hence it is harder to estimate the correct stacking velocity.

In this study, the program generated average velocities producing the "perfect" stacking velocity picks. Changing the interval velocity model in depth will alter the average velocity model. Two types of stacking velocity error scenarios are investigated (Figure 2.8). The first type considers that the velocity error occurs within a vertical band between 2000 m and 2600 m (Figure 2.8b), which approximates the front limb of the structures and extends to the undeformed beds in the footwall. Interval velocities were modified to be 20% higher or lower, so that the maximum average velocity error is 15% higher or lower (Figure 2.8a: red and green lines). The second type is that the velocity error only occurs within the trishear zone (Figure 2.8c), therefore the average velocity error is confined to a triangular zone. The maximum average velocity error is between 5 and 10 % (Figure 2.8a: purple and

blue lines), because deeper beds outside the trishear zone maintain their original interval velocities. This case is based on the assumption that the signal to noise ratio is typically lowest within the steeply dipping trishear zone.

In processing of real data, the velocity error may not be as high and the boundary marking the change will likely not be as sharp. The seismic model shows the extreme scenario to better illustrate the influence of the velocity error.

For both the vertical and trishear PSTM models (Figure 2.9a and d), higher velocities result in the horizons close to the synclinal axis being pushed down clockwise so that the dips are shallower than the correctly migrated result (Figure 2.9b). The effect of the velocity increase on the front limb appears to be more pronounced than the effect on the horizontal layers underneath it. The offset of reflectors along the boundaries of the error zone is not clearly visible because of the poor quality of the data between the crest and the steeply dipping front limb. For better imaged front limbs, incorrectly estimated high velocities on the front limb may results in an apparent offset of reflectors leading to an incorrect interpretation of the fault tip especially in the deeper units.

This results in a common problem of estimating the extent of fault propagation for structures with steep front limbs, including trishear fault-propagation folds and faulted detachment folds. An incorrect interpretation of the location of the fault tip can result in variations in the closed volume under the structure and the related hydrocarbon reserves, as demonstrated in an example from the Niger Delta (Kostenko et al., 2008).

Lower velocities (Figure 2.9c and f) results in the front limb reflectors lifted counterclockwise, so that the dip of the front limb appears steeper. The gap between the front limb slope and the underlying horizontal layers is larger.

In conclusion, the tilted layers on the front limb in our models have higher dips when the velocity is lower and lower dips when the velocity is higher. The horizontal layers are not affected by the velocity error significantly. Apparent offsets between the crest and front limb may result in an incorrect interpretation of a fault, especially in the deeper units.

**PSDM modeling of trishear fault-propagation folds**

PSTM modeling was followed by pre-stack depth migration (PSDM) modeling of the same trishear suite (Figure 2.10). The velocity models used for PSDM in this study are original interval velocity models after smoothing. In general, the seismic model matches the geological model well, because the input velocity model for the pre-stack depth migration is known and therefore "perfect". Some of the issues with pre-stack time migration such as "pull-up" effects and fault shadows are solved in the PSDM image. However, weak reflections in PSTM results, are also reflected in the PSDM results because the data was not recorded by the receivers.

In natural examples, the velocity model built in depth is based on PSTM results. Since the PSTM results may not be good in poorly imaged areas such as the front limb, the velocity model built from it would be less reliable. Eliminating the "pull-up" effect and fault shadows will enable a better interpretation of the actual geometry of the structure and the fault. However, PSDM images are strongly dependent on an accurate PSTM interpretation.

**Conclusions**

PSTM seismic modeling shows the quality of imaging that can generally be obtained for common fold-thrust structures and the common structural positions which display

relatively poor imaging. This approach provides a seismic interpreter with information about common pitfalls of interpreting seismic data for these structures.

Mode 1 fault-bend folds are generally well imaged, provided the correct migration velocities are used for the dipping segments. Seismic pull-ups can result in some ambiguities in interpreting the fault geometry as well as the footwall beds underlying the flat crest of the structure. Fault-tip fault propagation folds show not only strong pull up effects underlying the structure, but very poor to no data from the steep front limb of the fold.

The geometry of trishear fault-propagation folds is dependent on both the maximum slip on the fault (S) and the fault propagation to slip ratio (P/S ratio). Our studies show that the slip has a strong influence on the dip of the front limb, so that partial imaging of the front limb is only obtained for low slip values, whereas high slip values result in no imaging of the front limb. The P/S ratio also influences the front limb dip by controlling the extent of folding versus faulting, but these effects are usually secondary compared to the amount of slip. It is generally difficult to determine the extent of fault propagation for all trishear folds, because it is difficult to distinguish velocity contrasts across faults and steep dipping segments. The imaging of the front limb is also sensitive to the accuracy of the stacking velocity. Lower velocities typically result in steeper dipping reflectors, whereas higher velocities result in shallower dips. Inaccurate velocity estimates can therefore lead to both an inaccurate interpretation of the structure and estimates of the fault slip and propagation.

Pre-stack depth migration generally produces better imaging of the structures, provided the velocity models are accurate. The quality of the PSDM images are strongly dependent on the PSTM models, both because the imaging of segments with poor data in PSTM is

not improved by using depth migration, and because the velocity models are obtained based on interpretation of the PSTM data.

**Acknowledgments**

All synthetic models were constructed and imaged using Tesseral Pro.

## CHAPTER 2 TABLES

| Wave form | Frequency | Sources No. | Receivers No. | Source interval | Receiver interval |
|---|---|---|---|---|---|
| Ricker | 25 Hz | 201 | 401 | 25m | 12.5m |

Table 2.1 The detailed parameters of the elastic wave forward modeling.

**CHAPTER 2 FIGURES**

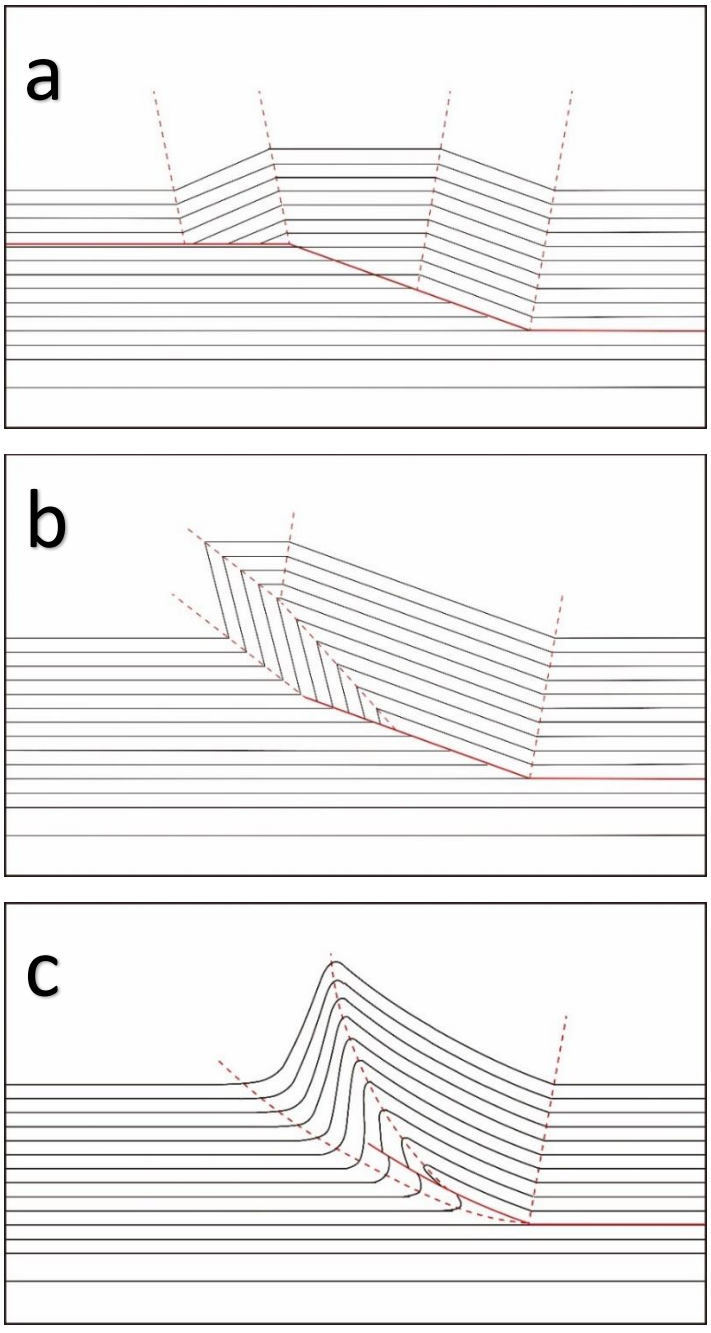


Figure 2.1. Three common fold-thrust belt models: (a) fault-bend fold (Mode 1); (b) fault-tip fault-propagation fold (self-similar); (c) trishear fault-propagation fold. Fault surfaces are shown in red solid lines. Axial surfaces are shown in red dashed lines.

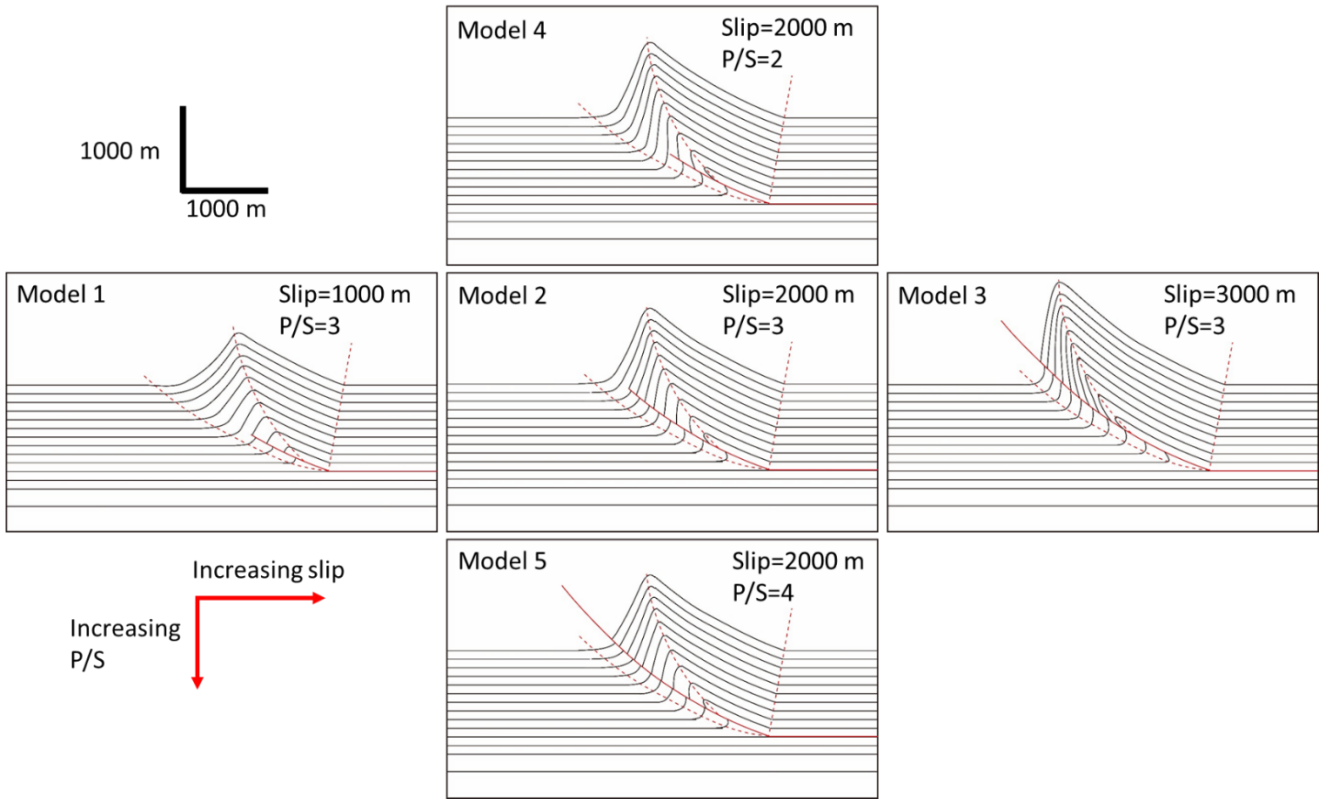


Figure 2.2. Trishear fault-propagation fold models. Fault planes are shown in red solid lines. Axial surfaces are shown in red dashed lines. From the left to the right, the fault slip increases from 1000 m for Model 1 to 3000 m for Model 3. From the top to the bottom, the P/S ratio is increases from 2 for model 4 to 4 for model 5.

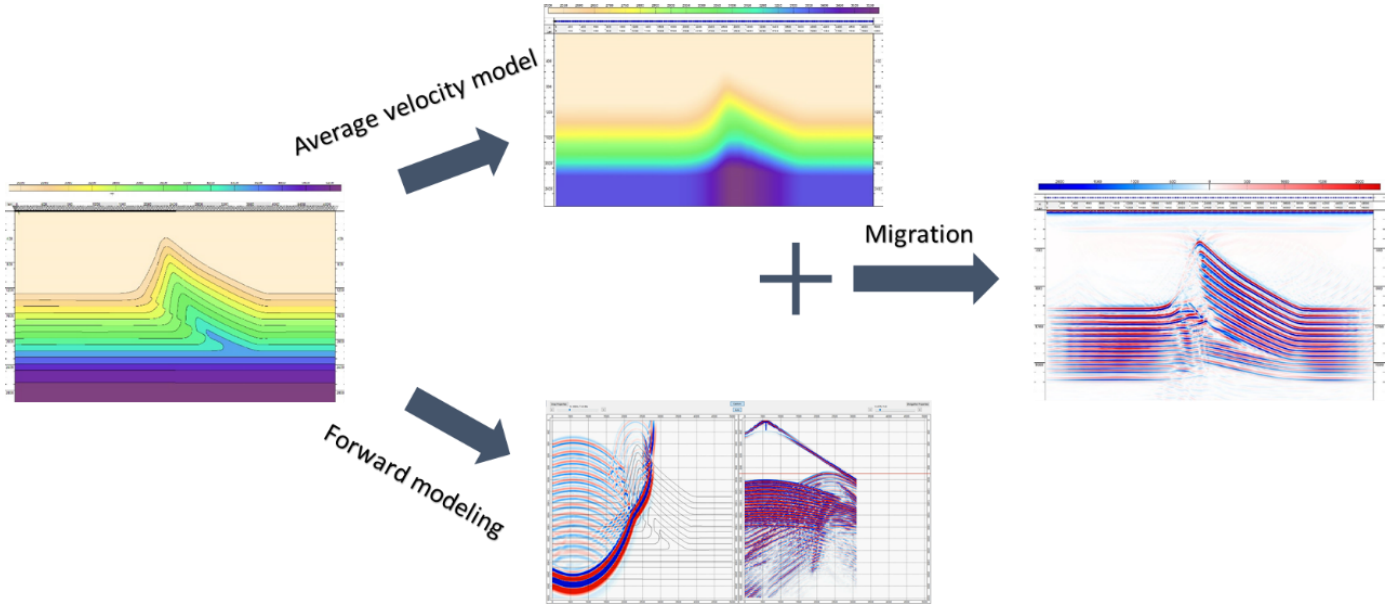


Figure 2.3. A workflow showing the key steps in the seismic forward modeling method used in this study: forward modeling, development of average velocity model in time, and migration.

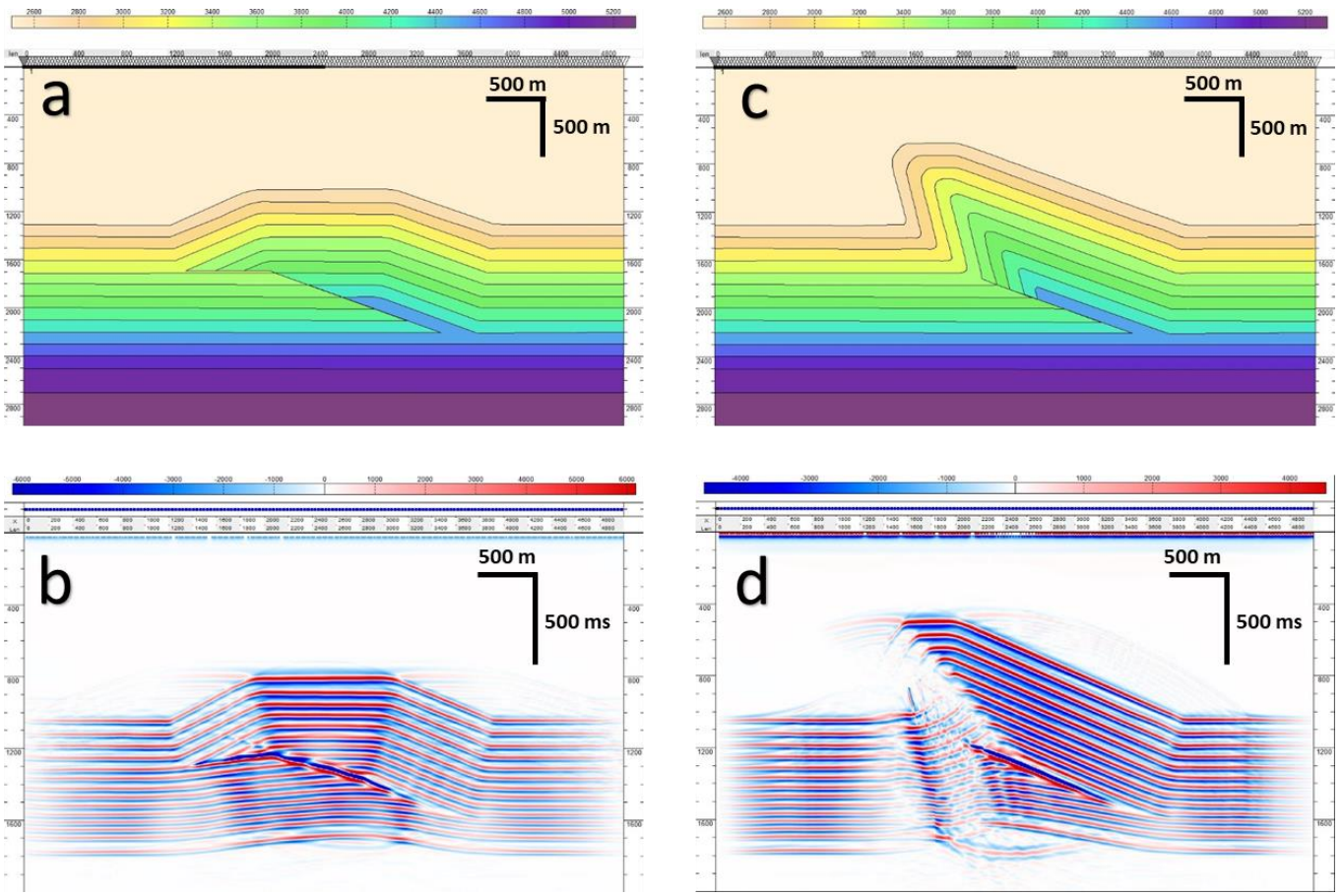


Figure 2.4. Velocity models of fault-bend fold (a) and fault-tip fault-propagation fold (c). Vertical and horizontal axes are in meters (m). PSTM results of fault bend fold (b) and fault-tip fault-propagation fold (d). The vertical axis is in milliseconds (ms).

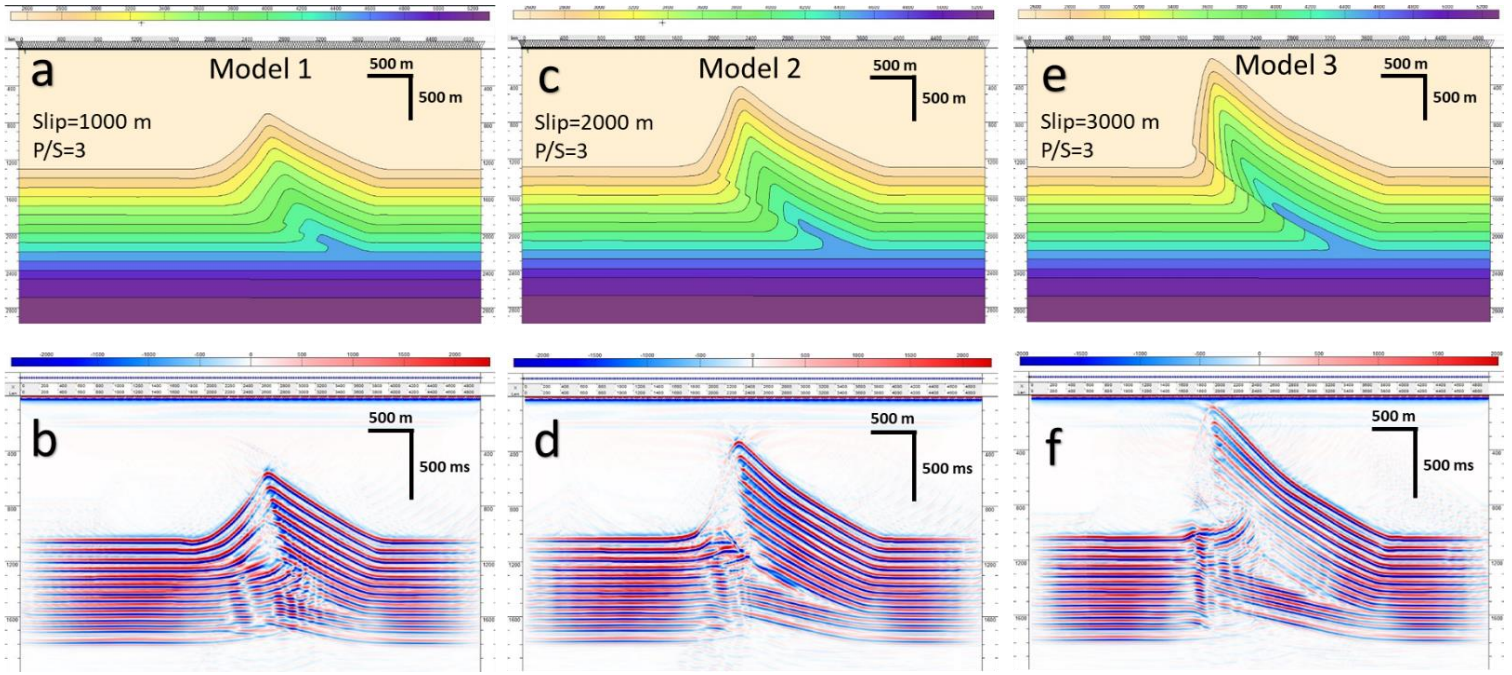


Figure 2.5. Trishear fault-propagation fold models with constant P/S ratio (P/S = 3). Velocity models of Model 1 (a), Model 2 (c), and Model 3 (e). Vertical and horizontal axes are in meters (m). PSTM results of Model 1 (b), Model 2 (d), and Model 3 (f). The vertical axis is in milliseconds (ms).

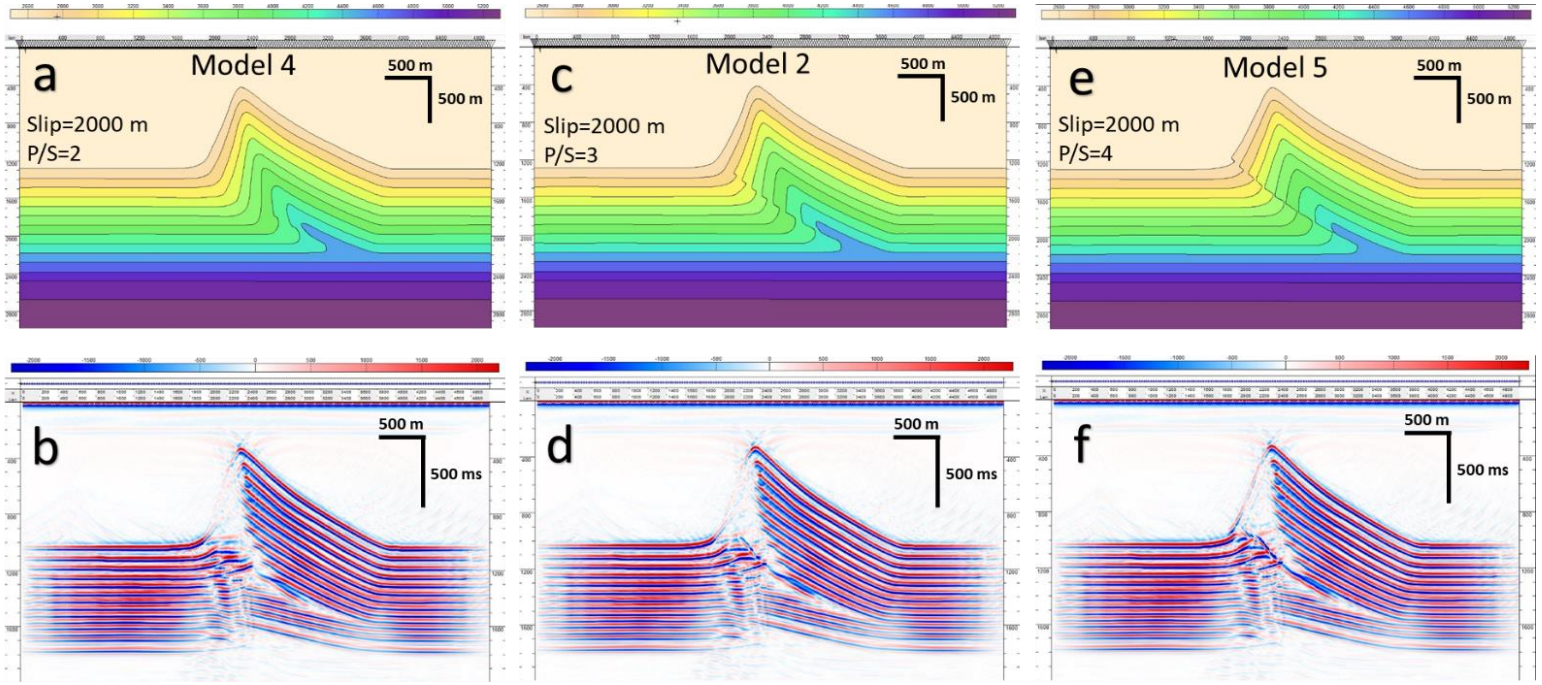


Figure 2.6. Trishear fault-propagation fold models with constant slip (2000 m). Velocity models of Model 4 (a), Model 2 (c), and Model 5 (e). Vertical and horizontal axes are in meters (m). PSTM results of Model 4 (b), Model 2 (d), and Model 5 (f). The vertical axis is in milliseconds (ms).

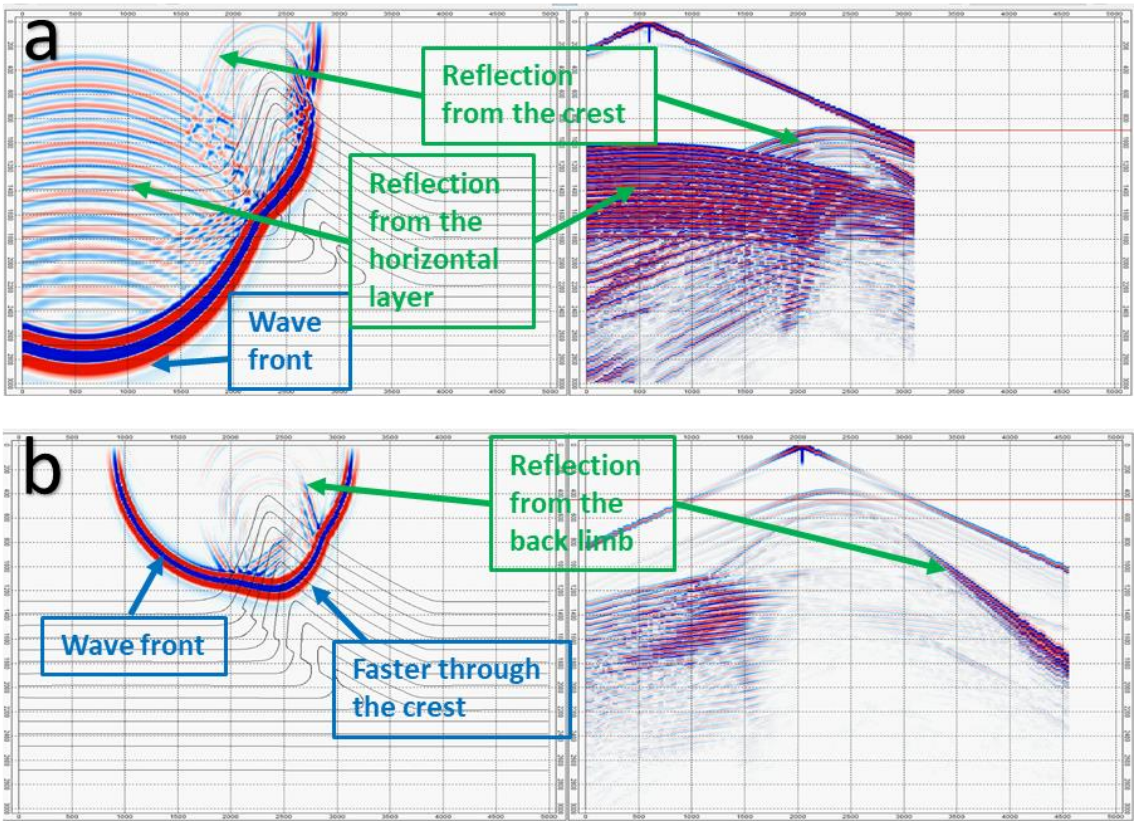


Figure 2.7. Snapshots of wave propagation and shot gathers: (a) left: snapshot at 0.9 sec of shot at 600 m, right: shot gather of shot at 600 m; (b) left: snapshot at 0.45 sec of shot at 2050 m, right: shot gather of shot at 2050 m.

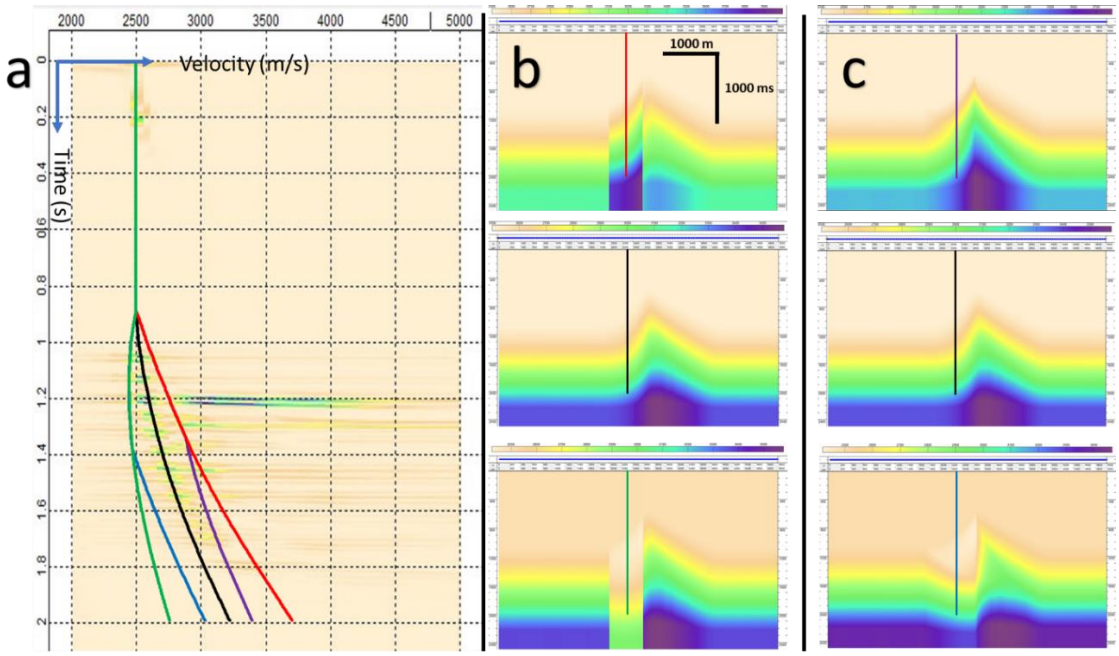


Figure 2.8. Two types of velocity error scenarios. (a) the velocity spectrum showing the concept of higher (red line) or lower (green line) velocity picking within 2000-2600 m band, higher (purple line) or lower (blue line) velocity picking within trishear zone, and correct velocity picking (black); (b) average velocity models with incorrect velocity picks within 2000-2600 m band; (c) average velocity models with incorrect velocity picks within trishear zone. The correct average velocity model is in the middle. The horizontal axis is in meters (m). The vertical axis is in milliseconds (ms).

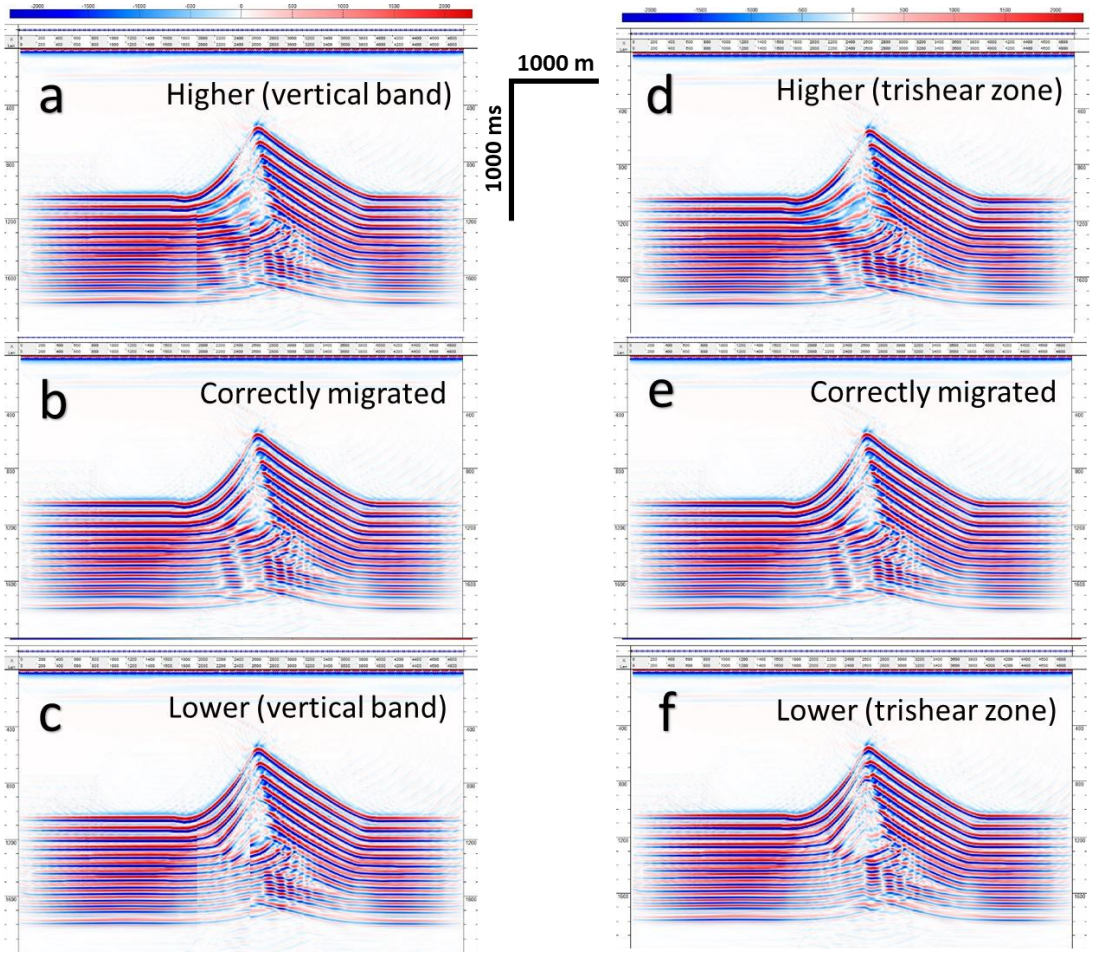


Figure 2.9. PSTM results of Model 1 migrated with different average velocity models shown in Figure 2.8.

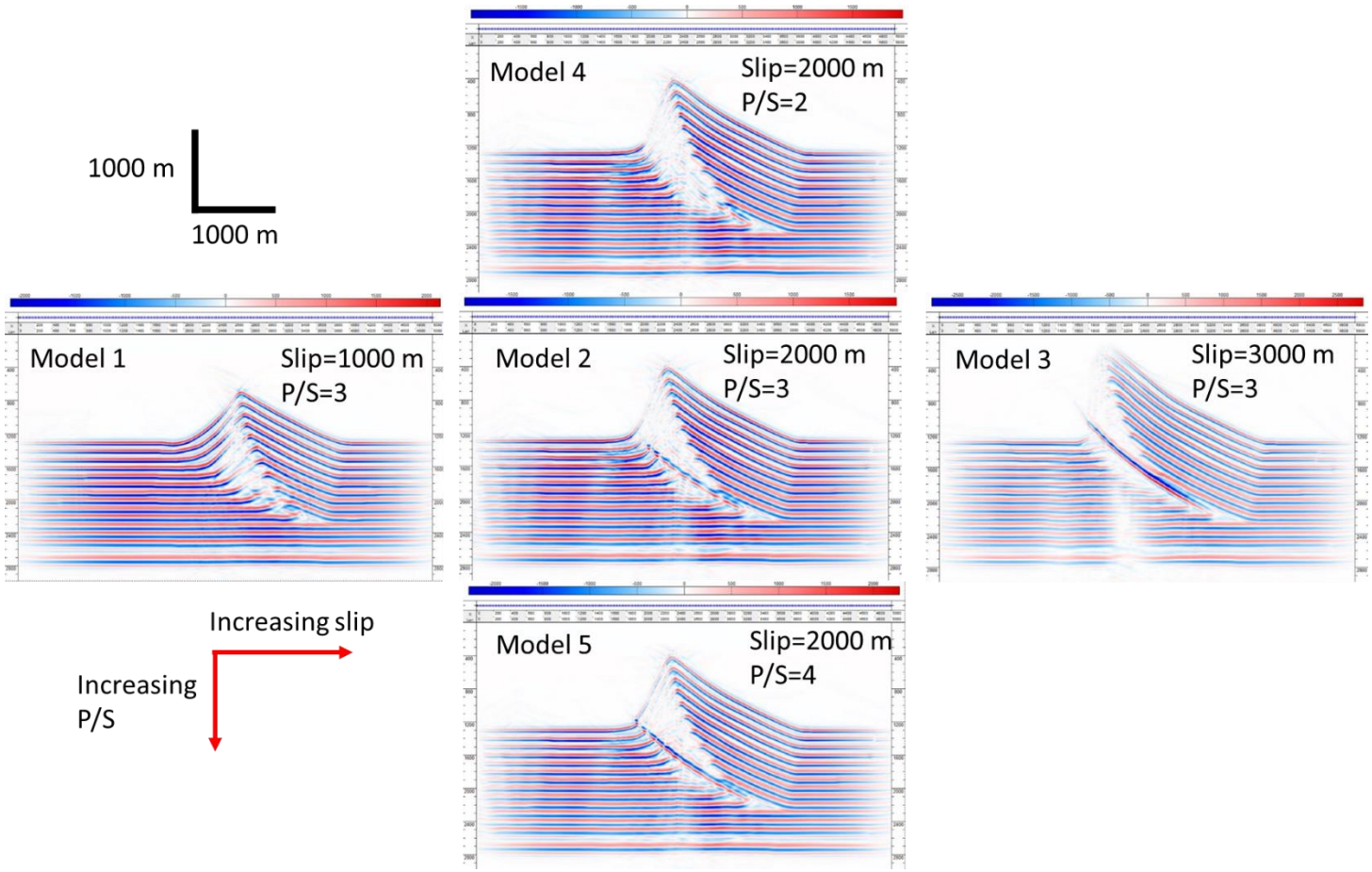


Figure 2.10. PSDM results of trishear fault propagation fold models

## REFERENCES


Alaei, B., & Petersen, S. A. (2007). Geological modelling and finite difference forward realization of a regional section from the Zagros fold-and-thrust belt. Petroleum Geoscience, 13(3), 241-251.

Alaei, B. (2012). Seismic modeling of complex geological structures. Seismic Waves-Research and Analysis. InTech, 213-236.

Allmendinger, R. W. (1998). Inverse and forward numerical modeling of trishear fault-propagation folds. Tectonics, 17(4), 640-656.

Brandenburg, J. P. (2013). Trishear for curved faults. Journal of Structural Geology, 53, 80-94.

Dahlstrom, C. D. A. (1969). Balanced cross sections. Canadian Journal of Earth Sciences, 6(4), 743-757.

Erslev, E. A. (1991). Trishear fault-propagation folding. Geology, 19(6), 617-620.

Fagin, S. W. (1991). Seismic modeling of geologic structures: Applications to exploration problems. Society of Exploration Geophysicists.

Fagin, S. (1996). The fault shadow problem: Its nature and elimination. The Leading Edge, 15(9), 1005-1013.

Hardy, S. (1997). A velocity description of constant-thickness fault-propagation folding. Journal of Structural Geology, 19(6), 893-896.

Hardy, S., & Ford, M. (1997). Numerical modeling of trishear fault-propagation folding. Tectonics, 16(5), 841-854.

Hatchell, P. J. (2000). Fault whispers: Transmission distortions on prestack seismic reflection data. Geophysics, 65(2), 377-389.

Jabbour, M., Dhont, D., Hervouët, Y., & Deroin, J. P. (2012). Geometry and kinematics of fault-propagation folds with variable interlimb angle. Journal of Structural Geology, 42, 212-226.

Jamison, W. R. (1987). Geometric analysis of fold development in overthrust terranes. Journal of Structural Geology, 9(2), 207-219.

Kostenko, O. V., Naruk, S. J., Hack, W., Poupon, M., Meyer, H. J., Mora-Glukstad, M., ... & Mordi, M. (2008). Structural evaluation of column-height controls at a toe-thrust discovery, deep-water Niger Delta. AAPG Bulletin, 92(12), 1615-1638.

Mitra, S. (1990). Fault-propagation folds: geometry, kinematic evolution, and hydrocarbon Traps (1). AAPG Bulletin, 74(6), 921-945.

Mitra, S., & Mount, V. S. (1998). Foreland basement-involved structures. AAPG bulletin, 82(1), 70-109.

Morse, P. F., Purnell, G. W., & Medwedeff, D. A. (1991). Case History 4. Seismic Modeling of Fault-Related Folds. In Seismic Modeling of Geologic Structures: Applications to Exploration Problems (pp. 127-152). Society of Exploration Geophysicists.

Onajite, E. (2014). Chapter 12-Understanding Seismic Migration. In Seismic Data Analysis Techniques in Hydrocarbon Exploration (pp. 153-174). Elsevier

Rich, J. L. (1934). Mechanics of low-angle overthrust faulting as illustrated by Cumberland thrust block, Virginia, Kentucky, and Tennessee. AAPG Bulletin, 18(12), 1584-1596.

Shaw, J. H., Connors, C. D., & Suppe, J. (Eds.). (2005). Seismic interpretation of contractional fault-related folds: An AAPG seismic atlas (Vol. 53). American Association of Petroleum Geologists.

Suppe, J. (1983). Geometry and kinematics of fault-bend folding. American Journal of science, 283(7), 684-721.

Suppe, J. (1985). Principles of structural geology. Prentice Hall.

Suppe, J., & Medwedeff, D. A. (1990). Geometry and kinematics of fault-propagation folding. Eclogae Geologicae Helvetiae, 83(3), 409-454.

Taner, M. T., & Koehler, F. (1969). Velocity spectra—Digital computer derivation applications of velocity functions. Geophysics, 34(6), 859-881.

Withjack, M. O., & Pollock, D. D. (1984). Synthetic seismic-reflection profiles of rift-related structures. AAPG Bulletin, 68(9), 1160-1178.

Yilmaz, Ö. (2001). Seismic data analysis: Processing, inversion, and interpretation of seismic data. Society of exploration geophysicists.

# CHAPTER 3: SEISMIC MODELS OF DETACHMENT AND FAULTED DETACHMENT FOLDS


## ABSTRACT

Detachment folds constitute a common structural style in fold-thrust belts and typically from in stratigraphic packages defined by relatively competent cover units underlain by ductile units. PSTM images through these structures display complexities resulting from significant lateral velocity variations between the cover sediments and the core units, steep dips, and complex fold-fault relationships, making them difficult to interpret. We conducted 2D seismic modeling for a number of detachment fold models to study the effect of these complexities on PSTM data. Seismic "pull-ups" and "push-downs" of the strata underneath the salt or shale substrate are related to the relative velocities of the cover sediments and the core units. A specific example of an Appalachian Plateau structure demonstrates how the relative velocities can influence the seismic image. Progressive evolution of the structures to disharmonic and lift off folds results in enhanced "pull-ups" and poorer imaging of steep limb segments. For faulted detachment folds, the limbs around the fault are poorly imaged and marked by wide low-reflectivity bands, making fault interpretation difficult. Footwall zones are also poorly imaged. Understanding these artifacts and pitfalls in PSTM seismic models enables improved interpretations of PSTM data in natural structures.


## Introduction

Kirchhoff pre-stack time migration (PSTM) is commonly adopted in the seismic imaging of subsurface structures. It provides better images compared to post-stack time migration, however, it still has some inherent issues that time migration is not capable of

solving. Compared to Kirchhoff pre-stack depth migration (PSDM), PSTM time sections contain distortions related to lateral velocity variations when imaging complex structures with steep dips. Therefore, a good understanding of these inherent artifacts and the resulting pitfalls is critical when interpreting the PSTM seismic sections.

Detachment folds constitute a common structural style in both onshore and deepwater fold and thrust belts. They typically form in stratigraphic packages defined by a relatively competent package overlying a ductile unit, and progressively evolve from simple low amplitude structures to disharmonic detachment folds and lift-off folds. Faulting in the later stage of deformation is also common. The seismic interpretation of PSTM data is particularly challenging for detachment fold structures that involve complexities like significant lateral velocity variations caused by a salt or shale detachment core, overburden strata, steep dips, and relationships between folds and thrust faults (Jones and Davison, 2014). The interpretation of salt or shale cored detachment fold structures influences the exploration and development of a hydrocarbon-bearing basin by affecting the trap definition, seal capacity, reservoir quality, migration and drilling hazards (Wiener et al., 2010).

The objective of this paper is to use synthetic seismic data of multiple detachment fold geological models produced by 2D seismic forward modeling to demonstrate the common artifacts and pitfalls associated with the PSTM data of detachment fold structures. We specifically focus on the effects of the seismic velocity of the cover sediments and core units, the evolution of the structure, and the fold-fault relationships.

**Detachment and faulted detachment folds**

Detachment folds (Mitra, 2003) comprise one of the three main types of structural styles in fold-thrust belts (Jamison, 1987). They typically form in sedimentary units characterized by strong thickness and competency contrasts, in which the basal incompetent layer is commonly salt and shale, and covering competent layers are carbonates or clastic rocks (Jamison, 1987; Mitra, 2002, 2003).

Detachment folds have been documented in a variety of fold belts, including the Appalachian fold belt (Mount, 2014; Gillespie and Kampferk, 2017), the Jura Mountains (Buxtorf, 1916; Laubscher, 1962), the Zagros fold belt (Stocklin, 1968; McQuarrie, 2004), the Perdido and Mississippi Fan fold belts of Gulf of Mexico (Rowan, 1997; Trudgill et al., 1999; Camerlo and Benson, 2006), and the Niger Delta (Briggs et al., 2006; Kostenko et al., 2008; Wiener et al., 2010). Numerous physical modeling experiments have been conducted to investigate the kinematics of thin-skinned fold-thrust belts above ductile detachments (Letouzey et al., 1995; Cotton and Koyi, 2000; Costa and Vendeville, 2002; Vidal-Royo et al., 2009; Li and Mitra, 2017). The natural examples and the experimental modeling show that detachment folds can be generally more symmetric than other fold forms in fold belts like fault-bend and fault propagation folds, particularly in the early stages of evolution (Mitra, 2003). Opposite vergences are common both along and across trend, and fold asymmetry and faulting might occur later due to variations in the mechanical stratigraphy and pre-existing structure.

Detachment folds can be described in terms of geometries of two main types: disharmonic detachment folds (De Sitter, 1964), and lift-off folds (Namson, 1981; Mitra and Namson, 1989). These geometric types represent different stages of the same

evolutionary process (Mitra, 2003). Figure 3.1 shows the evolution of a symmetric detachment fold. With evolution, the fold wavelength decreases, while the amplitude increases. Although the large anticlinal area resulted by the formation is greater than the shortened area, the missing area can be compensated by the downward deflection of the synclines (Dahlstrom, 1990; Mitra, 2003). The area balancing of the detachment fold is achieved with the anticlinal area above the regional position of each unit (A1) equal to the sum of the shortening area (A4) and the synclinal areas (A3, A4). Dahlstrom (1990) proposed a model for detachment folding without any synclinal downwarp. Such folds can develop if the structure initiates with a low wavelength/amplitude ratio.

The above model describes the simplest case of symmetric detachment folding without significant faulting. Variations in the geometry of detachment folds from the above model include (1) fold asymmetry, (2) faulting, which initiates in the most highly strained structural positions and can affect one or both limbs, and (3) the presence of multiple detachments, resulting in changes in the geometry and vergence of the structure in the different stratigraphic packages.

Natural examples of seismic time profiles through detachment folds display a number of artifacts that can result in problems or ambiguities in interpreting these structures. These include seismic “pull-ups” and “push-downs” below the basal detachment, poor imaging of steep limbs, parallel bands of no data zones that can be alternatively interpreted as faults or kink bands, and ambiguities regarding the nature of the main fault zone. The comparison of seismic models and natural examples can provide insights into resolving these problems.

## Seismic modeling method

### *Seismic modeling workflow*

Seismic forward modeling methods, including ray-trace modeling (Withjack and Pollock, 1984; Fagin, 1991) and wave-equation modeling (Morse et al., 1991; Alaei and Petersen, 2007; Li and Mitra, 2019), have been used to study the seismic expression of several extensional, contractional, and salt structures. These modeling methods use ray paths or wave equations to simulate the propagation of the seismic waves.

In this study, 2D wave-equation seismic forward modeling followed by Kirchhoff pre-stack time migration (PSTM) is conducted for a series of detachment fold models. The complete workflow of a seismic forward model used in this study involves three major steps (Figure 3.2): wave-equation forward modeling, Root Mean Square (RMS) velocity analysis, and PSTM.

The forward modeling method we use requires building a polygon-based velocity model in depth. Each velocity variance is bounded within a polygon. A simple velocity polygon includes P-wave velocity and density. After the velocity models in depth are built and the acquisition parameters are set-up, the acoustic wave forward modeling is conducted. The shotgathers are used for later processing.

Interactive velocity analysis and stacking velocity picking processes are carried out to approximate the RMS velocity which is needed for PSTM. Figure 3.2c shows an example of the velocity analysis panel. The figure to the left shows the velocity spectrum panel where the stacking velocity was picked, whereas the right shows the correlating offset gather after normal-move-out (NMO). In the spectrum panel, the velocity that is used to stack the event in the input CMP gather is highlighted with a stacked amplitude.

Pre-stack time migration (PSTM) is a migration technique that is applied before the stacking process. It provides better images for complex structures than post-stack time migration. It is conducted onto the common mid-point sorted shotgathers with the RMS velocity model.

***Velocity model set up***

Seismic modeling of a variety of detachment folds is conducted using a series of controlled experiments. We first construct models that explore the effects of the overburden lithology by considering three separate possibilities: a clastic package with progressively increasing velocities with depth (Figure 3.3a), a carbonate package with progressively increasing velocities with depth, but with velocities higher than for the clastic units (Figure 3.3c), and a hybrid package made up of clastic rocks overlying carbonates (Figure 3.3e). We also consider the effects of the lithology of the core units, by replacing salt with overpressured shale, which has a lower seismic velocity (Figure 3.4c). The effects of overburden lithology and that of the core units are examined only for early stage symmetric detachment folds with a high wavelength/amplitude ratio. Finally, we develop models that explore the effects of the stages of evolution of a symmetric detachment fold as manifested in the final geometry, maintaining a constant overburden lithology made up of clastic units overlying higher velocity carbonate units (Figure 3.5). The core unit is salt with a constant velocity and originally constant thickness.

All of the above models use the same model frame which is 20000 m long and 6500 m deep. The thickness of the ductile layer (salt or shale) before the deformation is 900 m. The thickness of the competent layers above and below the salt is 300 m. The salt velocity is 4600 m/s. The seismic velocity for the overpressured shale used in this study ranges from

2800 m/s at the top to 3000 m/s at the bottom. In terms of the covering competent layers (14 layers), the seismic velocities of the clastic rocks range from 2900 m/s to 4100 m/s based on the depth. The carbonate velocities range from 5000 m/s to 6000 m/s. The velocity interval between two adjacent layers varies from 70 m/s to 100 m/s. The sediments below the detachment share the same seismic velocities among all the models. The velocities of them (5 layers) range from 5000 m/s to 5800 m/s with an increment of 200 m/s. A separate model for the Liberty anticline in the Appalachian Plateau with known structural geometry and seismic velocity information is built to study the effects of overburden and core lithology (Figure 3.6).

The second series of models examine the effects of asymmetry, faulting on both the front and back limbs, and curved vs. angular fold geometries. These are based on the kinematic models of detachment and faulted detachment folds described by Mitra (2002, 2003). The frame for these models is 15000 m long and 6200 m deep (Figure 3.7). The salt velocity is 4600 m/s. The cover layers use the lithology combination of the clastic rocks (9 layers) at the top (3800 - 4600 m/s) and carbonates (4 layers) at the bottom (5500 - 5800 m/s) with an increment of 100 m/s. The growth units above the structure have the velocity gradually changing from 2700 m/s to 3600 m/s with depth. The three layers below the salt have the velocities ranging from 5600 m/s to 6000 m/s with an increment of 200 m/s.

The acquisition parameters are the same for all the models. The source interval is 300 m while the receiver interval is 50 m. The wavelet form is Ricker wave (Figure 3.2). The wavelet frequency is 30 Hz which is standard for high-resolution seismic acquisition and high enough for resolving all the layers in our models vertically.

**Effects of seismic velocities of overlying sediments**

Three models were run to study the effects of the seismic velocities of the cover sediments, with salt as the core unit. These included (1) a clastic sedimentary cover with velocities lower than salt, (2) a carbonate cover with velocities higher than the salt, and (3) a hybrid cover with clastic rocks overlying carbonates. All models apply to early stage low-relief detachment fold with a high wavelength/amplitude ratio.

The first model with a clastic sedimentary cover (Figure 3.3a), the sediments have velocities ranging from 2900 m/s to 4100 m/s, whereas the salt has a constant velocity of 4600 m/sec. The velocities of the five layers underlying the salt range from 5000 m/s to 5800 m/s with an increment of 200 m/s. The PSTM result of the model reproduces the general geometry of the structure (Figure 3.3b), and all parts of the structure can be easily recognized in the PSTM data. The top and bottom surfaces of the salt are showing positive reflectivities. The horizons below the salt in PSTM data are not flat as in the structure model. Under the anticline where the salt is thicker, the horizons under the salt are pulled up to an anticlinal geometry. This "pull-up" effect is caused by lateral variation in velocity since the average velocity for the anticline is higher than the synclines. A simple approximate velocity contrast can be obtained by comparing the salt velocity (4600 m/s) with the velocities of shallow layers in the synclines (2900 – 3200 m/s), which are not present above the anticline. Depth conversion using the correct velocities will remove the "pull-up" effect.

The second model replaced the overlying sediments with high velocity carbonate layers (Figure 3.3c), with velocities ranging between 5000 m/s and 6000 m/s. The top surface of the salt in the PSTM result is now showing the negative reflectivity (Figure 3.3d). The salt

velocity (4600 m/s) is lower than the velocities of shallow uneroded layers (5000 – 5210 m/s). Therefore, as expected, the PSTM result of this model shows a "push-down" of the underlying horizons under the anticline.

A hybrid sedimentary cover with the clastic rocks (2900 - 3500 m/s) overlying carbonates (5400 - 6000 m/s) was used for the third model (Figure 3.3e). The cover sediments, therefore, combine the shallow part of the first model and the deep part of the second model. The contact between the clastic rocks and carbonates shows a positive reflectivity, while the top salt surface shows a negative reflectivity (Figure 3.3f). Similar to the first model, the salt velocity is higher than the velocities of shallow uneroded clastic layers in the synclines. As a result, a "pull-up" can be observed under the thicker salt pillow.

**Effects of salt vs shale core**

Shale can be mobile when overpressured. The mobile shale is characterized by low seismic velocity, low density, and ductile deformation (Wiener et al., 2010). It can form a ductile substrate just like the salt to form the core of detachment folds. However, shale mobility is dependent on overpressuring, compared to the salt, for which mobility is a fundamental material property (Morley and Guerin, 1996). Mobile shale is associated with numerous hydrocarbon-bearing basins, such as the Gulf of Mexico, the Gulf of Guinea, and the Niger Delta (Morley and Guerin, 1996; Wu et al., 2000; Wiener et al., 2010).

In this section, two scenarios are investigated to study the difference between the salt-cored and shale-cored detachment folds. Two velocity models share the same characteristics except for the velocity of the ductile unit, with the hybrid cover having the same velocity model as shown in Figure 3.3e. The first model contains a salt unit with high seismic velocity (4600 m/s) (Figure 3.4a), while the second has a mobile shale unit with

much lower velocity (2800 - 3000 m/s) (Figure 3.4c). Compared to the significant "pull-up" effect under the anticline of the PSTM seismic data of the salt-cored detachment fold (Figure 3.4b), there is a gentle "push-down" in the PSTM seismic data of the shale-cored model (Figure 3.4d), caused by the thick low velocity shale. The mobile shale seismic velocity is slower than the shallow sediments. In addition, there are multiples of the top and bottom surfaces of the shale unit as pointed by the arrows in Figure 3.4d. The waves reflected from these two surfaces bounce an additional time within the high acoustic impedance carbonate units.

Figure 3.8 shows an example of a detachment fold in the deepwater west Niger Delta (Briggs, et al., 2006). The detachment is within an overpressured shale unit. Similar to the PSTM seismic data of the shale-cored detachment fold model (Figure 3.4d), a low relief "push-down" of the detachment and underlying sediments can be observed beneath the thickest part of the mobile shale.

**Case study: Appalachian Plateau fold belt**

The Appalachian Plateau has long been known to contain low relief detachment folds with high wavelength/amplitude ratios (Gwinn, 1964). Recent hydrocarbon exploration and development of Marcellus shale in north Pennsylvania has resulted in the availability of newer and higher quality seismic and well data. This has led to a better understanding of the structural style of the Appalachian Plateau fold belt developed during the late Paleozoic Alleghanian Orogeny (Mount, 2014; Gillespie and Kampferk, 2017).

The Appalachian Plateau fold belt in north Pennsylvania is developed above a detachment in Upper Silurian Salina Group evaporites (Rogers, 1963; Gwinn, 1964; Davis and Engelder, 1985). The structural style is strongly controlled by the thickness of the

evaporites. Where the evaporites are thin, the structural style is characterized by short-wavelength, low-amplitude, symmetric detachment folds, while large amplitude, asymmetric detachment folds dominate the area over thick evaporites (Frey, 1973; Davis and Engelder, 1985; Mount, 2014). The relationship between the structural style and the thickness of the ductile substrate is confirmed by experimental models (Costa and Vendeville, 2002; Li and Mitra, 2017).

Using 2D lines and 3D seismic surveys over north Pennsylvania, Mount (2014) observed velocity "push-downs" beneath areas of thick halite, and concluded that the cause of these "push-downs" is that the seismic velocity of the halite is slower than the adjacent Paleozoic rocks (Figure 3.9). Our models show that salt-cored detachment folds normally would have "pull-ups" under the thick salt unit areas, except if all of the cover sediments are carbonates (Figure 3.3c). To study this unusual case, the Liberty anticline from northern Pennsylvania is selected for seismic modeling (Figure 3.6).

The geometry of the model (Figure 3.6) is simplified from the seismic interpretation by Mount (2014) and the seismic velocity information is approximated from the sonic logs from Occidental Petroleum Corporation Burley No. 1 well in the SW West Virginia (Kulander and Ryder, 2005) and a well in the NE Pennsylvania (Far and Hardage, 2014) (Figure 3.6). Since there is no reliable published sonic log data for the Salina evaporites over the study area, we adopted the typical salt seismic velocity (4600 m/s) based on previous description of the Salina Group being made up of halite and anhydrite (Rogers, 1963; Frey, 1973; Davis and Engelder, 1985; Mount, 2014). The PSTM result of the model (Figure 3.10b) generally reproduces the geometry of the Liberty anticline in the actual

seismic data (Figure 3.11a). However, the expected “push-down” cannot be found in the PSTM result of the model.

Our seismic models suggest that the only two scenarios which result in a seismic “push-down” are very high velocities in the shallow cover sediments, typically found only in carbonates, or core velocities with lower velocities than halite (4600 m/s). For the Liberty anticline, the cover sediments are a hybrid complex of clastic and carbonate sediments. The seismic velocities of shallow clastic sediments are indeed anomalously high (4350 – 4500 m/s) compared to normal shallow clastic units because the Appalachian Plateau has experienced significant uplift following deep burial. However, the shallow uneroded sediments are still lower than the typical halite velocity of 4600 m/s, so that a “push-down” would not be expected in the PSTM model.

Since the “push-downs” are present in the time migrated seismic data shown by Mount (2014), a reasonable hypothesis is that the Salina group here is not pure salt and that the velocity of the ductile unit is much lower than the typical salt velocity.

A second model is built to test this hypothesis (Figure 3.10c) using a seismic velocity of the ductile unit as 4000 m/s. A “push-down” under the thick Salina unit is seen in this case (Figure 3.10d), with the amount of push-down similar to the actual case (Figure 3.11c). The “push-down” is increasing laterally as the Salina unit thickens.

Therefore, the Salina Group in the Appalachian Plateau fold belt may not be made up of pure halite, and the lithology and seismic velocities should be reevaluated. Although, other factors such as salt anisotropy (Jones and Davison, 2014) and salt-induced stress anomalies (Hoetz et al., 2011) could be attributing to the “push-downs”, they are not significant enough to cause the “push-down” independently if the Salina ductile unit is pure

salt. The models suggest that further study of the Salina Group is necessary for correct depth conversion or migration of the seismic data if imaging of the strata below the Salina Group is needed for hydrocarbon exploration and development.

**The effects of geometry related to structural evolution**

Three models in this section represent three stages of the evolution of a detachment fold structure (Figure 3.5). With the growth of the fold, the limb lengthens and steepens, involving hinge migration and limb rotation (Mitra, 2003). As the fold tightens and the anticlinal area increases, the synclinal area decreases. Therefore, in the late stage of the deformation, the units almost return to their regional positions in the synclines (Figure 3.5e). The cover sediments and basal units maintain the constant area when reconstructed for eroded cover sediments. A hybrid model of clastic sediments overlying carbonates is used with the same velocities as in Figure 3.3e. Salt with a constant velocity of 4600m/sec is used for the basal unit.

For the first stage, all the elements of the structure can be imaged well in the PSTM model (Figure 3.5b). The interface between the clastic rocks and the carbonates and the top and bottom surfaces of the salt are strong reflectors due to the large contrast of acoustic impedance.

As the structure evolves into a disharmonic detachment fold, segments of the two limbs of the anticline are not well imaged with PSTM because of their steeper dips (Figure 3.5d). Some traces of the top carbonate horizon can still be observed for the two limbs. There is also a noticeable decrease in the quality of the image under the salt because of the larger thickness of the salt coring the anticline.

With further evolution to a lift-off structure (Figure 3.5e), the anticline limbs are very steep to vertical or overturned. In the PSTM data (Figure 3.5f), only the crest of the structure is imaged with two wide no-data zones representing the limbs. The imaging of the structure under the salt anticline is poor, and both the top and base of the salt are difficult to trace. The "pull-up" under the anticline is progressively more pronounced with increasing structural relief (Figure 3.5d, f) because of the increase in the thickness of the salt in the anticlinal core relative to the more uniform thickness of the low-velocity clastic sediments in the synclines.

**Asymmetric and faulted detachment folds**

The above models address the seismic expression of symmetric detachment folds as they progress from low amplitude folds to disharmonic detachment folds to lift off folds with a progressive increase in shortening. Variations in geometry from the above models include asymmetric fold geometries, faulted detachment folds with both asymmetric and symmetric geometries. The seismic expressions of these types of structures are addressed in this section.

A series of models are developed to study some representative types of asymmetric and faulted detachment folds (Figure 3.7a, c, e). In these models, the pre-growth strata are preserved, so that there is no erosion of the competent layers above the ductile substrate. The pre-growth strata are overlain by growth strata with gradual increasing seismic velocity along with the depth. The lithology of the ductile substrate used in these models is pure salt with the P-wave velocity of 4600 m/s.

Faulted detachment folds form by a transition in deformation behavior from detachment folding to progressive fault propagation with increasing shortening (Mitra, 2002). The

structure starts with symmetric or asymmetric detachment folding. The first model shows an asymmetric detachment fold example at this stage (Figure 3.7a). The fold progressively tightens with limb rotation and internal shear confined to limb segments with the most rotation. The thrust faults propagate through the competent layers and into the upper incompetent units and downward within the ductile unit. Finally, the fault connects with the basal detachment and breaks through the deformation zone in the upper unit. This stage is illustrated by the second model (Figure 3.7c). The third model shows a faulted symmetric detachment fold with opposite dipping faults curring through both limbs (Figure 3.7e).

The first model shows an asymmetric detachment fold without any fault breakthrough (Figure 3.7a). The PSTM model (Figure 3.7b) exhibits good imaging of the low-dipping back limb and the undeformed section above the ductile layer. However, there is a band of the low-reflectivity on the front limb where the dips are high in the model. The gap between the upper front limb and the lower front limb is clear. In a natural case, this band of the low-reflectivity could be misinterpreted as a thrust fault especially with the appearance of reverse-fault-like dislocation. The area under the fault also shows poor imaging, due to both steep dips and a "fault-shadow" effect. The "pull-up" under the salt is asymmetric and also marked by poor migration as indicated by the crossing of reflectors.

A thrust fault finally develops in the highly strained segment on the front limb within the cover units. In the final stage of the evolution, the thrust fault propagates through the front limb and connects with the basal detachment, and a kink band developed on the back limb to accommodate the backward shear (Figure 3.7c).

For the front limb, the fault plane is well imaged, with a negative reflection amplitude because it juxtaposes high velocity units above against low velocity units across the fault

(Figure 3.7d). In natural examples, with less signal to noise ratio and more diffraction associated with the fault zone, the imaging of the fault plane may not be as clear. A wide zone both above and below the fault is not imaged because of the steep dip. This zone closely resembles that seen in Figure 3.7b, except that the displacement between the hanging wall and footwall is much more prominent. A comparison of Figure 3.7b and Figure 3.7d shows the problem of determining whether the front limb is faulted or not, and the exact location of upward termination of the fault, in the absence of a good fault plane reflector. Kostenko et al (2008) document a natural example of a structure from the deepwater Niger Delta fold belt, in which the location of fault termination, while critical in estimating hydrocarbon reserves, is difficult to determine from the seismic data.

The footwall syncline cannot be recognized in the PSTM model, because the syncline through is pulled up under the "shadow" of the high velocity anticline.

The kink band on the back limb is imaged as a low-reflectivity zone which is showing a dislocation and could be misinterpreted as a back thrust. Figure 3.12 shows a seismic section across the Perdido fold belt in the NW deep-water Gulf of Mexico (Camerlo and Benson, 2006). The section is composed of seven detachment folds. One of the obvious observations is that every anticline is associated with two low-reflectivity bands. Previously, the folds were interpreted as reverse-faulted, salt-cored detachment folds (Peel et al., 1995; Trudgill et al., 1999). Later Camerlo and Benson (2006) interpreted those low-reflectivity bands as kink bands, rather than associated with large scale faulting. The key difference would be whether individual reflections can be connected through the kink bands as suggested by Camerlo and Benson (2006).

The bands are more prominent for an angular fold (Figure 3.13a) modeled with PSTM in Figure 3.13b. this fold is an angular version of the asymmetric faulted detachment fold modeled in Figure 3.7c. The resolution of whether these bands or no data zone represent faults or kink bands is dependent on correctly estimated stacking velocities.

Since the signal-to-noise ratio of the input data is not as good as the models, the stacked amplitude in the velocity spectrum may not be as clear as what we have for the models. Therefore, higher or lower stacking velocity might be picked for an event. The task of picking a correct velocity for a fold hinge may be especially challenging. We select a portion of the hinge between the front limb and the crest top as shown by the box in Figure 3.13a. Within this box portion, the stacking velocity varies for three different scenarios. The velocity spectrum panel (Figure 3.13c) shows an example of correct, higher, and lower velocity picking.

The PSTM results are presented in Figure 3.13b. With higher stacking velocity (Figure 3.13d), the front limbs are migrated to a lower position than the correctly migrated result (Figure 3.13e), therefore the crest reflectors and front limb reflectors cross each other. In contrast, with lower stacking velocity (Figure 3.13f), the front limb reflectors are pulled away from the crestal reflectors showing curved edges for the hinge. The gaps or overlaps between the crest and the front limb could result in apparent zones of shear or no data zones.

The third model in Figure 3.7 shows a symmetric faulted detachment fold which has two thrust faults propagating through the competent layers above the salt (Figure 3.7e). Compared to the shallow synclines in the previous two models, two synclines in this model are deeper with steeper limbs. That results in poorer images of the synclines and dimmer reflections from the layers below them (Figure 3.7f). Two fault planes are well imaged but

show lower dips, particularly towards the core of the anticline, due to higher velocities in this area.

**Conclusions**

Detachment and faulted detachment folds make up a common structural style in fold and thrust belts. The seismic interpretation of PSTM data of detachment folds is challenging due to the complexities like significant lateral velocity variations caused by salt or shale units in the core and overburden strata, steep dips, and complex fold-fault relationships. We conduct 2D seismic modeling to identify and resolve common artifacts and pitfalls associated with the interpretation of PSTM data through detachment folds.

The seismic velocities of the cover and core sediments control the seismic appearance of the structure. For salt-cored detachment folds, strata below the salt are pulled up, provided the velocity of the salt is higher than that in the shallow shallow strata filling the synclines. For shale-cored detachment folds, since the velocity of the overpressured shale is much lower than the covering sediments, there will be “push-downs” under the shale strata.

Modeling of a natural structure from the Appalachian Plateau fold belt was used to resolve the cause of an observed “push-down” under the Salina Group. The results suggest that the “push-down” effect might be a result of both high velocities of the cover sediments and the possibility that the Salina Group is not made up of pure salt, and therefore has lower average velocities.

With progressive evolution of a salt-cored detachment fold into a disharmonic detachment fold and a lift-off fold, the fold wavelength decreases, while the amplitude increases. As the limbs of the fold steepen, the steep limbs are not well imaged. The “pull-

up" effect is more pronounced with increasing amplitude of the top of the salt. The overall imaging quality of the structures below the anticline is poor for the later stage of the evolution.

For asymmetric and faulted detachment folds, the front limbs, especially the portions close to the thrust fault, are poorly imaged showing a wide low-reflectivity band. These bands can be alternatively interpreted as fault zones or kink bands with high dips. The "pull-ups" under the front limbs are segmented, while the ones under the back limbs are more gradual. Additional distortion can be observed for the frontal part of the syncline under the "shadow" of the high velocity anticline.

Picking the correct stacking velocity for an angular fold hinge can influence the final image. A higher stacking velocity would cause a "crossing" artifact, while a lower stacking velocity would round the angular edges or result in gaps of no data zones.

**Acknowledgments**

All synthetic models were constructed and imaged using Tesseral Pro. We thank Tesseral Technologies for providing the academic license of Tesseral Pro. The synthetic seismic data is processed in VISTA. Schlumberger is thanked for providing the academic license of VISTA.

## CHAPTER 3 FIGURES

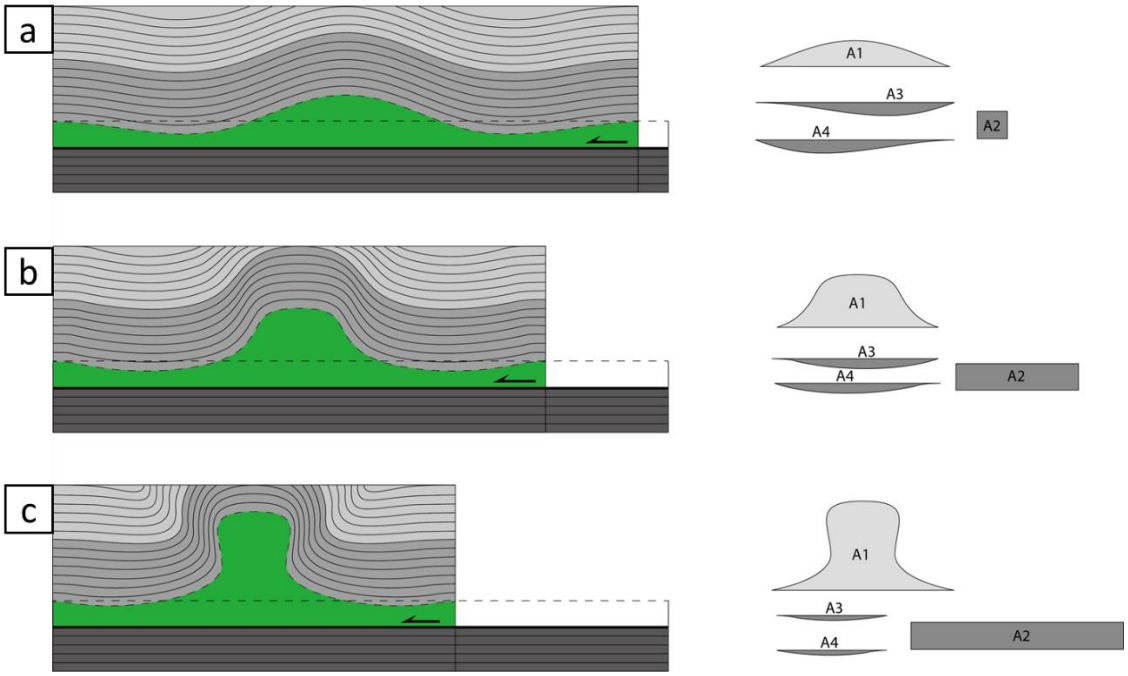


Figure 3.1. Model for the evolution of a symmetric detachment fold (modified from Mitra, 2003). (a) Low amplitude fold. (b) Disharmonic detachment fold. (c) Lift-off fold. Area balancing requires that the anticlinal area above the regional position of the core unit (A1) equal to the sum of the shortening area (A2) and the synclinal areas (A3, A4).

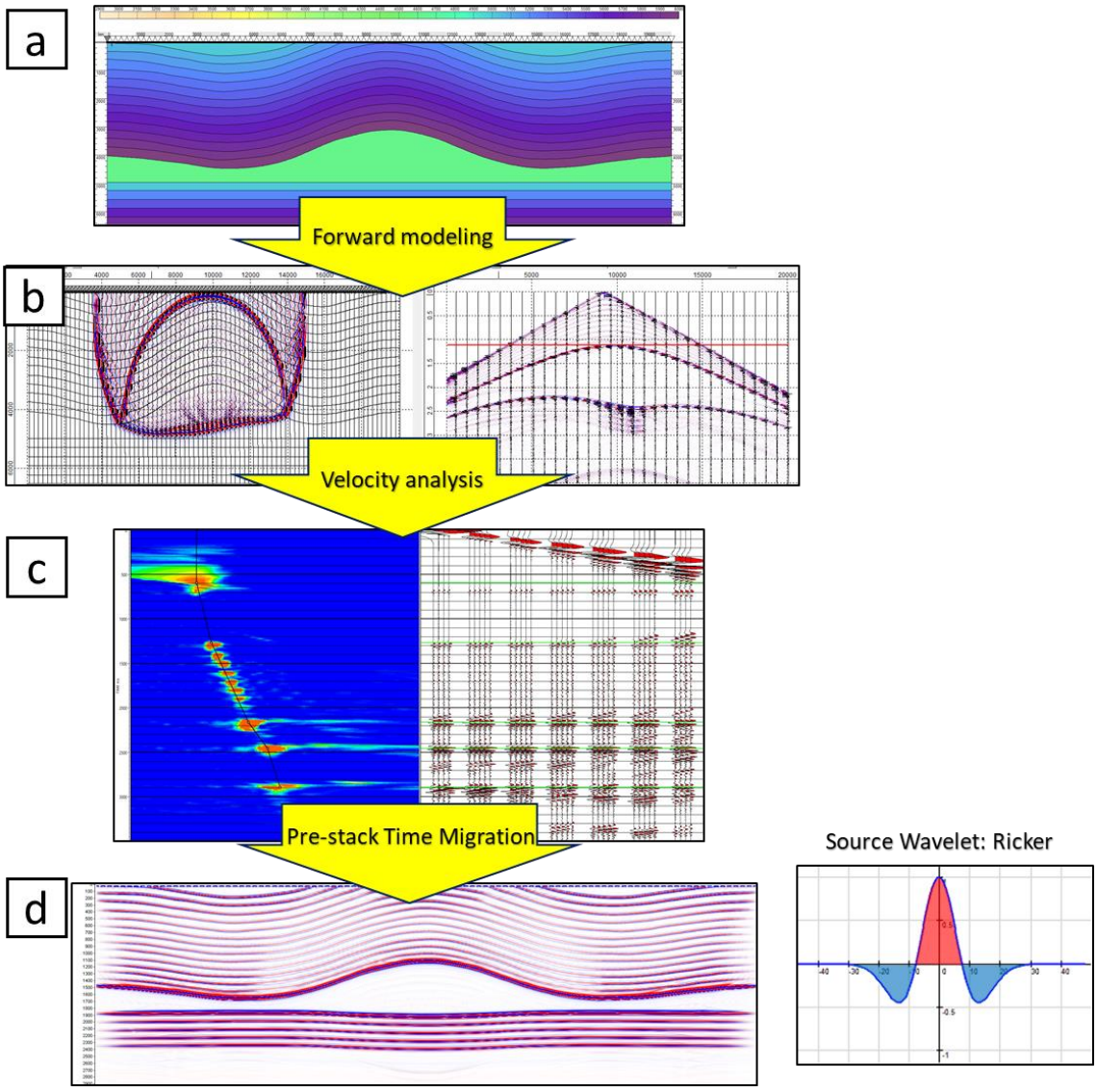


Figure 3.2. A workflow showing the key steps in the seismic forward modeling method used in the study: forward modeling, velocity analysis, and PSTM. (a) Velocity model in depth. (b) Snapshot of the wave propagation and the shot gather from the same source. (c) Velocity analysis panel. (d) PSTM result. The source wavelet is Ricker wave with a frequency of 30 Hz.

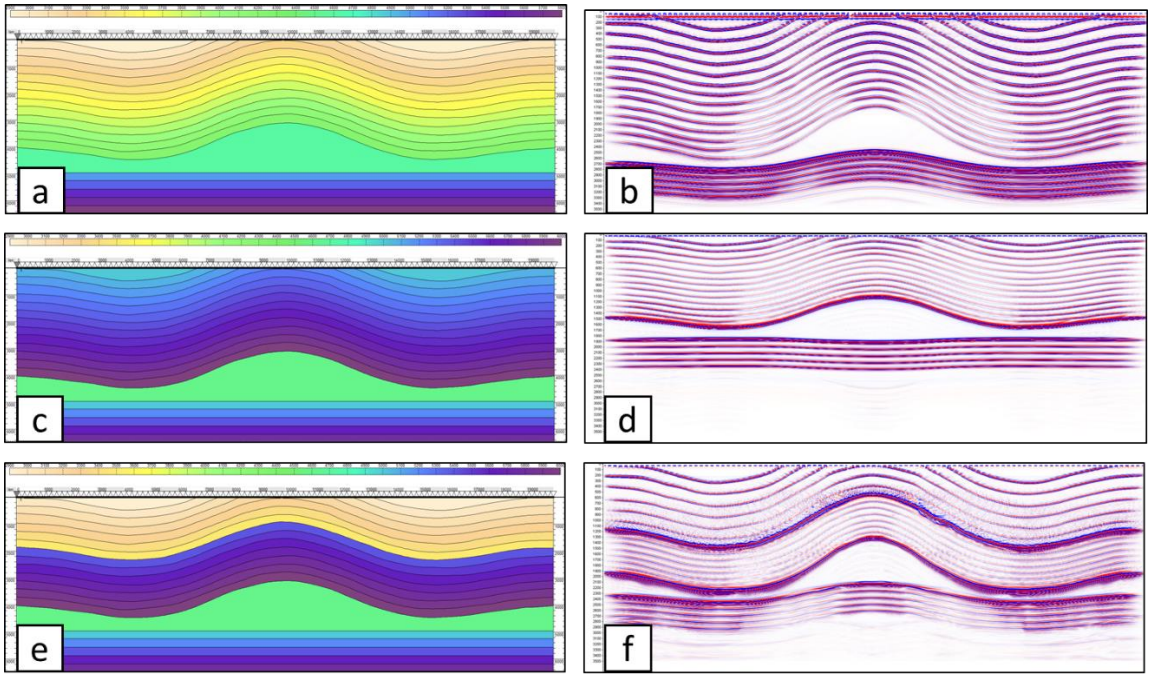


Figure 3.3. Three velocity models showing the effects of the seismic velocities of the cover sediments (a), (c), (e) and resulting PSTM models (b), (d), (f). (a) Clastic cover. (c) Carbonate cover. (e) Hybrid cover with clastic rocks overlying carbonates.

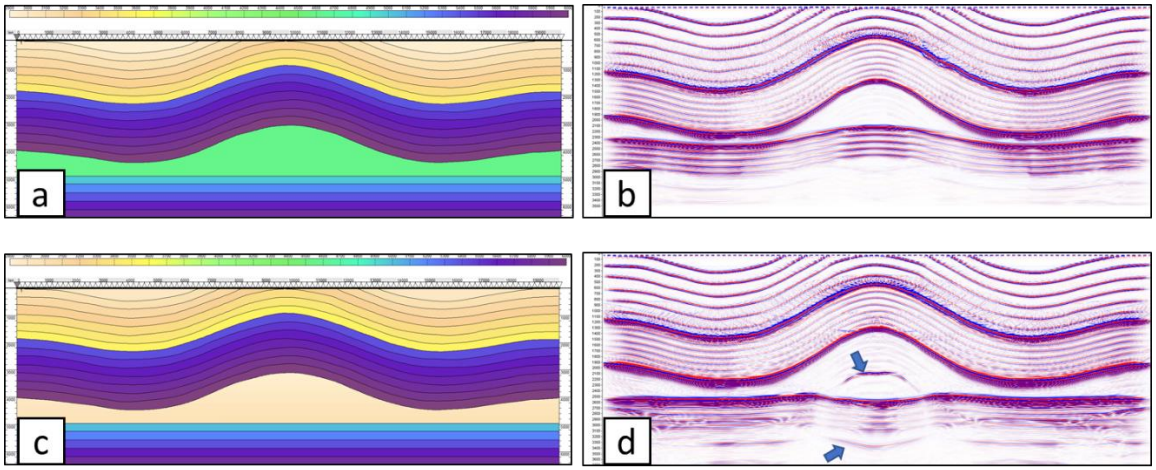


Figure 3.4. (a) Salt cored detachment fold model. (b) PSTM result of the salt cored detachment fold model. (c) Shale cored detachment fold model. (d) PSTM result of the shale cored detachment fold model. Multiples are pointed by the arrows.

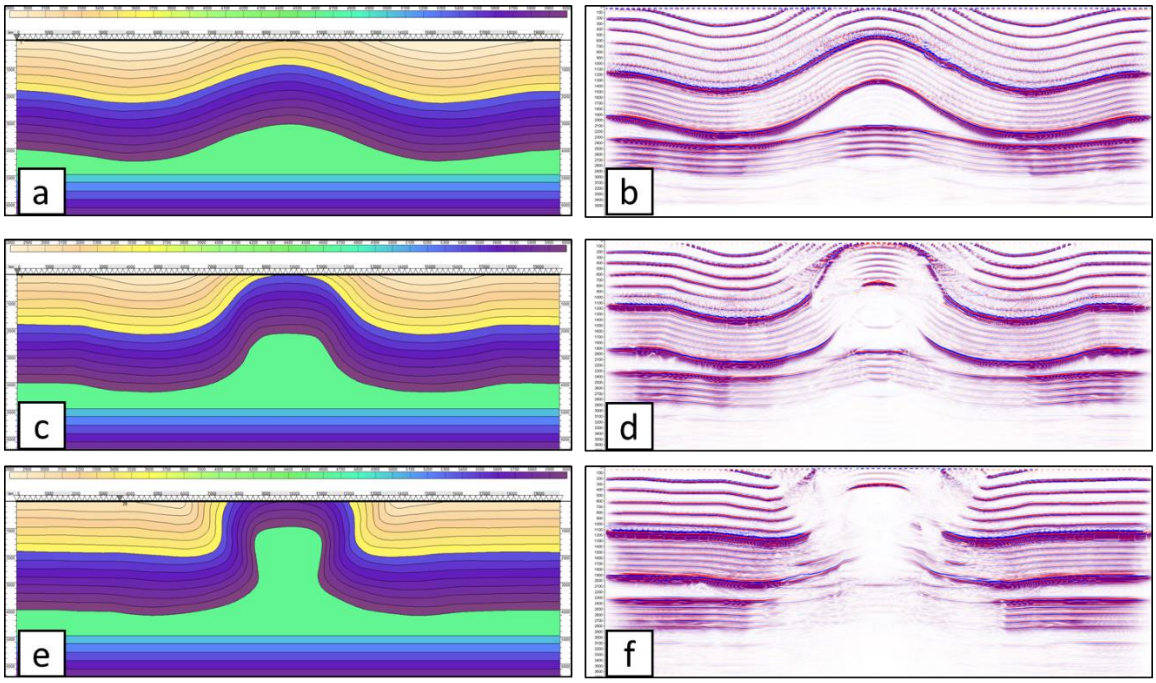


Figure 3.5. Three velocity models to study the effects of the evolution of the structure (a), (c), (e) and correlating PSTM results (b), (d), (f). (a) Low amplitude fold. (c) Disharmonic detachment fold. (e) Lift-off fold.

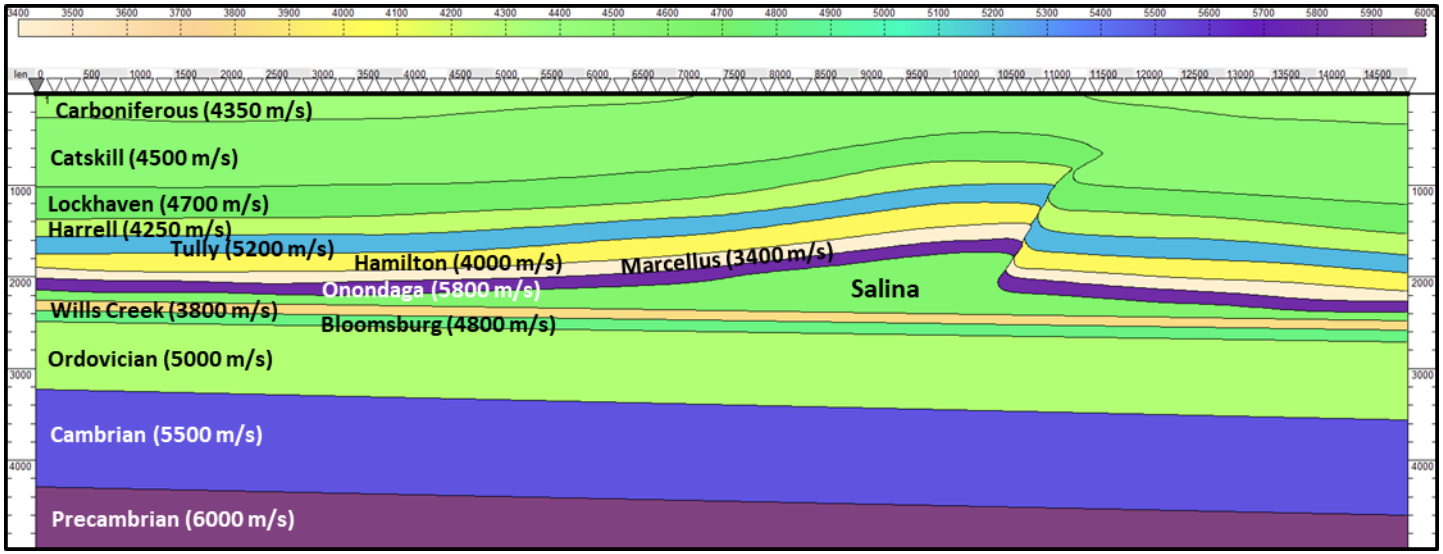


Figure 3.6. The Liberty anticline velocity model in depth with no vertical exaggeration (modified from Mount, 2014). The seismic velocity of each layer is estimated from the sonic logs from Occidental Petroleum Corporation Burley No. 1 well in the SW West Virginia (Kulander and Ryder, 2005) and a well in the NE Pennsylvania (Far and Hardage, 2014).

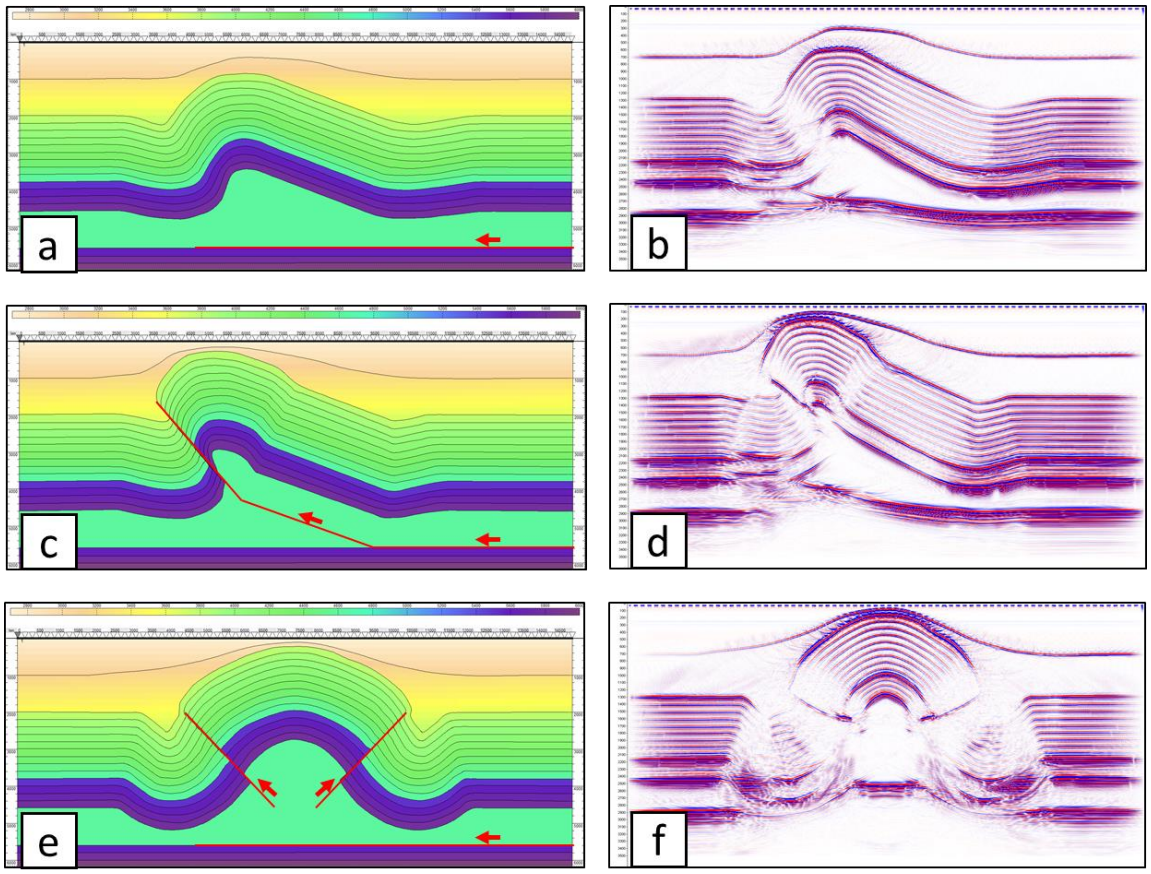


Figure 3.7. (a) and (b) Asymmetric detachment fold model and the PSTM result. (c) and (d) Asymmetric faulted detachment fold model and the PSTM result. (e) and (f) Symmetric faulted detachment fold model and the PSTM result.

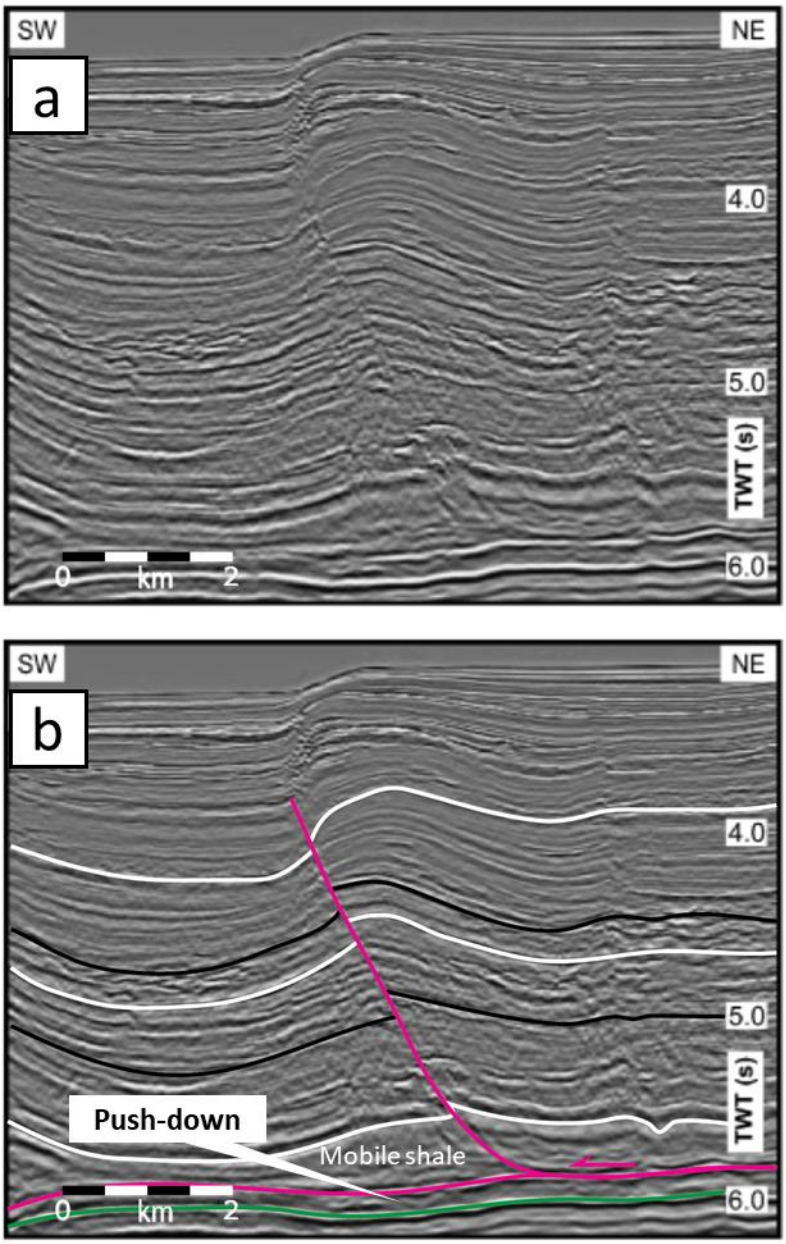


Figure 3.8. Uninterpreted (a) and interpreted (b) seismic section from the deepwater west Niger Delta fold belt showing a faulted detachment fold above a mobile shale unit (modified from Briggs et al., 2006). Note the push down under the thickened shale.

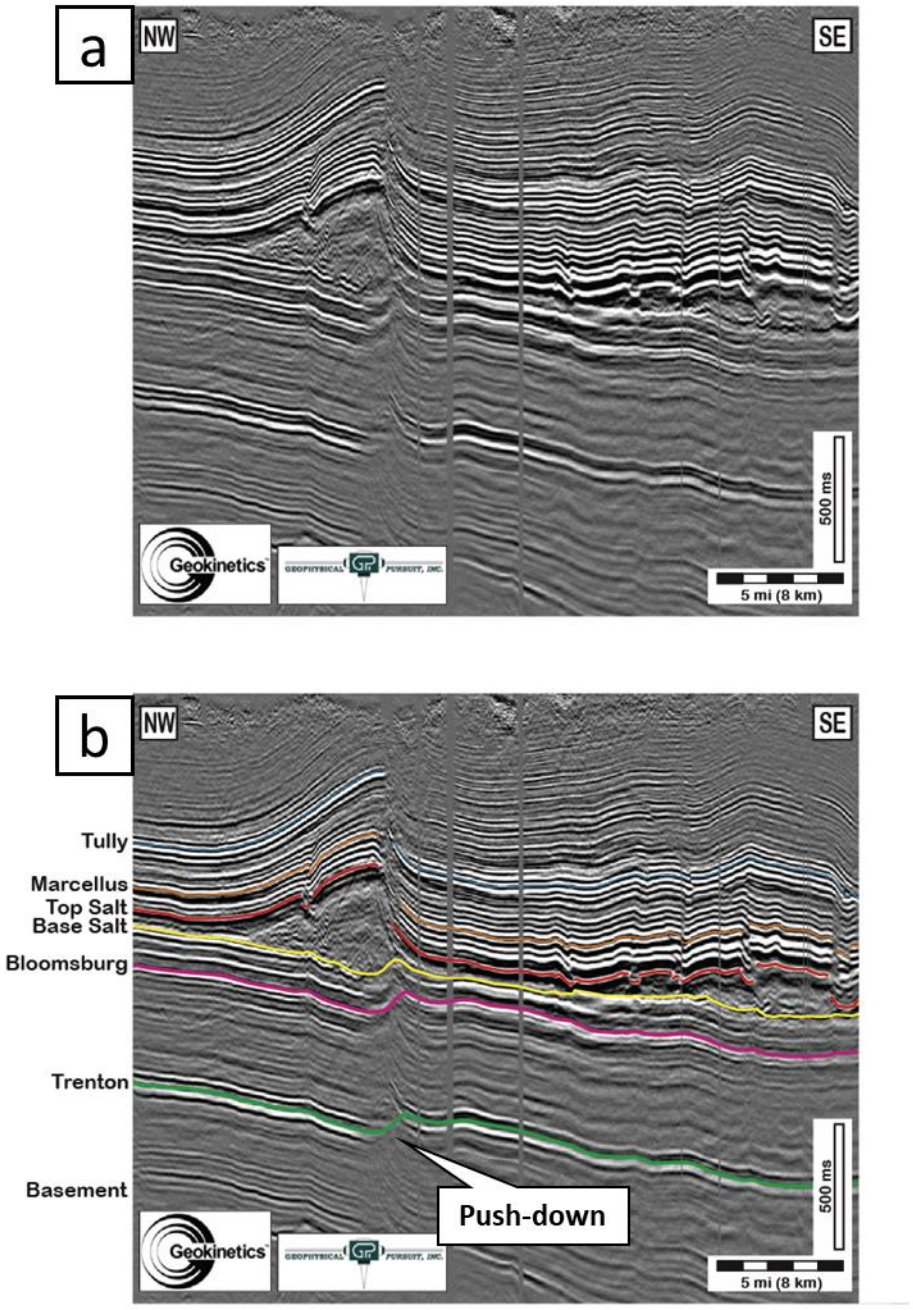


Figure 3.9. Uninterpreted (a) and interpreted (b) seismic sections across the Liberty anticline (after Mount, 2014).

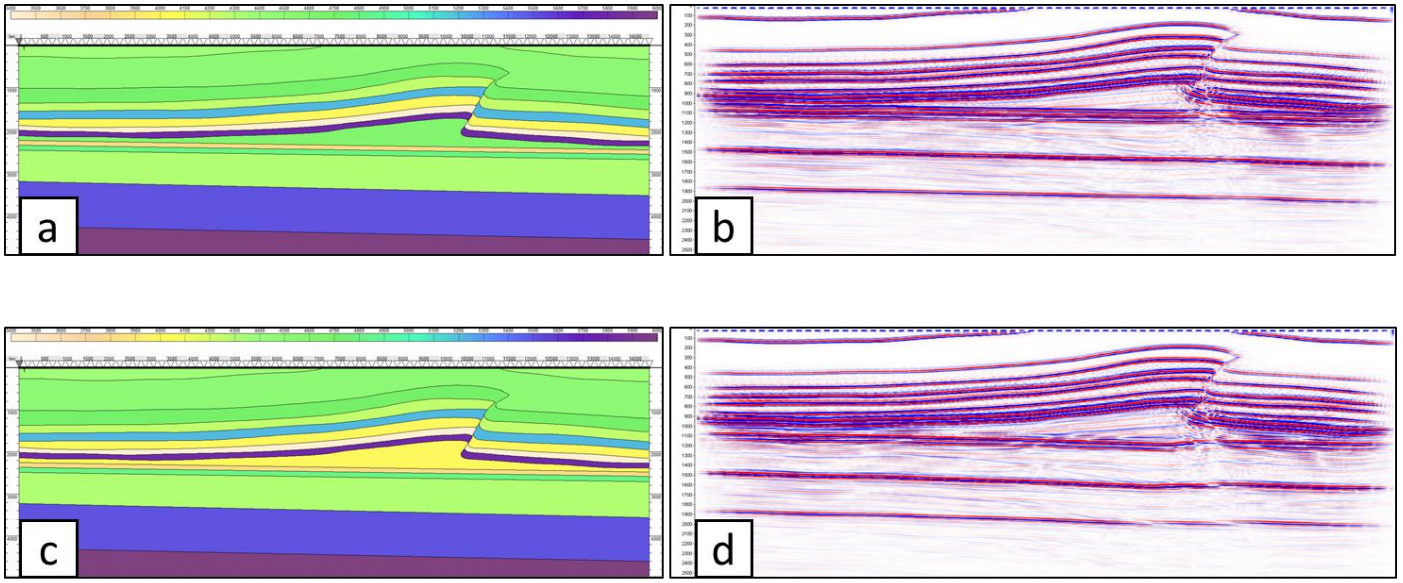


Figure 3.10. Two Liberty anticline models with different seismic velocities for the ductile units. (a) and (b) The model with the ductile unit of 4600 m/s and correlating PSTM result. (c) and (d) The model with the ductile unit of 4000 m/s and correlating PSTM result.

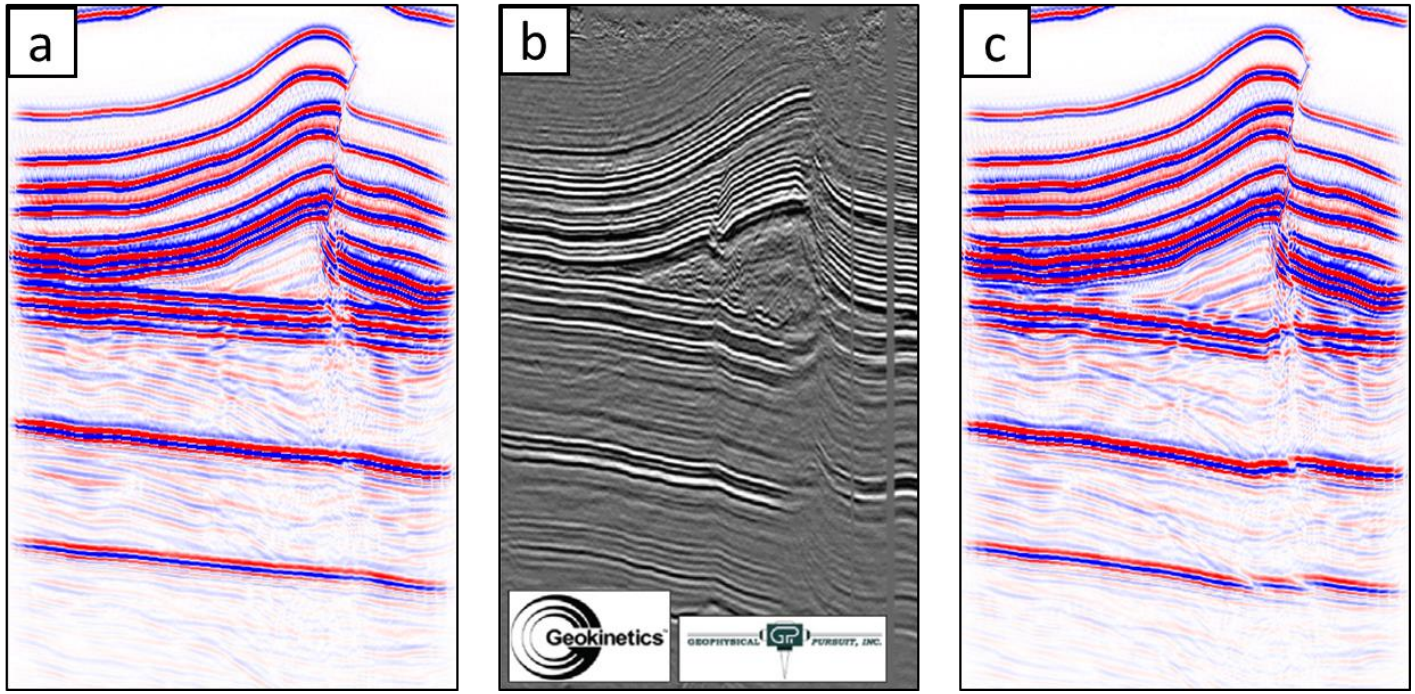


Figure 3.11. Comparison of the synthetic seismic data (a), (c) and the actual seismic data (b) (after Mount, 2014) from the Liberty anticline in the Appalachian Plateau fold belt. (a) The PSTM result of the model with a salt substrate (4600 m/s). (c) The PSTM result of the model with a lower velocity ductile substrate (4000 m/s). Note that (c) resembles (b) better with “push-downs” below the ductile unit.

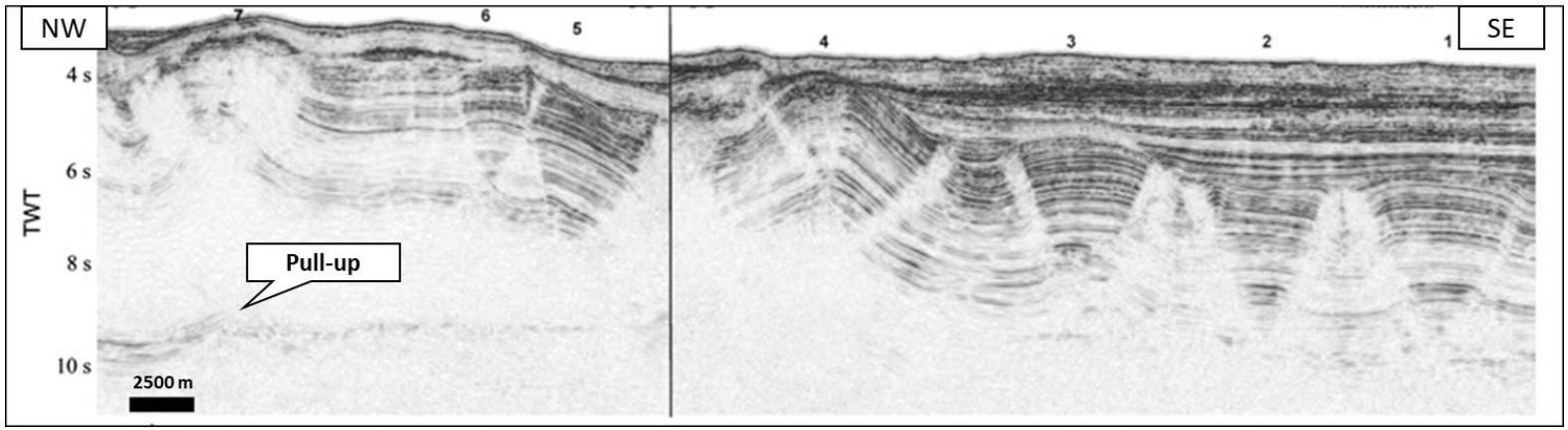




Figure 3.12. Seismic section across the Perdido fold belt (after Camerlo and Benson, 2006). Note the low-reflectivity bands that have alternatively been interpreted as faults and kink bands. (AAPG ©[2006], reprinted by permission of the AAPG whose permission is required for further use).

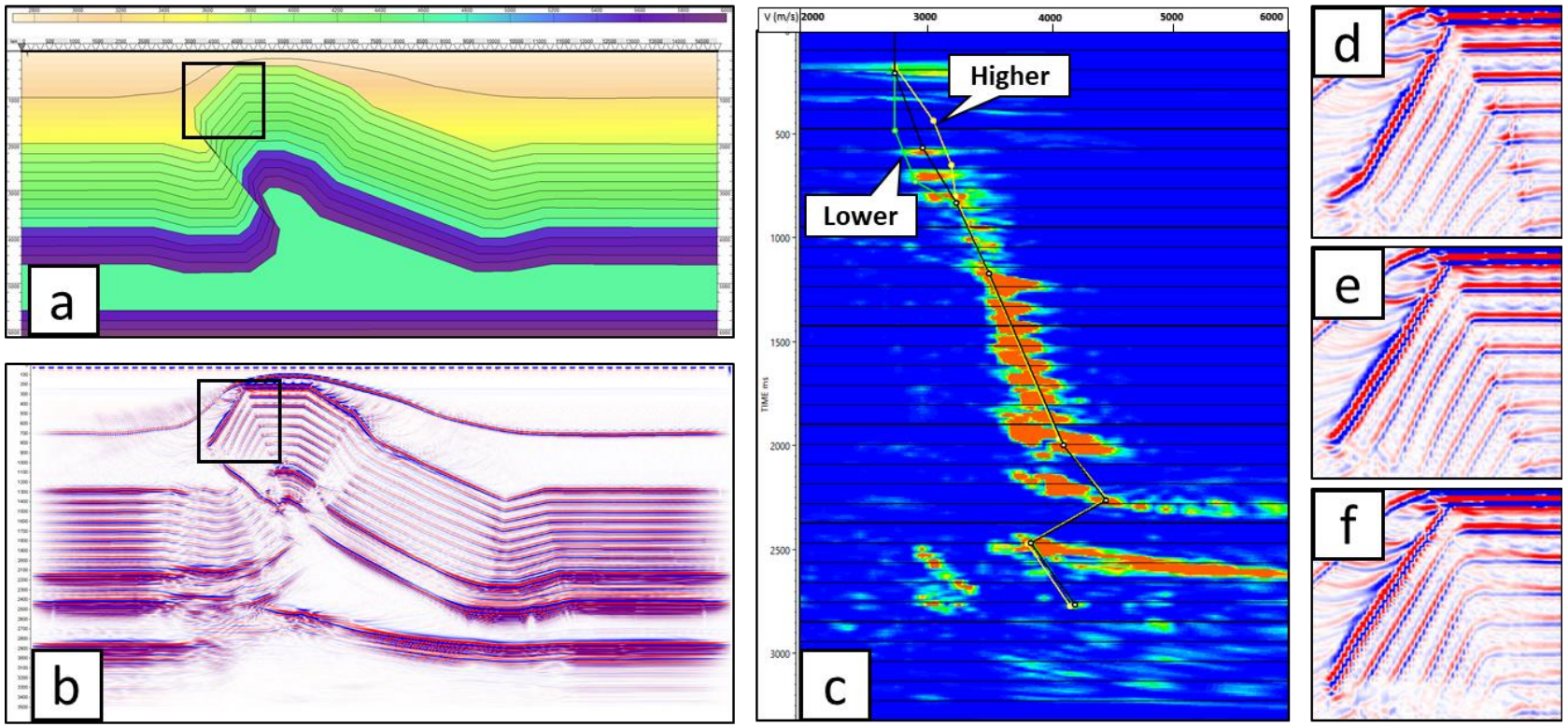


Figure 3.13. (a) and (b) Angular asymmetric faulted detachment fold model and the PSTM result. (c) Velocity spectrum panel illustrating an example of higher (yellow), correct (black) and lower (green) velocity picks. (d), (e) and (f) The PSTM of the box portion in (b) correlating to higher, correct, and lower velocity picks, respectively.

## REFERENCES


Alaei, B., & Petersen, S. A. (2007). Geological modelling and finite difference forward realization of a regional section from the Zagros fold-and-thrust belt. Petroleum Geoscience, 13(3), 241-251.

Briggs, S. E., Davies, R. J., Cartwright, J. A., & Morgan, R. (2006). Multiple detachment levels and their control on fold styles in the compressional domain of the deepwater west Niger Delta. Basin Research, 18(4), 435-450.

Buxtorf, A. (1916). Prognosen und Befunde beim Hauensteinbasis-und Grenchenbergtunnel und die Bedeutung der letztern für die Geologie des Juragebirges. E. Birkhäuser.

Camerlo, R. H., & Benson, E. F. (2006). Geometric and seismic interpretation of the Perdido fold belt: Northwestern deep-water Gulf of Mexico. AAPG bulletin, 90(3), 363-386.

Costa, E., & Vendeville, B. C. (2002). Experimental insights on the geometry and kinematics of fold-and-thrust belts above weak, viscous evaporitic décollement. Journal of Structural Geology, 24(11), 1729-1739.

Cotton, J. T., & Koyi, H. A. (2000). Modeling of thrust fronts above ductile and frictional detachments: Application to structures in the Salt Range and Potwar Plateau, Pakistan. Geological Society of America Bulletin, 112(3), 351-363.

Dahlstrom, C. D. (1990). Geometric Constraints Derived from the Law of Conservation of Volume and Applied to Evolutionary Models for Detachment Folding: Geologic Note:(1). AAPG Bulletin, 74(3), 336-344.

Davis, D. M., & Engelder, T. (1985). The role of salt in fold-and-thrust belts. Tectonophysics, 119(1-4), 67-88.

De Sitter, L. U. (1964). Structural Geology, Int. Ser. Earth Sciences (McGraw-Hill, New York, 1964), 551.

Fagin, S. (1996). The fault shadow problem: Its nature and elimination. The Leading Edge, 15(9), 1005-1013.

Fagin, S. W. (1991). Seismic modeling of geologic structures: Applications to exploration problems. Society of Exploration Geophysicists.

Far, M. E., & Hardage, B. (2014). Interpretation of fractures and stress anisotropy in Marcellus Shale using multicomponent seismic data. Interpretation, 2(2), SE105-SE115.

Frey, M. G. (1973). Influence of Salina salt on structure in New York-Pennsylvania part of Appalachian Plateau. AAPG Bulletin, 57(6), 1027-1037.

Gillespie, P., & Kampfer, G. (2017). Mechanical constraints on kink band and thrust development in the Appalachian Plateau, USA. Geological Society, London, Special Publications, 458(1), 245-256.

Gwinn, V. E. (1964). Thin-skinned tectonics in the Plateau and northwestern Valley and Ridge provinces of the central Appalachians. Geological Society of America Bulletin, 75(9), 863-900.

Hatchell, P. J. (2000). Fault whispers: Transmission distortions on prestack seismic reflection data. Geophysics, 65(2), 377-389.

Hoetz, G., Steenbrink, J., Bekkers, N., Vogelaar, A., & Luthi, S. (2011). Salt-induced stress anomalies: an explanation for variations in seismic velocity and reservoir quality. Petroleum Geoscience, 17(4), 385-396.

Jamison, W. R., 1987, Geometric analysis of fold development in overthrust terranes: Journal of Structural Geology, 9(2), 207-219.

Jones, I. F., & Davison, I. (2014). Seismic imaging in and around salt bodies. Interpretation, 2(4), SL1-SL20.

Kostenko, O. V., Naruk, S. J., Hack, W., Poupon, M., Meyer, H. J., Mora-Glukstad, M., ... & Mordi, M. (2008). Structural evaluation of column-height controls at a toe-thrust discovery, deep-water Niger Delta. AAPG Bulletin, 92(12), 1615-1638.

Kulander, C. S., & Ryder, R. T. (2005). Regional seismic lines across the Rome Trough and Allegheny Plateau of northern West Virginia, western Maryland, and southwestern Pennsylvania (p. 9). US Geological Survey.

Laubscher, H. P. (1962). Die Zweiphasenhypothese der Jurafaltung. Eclogae Geologicae Helvetiae, 55, 1-22.

Letouzey, J. L. B. C. J., Colletta, B., Vially, R. A., & Chermette, J. C. (1995). Evolution of salt-related structures in compressional settings.

Li, J., & Mitra, S. (2017). Geometry and evolution of fold-thrust structures at the boundaries between frictional and ductile detachments. Marine and Petroleum Geology, 85, 16-34.

Li, J., & Mitra, S. (2019). Seismic Modeling and Expression of Common Fold-Thrust Structures. Interpretation, 8(1), 1-39.

McQuarrie, N. (2004). Crustal scale geometry of the Zagros fold–thrust belt, Iran. Journal of Structural Geology, 26(3), 519-535.

Mitra, S. (2002). Structural models of faulted detachment folds. AAPG bulletin, 86(9), 1673-1694.

Mitra, S. (2003). A unified kinematic model for the evolution of detachment folds. Journal of Structural Geology, 25(10), 1659-1673.

Mitra, S., & Namson, J. S. (1989). Equal-area balancing. American Journal of Science, 289(5), 563-599.

Morley, C. K., & Guerin, G. (1996). Comparison of gravity-driven deformation styles and behavior associated with mobile shales and salt. Tectonics, 15(6), 1154-1170.

Morse, P. F., Purnell, G. W., & Medwedeff, D. A. (1991). Case History 4 Seismic Modeling of Fault-Related Folds. In Seismic Modeling of Geologic Structures: Applications to Exploration Problems (pp. 127-152). Society of Exploration Geophysicists.

Mount, V. S. (2014). Structural style of the Appalachian Plateau fold belt, north-central Pennsylvania. Journal of Structural Geology, 69, 284-303.

Namson, J. S. (1981). Detailed structural analysis of the western foothills belt in the Miaoli-Hsinchu area, Taiwan. Petroleum Geology Taiwan, 1, 31-51.

Peel, F. J., Travis, C. J., & Hossack, J. R. (1995). Genetic structural provinces and salt tectonics of the Cenozoic offshore US Gulf of Mexico: A preliminary analysis.

Rodgers, J. (1963). Mechanics of Appalachian foreland folding in Pennsylvania and West Virginia. AAPG Bulletin, 47(8), 1527-1536.

Rowan, M. G. (1997). Three-dimensional geometry and evolution of a segmented detachment fold, Mississippi Fan foldbelt, Gulf of Mexico. Journal of Structural Geology, 19(3-4), 463-480.

Stocklin, J. (1968). Structural history and tectonics of Iran: a review. AAPG bulletin, 52(7), 1229-1258.

Suppe, J. (1985). Principles of structural geology. Prentice Hall.

Trudgill, B. D., Rowan, M. G., Fiduk, J. C., Weimer, P., Gale, P. E., Korn, B. E., ... & Dobbs, S. W. (1999). The perdido fold belt, northwestern deep gulf of mexico, part 1: Structural geometry, evolution and regional implications1. AAPG bulletin, 83(1), 88-113.

Vidal-Royo, O., Koyi, H. A., & Muñoz, J. A. (2009). Formation of orogen-perpendicular thrusts due to mechanical contrasts in the basal décollement in the Central External Sierras (Southern Pyrenees, Spain). Journal of Structural Geology, 31(5), 523-539.

Wiener, R. W., Mann, M. G., Angelich, M. T., & Molyneux, J. B. (2010). Mobile shale in the Niger Delta: Characteristics, structure, and evolution.

Withjack, M. O., & Pollock, D. D. (1984). Synthetic seismic-reflection profiles of rift-related structures. AAPG Bulletin, 68(9), 1160-1178.

Wu, S., Bally, A. W., Mohriak, W., & Talwani, M. (2000). Slope tectonics-comparisons and contrasts of structural styles of salt and shale tectonics of the northern Gulf of Mexico with shale tectonics of offshore Nigeria in Gulf of Guinea. GEOPHYSICAL MONOGRAPH-AMERICAN GEOPHYSICAL UNION, 115, 151-172.

# CHAPTER 4: SEISMIC ANALYSIS OF POLYGONAL FAULT SYSTEMS IN THE GREAT SOUTH BASIN, NEW ZEALAND


## ABSTRACT

Polygonal fault systems (PFS) consisting of networks of layer-bound normal faults are analyzed for Eocene strata in the Great South Basin, New Zealand. An advanced fault enhancement and skeletonization method is applied to delineate faults using 3D seismic data from the Great South Basin. The process sharpens structural and stratigraphic discontinuities and smears the incoherent noise on coherence to obtain a skeletonized fault probability volume which can be directly used to extract and map fault geometries. The characteristics of the polygonal faults in cross-section, planiform, and 3D space were studied. The faults dip approximately 50°, with displacements on a single fault ranging from tens of meters to a hundred meters. The fault planiform patterns are polygonal but also related to the regional horizontal stress anisotropy caused by slope changes of the basal unit. The patterns vary from linear for high slopes, rectangular for moderate slopes and polygonal for low slopes. Two preferred orientations may reflect the superposition of deep Cretaceous trends on the polygonal system in the Eocene strata. A local concentric pattern with outward dipping normal faults is related to passive or active draping above a circular plutonic-volcanic structure. The genetic mechanism of the polygonal fault systems is interpreted to be related to volume loss and shear failure related to opal-A to opal-CT transition within the sediments.

## Introduction

Polygonal fault systems are defined by a network of layer-bound, mesoscale (throws from 10 to 100 m) normal faults arranged in a polygonal structure (Cartwright and Dewhurst, 1998). They are widely developed along many continental margin basins and some intracratonic and foreland basins (Cartwright, 2011), for example, the Central North Sea (Lonergan & Cartwright, 1999), the Lake Hope region, South Australia (Watterson et al., 2000), the Lower Congo Basin (Gay et al., 2004), the Sable Sub-basin, the Canadian Atlantic margin (Hansen et al., 2004), and the South China Sea (Chen et al., 2011). Unlike tectonically induced fault systems, which are dependent on the orientations and magnitudes of the principal tectonic stresses, polygonal fault systems are layer bounded and generally interpreted to have formed in response to differential compaction or diagenesis in the sedimentary sequence.

In this study, an advanced fault enhancement and skeletonization operation was applied to 3D seismic data of the Great South Basin (GSB), New Zealand, to study polygonal fault networks within the basin. Extraction of 3D fault data was used to produce a fault probability volume. Based on the original amplitude data and the fault probability data, the characteristics of different fault systems in cross-section, maps, and 3D space were studied. In addition, the genetic mechanisms of formation of the polygonal fault systems (PFS) were investigated.

The Great South Basin (GSB) is located to the southeast of the coastline of the South Island, New Zealand (Figure 4.1). The GSB formed as a result of Late Cretaceous rifting during the breakup of part of Gondwanaland into Australia, Antarctica and New Zealand (Hayes and Ringis, 1973; Molnar et al., 1975; Carter, 1988). This resulted in a NE-SW

trending normal fault system forming horst, graben, and half graben structures. The fault systems discussed in this study are located within the post-rift Rakiura Group within the Pakaha graben, and postdate the tectonic fault systems in the GSB.

**Geological framework**

The Great South Basin originated during the late Cretaceous (Cenomanian/Turonian) rifting with separation of the Australia, Antarctica and New Zealand plates along a complex system of ridges (Carter, 1988; Ghisetti, 2010). The syn-rift section is dominated by remnant half grabens, horsts, and grabens formed during the rifting event. During the Santonian, the basin experienced flooding and drowning which was responsible for the deposition of organic-rich shales. (ExxonMobil Exploration Company, 2010; Morley et al., 2017).

During late Cretaceous to top Eocene, the post-rift sag phase was dominated by the subsidence in the central part of the basin. The post-rift section in the GSB can be divided into two groups: Pakaha and Rakiura (Figure 4.2). In the study area, the Pakaha Group exhibits a transition from the widespread deposition of organic-rich shales during the Paleocene-Eocene to early Eocene deltaic progradation (Killops et al., 2000; Morley et al., 2017). The Rakiura Group (Eocene) contains siltstones, shales and marls.

The Marshall Paraconformity separates the Eocene and Oligocene units and defines the upper limit of the fault systems in the study area. Above the Marshall Paraconformity, the Oligocene is dominated by cherty limestones (Morley et al., 2017). Post-Oligocene tectonics is characterized by an orogenic phase which is dominated by horizontal shortening and vertical uplift along the Alpine plate boundary (Molnar et al., 1975; Ghisetti,

2010). This phase is characterized by a regressive sedimentary wedge in the GSB (Carter, 1988), but no tectonic deformation in the study area.

**Fault analysis methodology**

The Great South basin 3D seismic survey was used for the analysis of the polygonal faults within the GSB. This 3D seismic survey acquired by ExxonMobil is a post-stack time migrated volume. Although there are no wells located within the 3D seismic survey, a few wells (e.g. Pakaha-1 and Rakiura-1) are in nearby locations (Figure 4.1). The well data and 2D seismic lines connecting the well data to the 3D survey were used to identify the age and lithology of the units within which the fault systems developed. Schlumberger Petrel software was used for seismic display and interpretation.

Traditional methods of fault interpretation involve the integration of fault data from inlines, crosslines, and time slices. Although this method may yield reliable results, it is both time consuming and subject to errors in fault correlations from the different displays. More recent fault interpretation methods are based on 3D seismic image analysis (Hale, 2013; Wu and Hale, 2016; Qi et al., 2017; Wu et al., 2019). In this study, a fault enhancement and skeletonization processes (Qi et al., 2017, 2018) is applied to the 3D seismic data. The workflow (Figure 4.3) starts with the application of structure-oriented filtering on seismic amplitude data on the post-stack data. After filtering, the coherence attribute is computed. The coherence is then filtered by directional Laplacian of a Gaussian filter to produce volume estimates of the probability, dip magnitude and dip azimuth of faults. These attributes are then skeletonized to produce the skeletonized fault probability volume. The results are checked against the results of traditional fault interpretation methods.

Traditional approaches use seismic time slices combined with inline and cross line profiles to views the fault systems, and then interpret them primarily on the time slices. The workflow used in this study sharpens structural and stratigraphic discontinuities and smears the incoherent noise on coherence. As a result, the fault data can be reduced to 3-D point sets from which fault patches can be directly extracted. Furthermore, compared to the traditional coherence attributes (Marfurt et al., 1998), the skeletonized fault probability attribute eliminates the "stair-step effect" (Figure 4.4b) of the fault planes and presents them as more continuous planes (Figure 4.4c). In addition, other stratigraphic discontinuities are suppressed. The skeletonized fault probability volume is very suitable for the automatic fault extraction process as it displays sharper, smoother and more continuous faults. The ant-tracking based automatic fault extraction process (Pedersen et al., 2002) was used to produce 3D fault patches, so further analysis on the spatial orientation of the fault systems could be conducted.

**Polygonal fault patterns and orientations**

***Cross sections***

The polygonal fault system is confined to a wedge-shaped layer within the Rakiura Group (Figure 4.5). Two distinct faulted zones are identified: a northwest zone that is deposited on an underlying slope defined by the top of a progradational clastic wedge, and a SE zone located above an approximately flat base. Faulting within the NW zone is restricted to a thinner stratigraphic package, whereas that in the SE zone extends to a deeper level. The lithology of the units containing the fault system is predominantly shaly siltstones and marls (Morley et al, 2017).

On the crossline of the seismic amplitude data (Figure 4.5), the faults are planar normal faults forming rotational tilt blocks of opposite vergence. Conversion to the depth domain using the sequence average velocity of 2500m/s (Figure 4.6), enables an estimation of the displacement and the dip of the faults (Figure 4.7). The displacement on a single fault ranges from tens of meters to a hundred meters. Although the dip direction is variable, the dip angle is generally consistent at between 45° and 55° for all the faults. Rotation and folding of the hanging wall beds can be observed. The location of the largest displacement along the fault can be considered as the fault nucleation point (Barnett et al., 1987). In many cases, this coincides with high amplitude horizons in both zones.

Compared to the Central North Sea (Lonergan & Cartwright, 1999) and South China Sea (Chen et al., 2011), which are characterized by polygonal fault systems which developed in multiple stratigraphic tiers, the polygonal fault system in the Great South Basin formed in a single tier. The reason for the development of multiple tiers is the variation in the grain size, mud chemistry or compaction rate. For example, in the Faeroe-Shetland Basin, two tiers are separated by a thick submarine fan sand (Cartwright, 2011). In the GSB, a relatively homogeneous composition and compaction rate of the fine-grained sediments is present, resulting in the consistent dip angles of the polygonal faults.

***Map view***

The faults in the polygonal fault system form a complex network on a time slice through the skeletonized fault volume (Figure 4.8). The fault length ranges from a few hundred meters to thousands of meters. The planiform patterns of the fault system range from linear, rectangular, to polygonal shapes. Most intersections of the faults are orthogonal or nearly orthogonal. Even where the strikes of two faults are not perpendicular to each other, the

fault traces tend to curve in order to form an orthogonal intersection. A concentric curved pattern is observed in only one area in the southern part of the study area.

One of the characteristics of the fault map is that the fault strikes vary significantly. Rose diagrams are used to study the strikes and dips of the polygonal faults. Instead of using the traditional approach of constructing the rose diagrams from seismic time slices (Hansen et al. 2004; Sun et al. 2010), 3D polygonal fault planes were used to generate the rose diagrams. 3D fault patches in the PFS (Figure 4.7) were extracted based on the skeletonized fault probability attributes. The advantages of using 3D fault patches to generate are: (1) the dip directions of the faults are accessible; (2) linear features that might be misinterpreted as faults and located only on one time slice are avoided; and (3) the fault system is studied for the entire tier, rather than from a single slice in a 2D map.

Although the general pattern of the fault systems is polygonal, the fault strikes for the entire region (Figure 4.8b) show orientation preferences at 70° and 160°. Since these two preferred strikes are perpendicular to each other, fault dip directions (Figure 4.8c) present the same trends as the fault strikes. For faults striking 160°-340°, there appear to be an equal number of faults dipping towards ENE and faults dipping WSW. For faults striking 70°-250°, there appear to be more faults dipping SSE than NNW.

Lonergan & Cartwright (1999), Hansen et al. (2004) and Cartwright (2011) stated that regional geological structures could affect the fault orientations. Hansen et al. (2004) studied the interaction between tectonic faults and polygonal faults for a PFS in the Sable Sub-basin (Canadian Atlantic margin). They documented orthogonal intersections between polygonal faults and tectonic normal faults and related these to local stress perturbation around the primary fault set (Bai et al. 2002; Hansen et al. 2004).

In the GBS, there is no tectonic activity directly affecting the layer containing the PFS, because it is within the Eocene post-rift passive margin clastic wedge which is not cut by any tectonic faults. However, The TWT structure map of the top of the basement (Figure 4.9) shows major NE-SW trending rifting faults that define horst, graben and half graben structures which controlled the Late Cretaceous and Paleocene sedimentary evolution (ExxonMobil Exploration Company, 2010). The location of the 3D seismic survey (red polygon) is within a convergent transfer zone (Morley et al, 1990) between two major normal faults which are located at the Southwest and the East of the Pakaha Graben. The fault orientations within the transfer zone show distinct turning of the fault strikes. The orientation of the major faults is approximately NE which is compatible with the preferred orientation of the NE trend within the polygonal fault system (Figure 4.8b). Within the transfer zone, the fault trends turn sharply to very oblique orientations and also result in slope changes within the Pakaha graben. Sediments between the basement and the Eocene exhibit passive draping (Harding, 1984) over the basement highs. This draping may have resulted in the superimposition of the NE fault trend over the polygonal fault system within the Eocene units. The NW trend may possibly be related to slope changes normal to this trend, but this relationship is less certain and not discernible from the macroscopic fault trends.

A more important local control of polygonal fault patterns is related to the slope of the units underlying the layer containing the PFS. As indicated earlier, the layer bounding the PFS is a wedge thinning towards NNW, with the base sloping to the SE. The NW zone of faulting directly overlies the slope whereas the SE segment overlies a flatter base. A slope map of the base of the faulted units in the area shows that the slope also changes along

trend (Figure 4.10). The mapped surface shown in Figure 4.10 represents the base of the faulted unit in the NW fault zone. The faults within the SE fault zone extend deeper, but the base of that package is parallel to that underlying the NW zone, so the same map correctly depicts the slope change.

Three samples (red, blue and magenta boxes in Figure 4.11) with distinct fault planiform patterns were chosen to study the relationship between the slope and the PFS. 3D fault patches within each box were extracted based on the skeletonized fault probability results, and rose diagrams were generated using those fault patches.

Although all of these areas exhibit polygonal fault patterns, a preferred pattern of dominant faults is found in each case. In the area with the steepest slope (red box in Figure 4.10), the pattern is characterized by a strongly linear trend. The area with a relatively gentler slope shows a more rectangular pattern (blue box), whereas the area with almost no slope (magenta box) exhibits the most random pattern. The rose diagrams of the fault strikes within the boxes match the planiform patterns. The linear faults have preferred strikes of 55°. The rectangular faults have two dominant orthogonal trends of 65° and 155°. The random trends show faults trending at multiple orientations but also show preferred trends of NNW and ESE.

Olson et al. (2007) and Roberts (2014) used numerical modeling to investigate the influence of the horizontal stress anisotropy on fracture pattern geometry. Their results can also be used to study the initiation of high angle normal faults. They achieved the horizontal stress anisotropy by imposing different levels of strain on one of the side boundaries. Olson et al. (2007) applied differential horizontal strain to the simulations of layer confined fractures in sandstones. They observed that isotropic initial stress produced randomly

oriented fractures, but with mostly orthogonal intersections between intersecting fractures (Figure 4.12c). On the other hand, strong stress anisotropy resulted in a single fracture orientation (Figure 4.12a). The fractures are all parallel to the σhmax direction. Moderate stress anisotropy led to a "ladder pattern" as the later phase of fracturing is roughly orthogonal to the initial fracturing (Figure 4.9c). These results are consistent with the interpretation of orthogonal fracture pattern development illustrated by Bai et al. (2002). Similarly, Roberts (2014) induced anisotropy in the horizontal stresses during the deposition of chemically active layers. The results show that more faults align parallel to the σhmax as the anisotropy increases.

The slope changes the horizontally isotropic state of stress (σhmax = σhmin) (Cartwright, 2011), and the horizontal stress anisotropy affects the planiform geometry of polygonal faults. Since σhmax in the wedge is parallel to slope contours, it can be assumed that polygonal faults may have preferential strikes parallel to the slope contours.

A fourth pattern (green box in Figure 4.11) that alters the planiform pattern of the polygonal faults is a concentric circular to elliptical pattern observed in the southern part of the area. The peripheral faults in the pink box (Figure 4.11) display a unique concentric circular planiform geometry on the time sections of the skeletonized fault probability volume. These peripheral faults are bounding a broad circular structure within the sedimentary sequence that overlies a deeper dome-shaped structure, as indicated by serial time sections of seismic amplitude volume (Figure 4.13c), and the inline and crossline sections (Figure 4.13a,b).

We consider several past hypotheses that have been suggested for the formation of circular structures related to polygonal faults including (1) pock mark type features related

to fluid migration, (2) hydrocarbon-related diagenesis zones, (3) volcanic calderas formed by magma-reservoir evacuation, and (4) active forced folding due to igneous intrusions.

Circular features referred to as pockmarks are interpreted to be associated with polygonal faults (Cartwright et al., 2011). The topographic depression of the pockmark crater causes a stress anisotropy affecting the propagation of the polygonal faults (Cartwright, 2011). Gay (2004) described the pockmarks and related furrows as outlets of the conduits for fluids migrating from deeper levels. Radial polygonal faults are formed around the pockmarks resulting in a different planiform geometry than the concentric peripheral styles. The concave shape of the pockmark does not match the dome-shaped structure coring the peripheral faults.

Brien & Woods (1995) observed hydrocarbon-related diagenetic zones (HRDZs) in the 2D seismic lines of the Vulcan Sub-basin in the Timor Sea, which are related to present-day hydrocarbon seepage at the seafloor. HRDZs are typically located along major tectonic faults because they need faults which provide conduits for the migration path for the hydrocarbons. The signal to noise ratio of an HRDZ is typically low. In the Vulcan Sub-basin, the HRDZs are developed at a much shallower depth.

Circular collapse calderas are commonly formed at the summit of volcanoes (Clough et al., 1909) as a result of the evacuation of the magma reservoir. Concentric peripheral faults formed around calderas are either normal faults dipping towards the center of the caldera or reverse faults dipping outward (Walter & Troll, 2001; Gudmundsson, 2008).

In the Vøring and Møre basins, igneous intrusions and related hydrothermal vents have had a significant impact on deformation (Planke et al., 2005; Omosanya et al., 2017). Planke et al. (2005) observed active folding (draping) of overlying sequences above the

vent complexes on 2D seismic profiles. Omosanya et al. (2017) studied the folding generated by the emplacement of magma into pre-existing sedimentary rocks using high-resolution 3D seismic data over the same area and found radial faults surrounding the hydrothermal vent. Similar forced folds can be found in the northern South China Sea as well (Sun et al., 2014).

The peripheral concentric faults in the GSB are related to the emplacement of the domal structure in the core, which is interpreted as a volcanic-plutonic igneous complex. Although the lower parts of the Paleocene sequence appear to be intruded by the igneous body as indicated by the truncation of lower Paleocene reflectors, onlapping or erosional unconformities within the upper Paleocene strata suggest that a significant component of the emplacement occurred before the sequence bounding the PFS was deposited in the early Eocene. The draping of the Paleocene sequence on the SE side of the mound structure could be caused by the reactivation of the Cretaceous rift fault. Minor crustal movements and volcanism occurred in the GSB during the Paleocene (Korora-I) (Carter, 1988) (Figure 4.14), and may have resulted in local volcanism in Late Paleocene when the Cretaceous rift fault was reactivated. Sills related to the emplacement can be observed as high amplitude reflections in the seismic section. The seeping of the thermal fluid may have led to diagenetic alteration of the mound structure (Planke et al., 2005) as well as the layers surrounding it and developed anisotropic stresses around it.

The concentric geometry of the faults and the related domal shape of the igneous complex suggest a geometric relationship between the two. The outward dips of the faults suggest that they are not the result of active intrusions or caldera formation, which would result in radial or inward dipping fault geometries. The propagation of the domal geometry

of the sediments and the faults through the Paleocene and Eocene strata suggests active or passive draping of sediments above the igneous body. The Eocene sediments containing the PFS which are located high in the stratigraphic section likely developed in response to passive draping of the sediments.

**3D fault patterns**

A 3D fault model within a small area within the random fault zone was built (Figure 4.14). The model is complex and consists of 22 major faults and 3 horizons that were hand-picked based on the 3D seismic amplitude volume. The reason for using the 3D seismic amplitude volume instead of the fault probability volume is that stratigraphic horizons cannot be shown by the fault probability attributes. In the 3D view, fault planes are not completely planar, but the dip is fairly constant along the dip direction. Intersecting fault planes are perpendicular to each other, which is consistent with the map view observation on the skeletonized fault probability map.

On the interpreted horizons (Figure 4.14c,d,e), the displacement on the faults can be illustrated by the gaps between the hanging wall and footwall on each horizon. Colder colors on each horizon present lower elevation along that horizon. The central part is also the deepest and represents the hanging wall of multiple normal faults.

The displacement decreases laterally towards each end of the faults. Along the fault dip, comparing three marker horizons, it is apparent that the fault displacement gradually increases from the top horizon to the bottom one. Based on previous observations of the cross-section, the lowest horizon in this model has the maximum displacement and represents the fault nucleation horizon. The displacement decreases towards the top and bottom tip of each fault from the fault nucleation horizon.

**Origin of PFS**

The formation of polygonal fault systems has previously been attributed to gravity sliding, density inversion, syneresis, and diagenesis. A number of these mechanisms have been subsequently ruled out as the universal cause for the formation of PFS (Goulty, 2008; Cartwright, 2011).

The gravity sliding theory (Higgs & McClay, 1993; Clausen et al., 1999), relates the PFS to gravitational stresses resulting from sliding down a slope. Downslope gravitational stress produces a strong alignment of fault strikes perpendicular to the direction of sliding towards the depocenter, which is not the case for most PFS (Cartwright et al., 2003). Also, many of the PFS are observed on basin floors where regional dips are close to zero (Goulty, 2008).

Watterson et al. (2000) used density inversion theory as the genetic mechanism for the development of a PFS confined to an Early Cretaceous mudstone sequence in the Eromanga Basin, South Australia. The density inversion is created by the burial of the overpressured low-density layer by an overlying normally pressured sequence (Henriet et al., 1989; Watterson et al., 2000), and leads to folding and related fracturing of the sediments. Goulty (2008) suggested that gravitational instability which is a key state of the density inversion model is difficult to achieve even with strong tectonic stresses.

Syneresis is the spontaneous contraction of colloidal materials without evaporation (Brinker & Scherer, 1990). Cartwright and Dewhurst (1998) and Hansen et al. (2004) used the syneresis model as a genetic mechanism of the PFS. However, Goulty (2008) and Cartwright (2011) questioned the validity of the mechanism at burial depths exceeding a few tens of meters.

Shin et al. (2008) used numerical and experimental analyses to illustrate that stress changes induced by volumetric contraction through mineral-specific dissolution during regional diagenesis of sediments can lead to shear failure. Davies et al. (2009) specifically related the propagation of polygonal faults to biogenic silica diagenesis. Biogenic silica is a common component of mudstones (Schieber et al., 2000). In siliceous mudstones and marls, biogenic silica deposited as amorphous opal-A is thermally unstable and dissolves and reprecipitates as microcrystalline opal-CT, and eventually to quartz with increasing burial and temperature (Isaacs, 1982). The opal-A/CT transformation reduces the porosity and shrinks bulk rock volume. This diagenetically-driven volume reduction induces shear failure. Opal A/CT diagenesis has been adopted more widely as the genetic mechanism for the polygonal fault systems developed in many siliceous sediments. Guerin and Goldberg (1996) displayed well logs suggesting an increase of seismic P-wave velocity and density of the transition zone between opal-A and opal-CT. The results were further confirmed by Sanada et al. (2009) with laboratory tests of Horonobe siliceous rocks. Therefore, the transition causes an increase in the acoustic impedance, resulting in positive polarity and high amplitudes on seismic data (Davies et al., 2009).

In the Great South Basin, the closely spaced faults within the Eocene units are layer bounded and form a polygonal network of faults. The NW fault zone forms within a thinner stratigraphic section, whereas the SE fault zone extends to deeper levels. We postulate that the polygonal faults may have formed as result of volumetric changes associated with opal A - opal CT - Quartz transitions (Isaacs, 1982). Two high amplitude zones are observed within the seismic time section (Figure 4.5). The lower zone pinches out to the northwest and is marked by the largest fault displacements in the SE zone. The upper zone shows a

slight decrease in amplitude towards the SE. Variation in fault displacement in the NW zone is not as clear as in the SE zone.

This observation is compatible with the hypothesis that the biogenic silica diagenesis induced shear failure initiates polygonal faults. The two high amplitude layers may represent boundaries marked by a large amount of diagenesis along silica-rich zones, causing the high seismic amplitudes. Laterally, the depth of the maximum opal-A/CT transition changes from the NW to the SE. In the SE zone, the largest displacement is closer to the bottom tip of the faults, which also coincides with the high amplitude reflection zones. The variation in displacement is confirmed by the 3D structural model discussed earlier. As the horizon dims and pinches out onto the slope on the NW, the maximum opal-A/CT transition boundary in the NW zone forms at a shallower depth.

**Conclusions**

Advanced fault enhancement and skeletonization was applied to map fault patterns using 3D seismic data from the Great South Basin, New Zealand. The skeletonized fault probability data combined with the amplitude data were used to study the geometry and orientations of the polygonal faults in cross-section, planiform, and 3D space.

Fault dips are typically between 45° and 55°, with the displacement on a single fault ranging from tens of meters to a hundred meters. The fault displacement decreases along the fault length towards the tips.

The general pattern of faulting in the GSB is polygonal, with multiple sets of faults intersecting each other at high angles. Preferred NE and NW regional patterns may be related to passive draping of the sedimentary packages over a convergent transfer zone within the Cretaceous fault system.

Locally, the fault patterns are influenced by the slope of the underlying units, which cause different amounts of horizontal stress anisotropy within the faulted units. Areas with high slope are marked by strong stress anisotropy and linear trends, areas with moderate slope are marked by rectangular trends, whereas areas with no slopes are marked by random polygonal patterns. A local concentric fault pattern in the southern part of the study area is related to passive draping over a conical igneous complex.

The formation of the PFS in the GSB is most likely related to the diagenesis of the biogenic siliceous mudstone. The polygonal faults likely formed as result of volumetric changes associated with opal-A – opal-CT - Quartz transitions. The opal-A/CT transformation reduces the bulk rock volume and induces shear failure. The opal-A/CT transition zone varies in depth from the NW to the SE and is marked by zones of high seismic amplitudes related to the high silica content. The maximum displacements along faults are approximately at the high amplitude horizons corresponding to the opal-A/CT transition, which served as the nucleation points for the faults.

**Acknowledgements**

We would like to thank New Zealand Petroleum & Minerals for providing the seismic data and well data over the study area for research use. We also would like to thank Schlumberger Petrel and University of Oklahoma AASPI for providing the academic licenses to interpret the seismic data. Last but not the least, Joe Cartwright and Xinming Wu are thanked for reviewing the manuscript and making valuable suggestions.

## CHAPTER 4 FIGURES

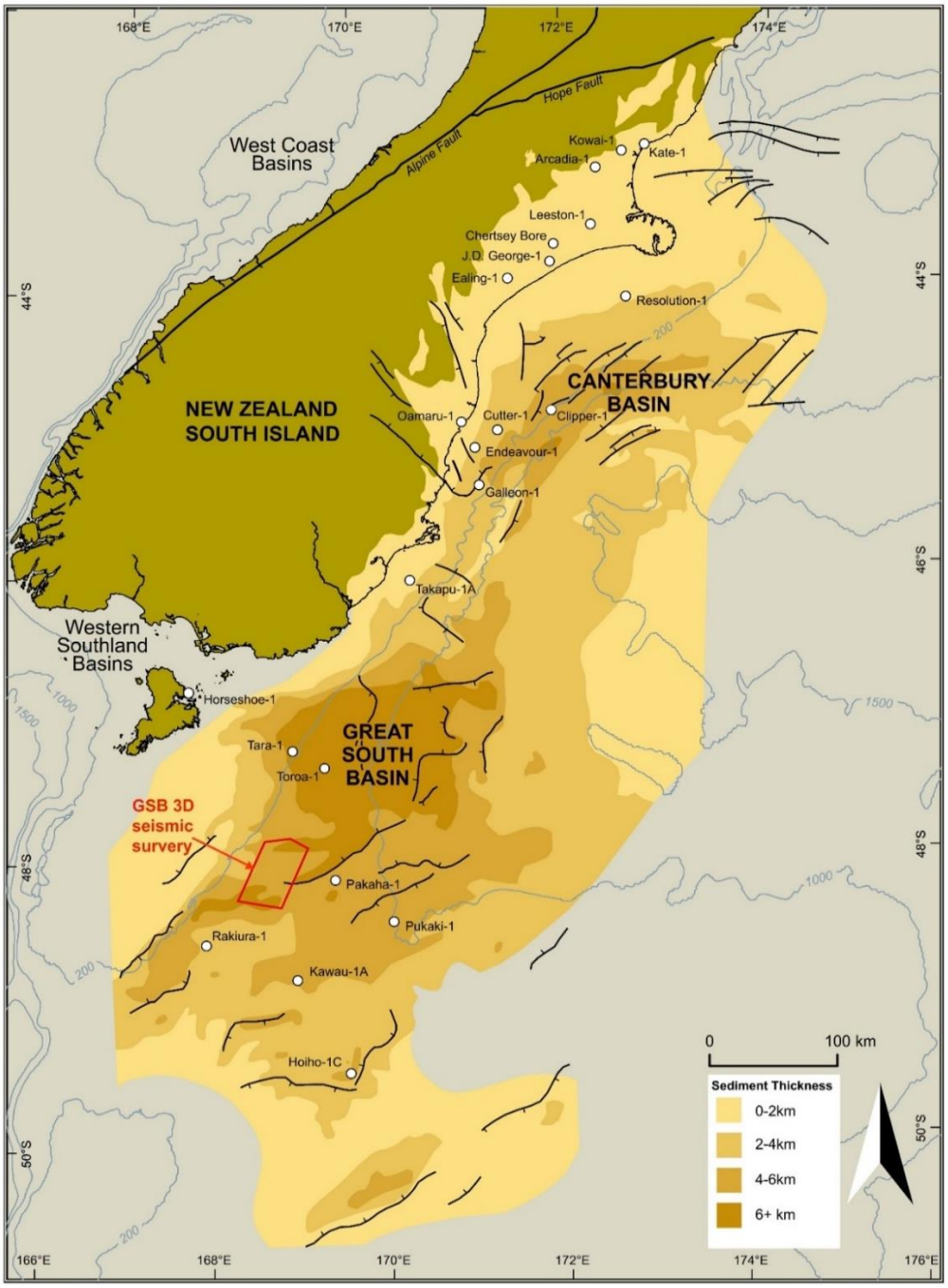


Figure 4.1. Map of the Great South Basin (GSB) showing the location of the 3D seismic survey (modified from New Zealand Petroleum & Minerals, 2014).

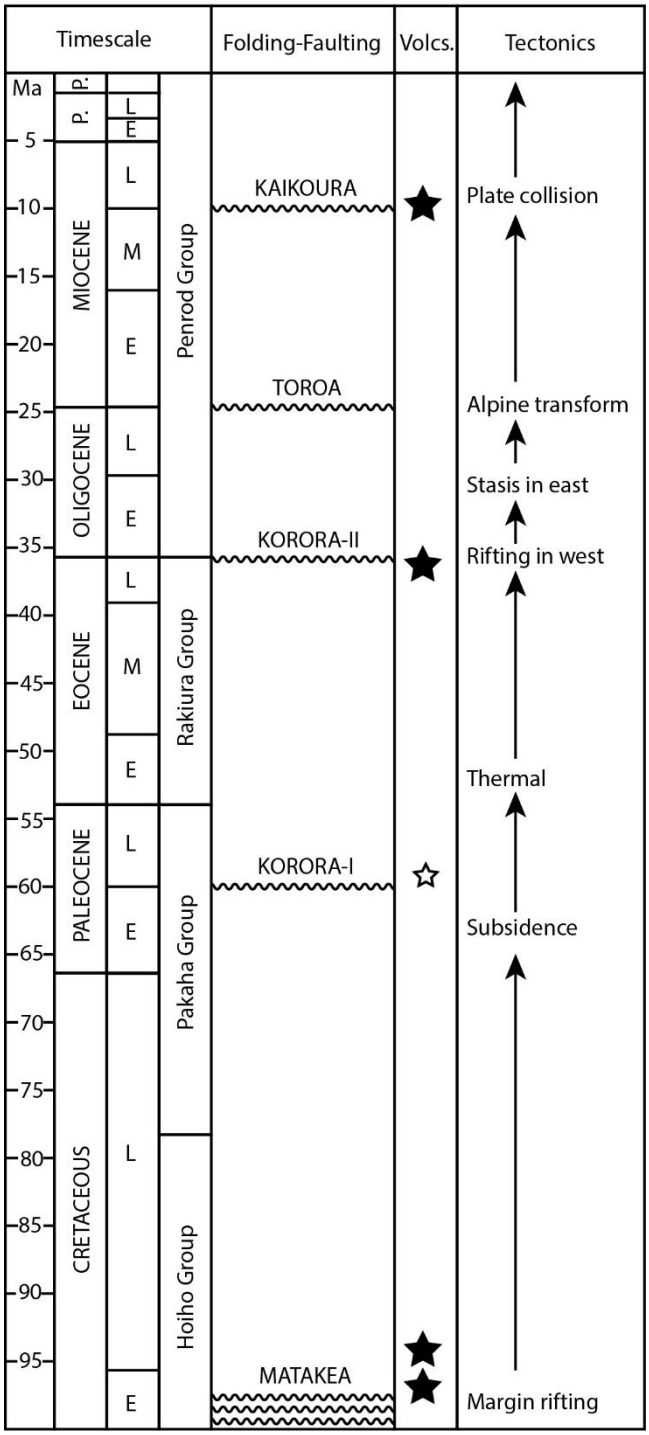


Figure 4.2. Stratigraphic column of GSB showing major stratigraphic units and tectonic events (modified from Carter, 1988 and Morley et al., 2017).

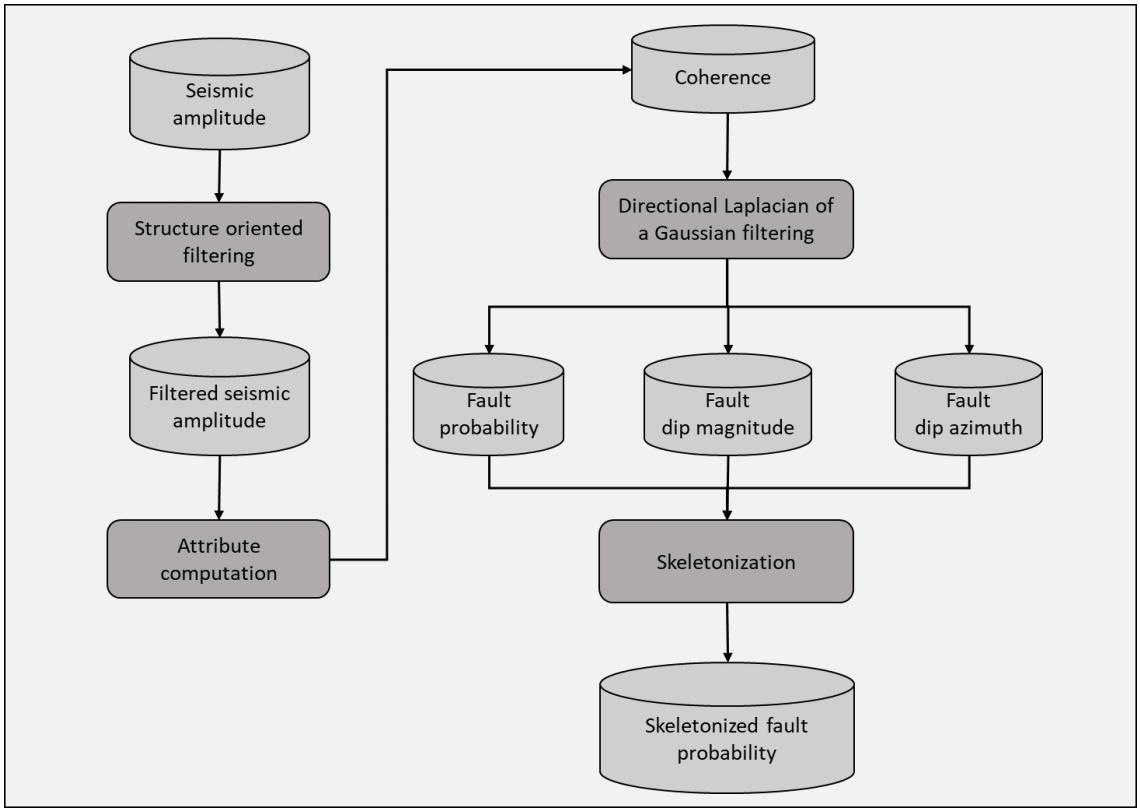


Figure 4.3. Fault enhancement and skeletonization workflow (modified from Qi et al., 2017). See text for further explanation.

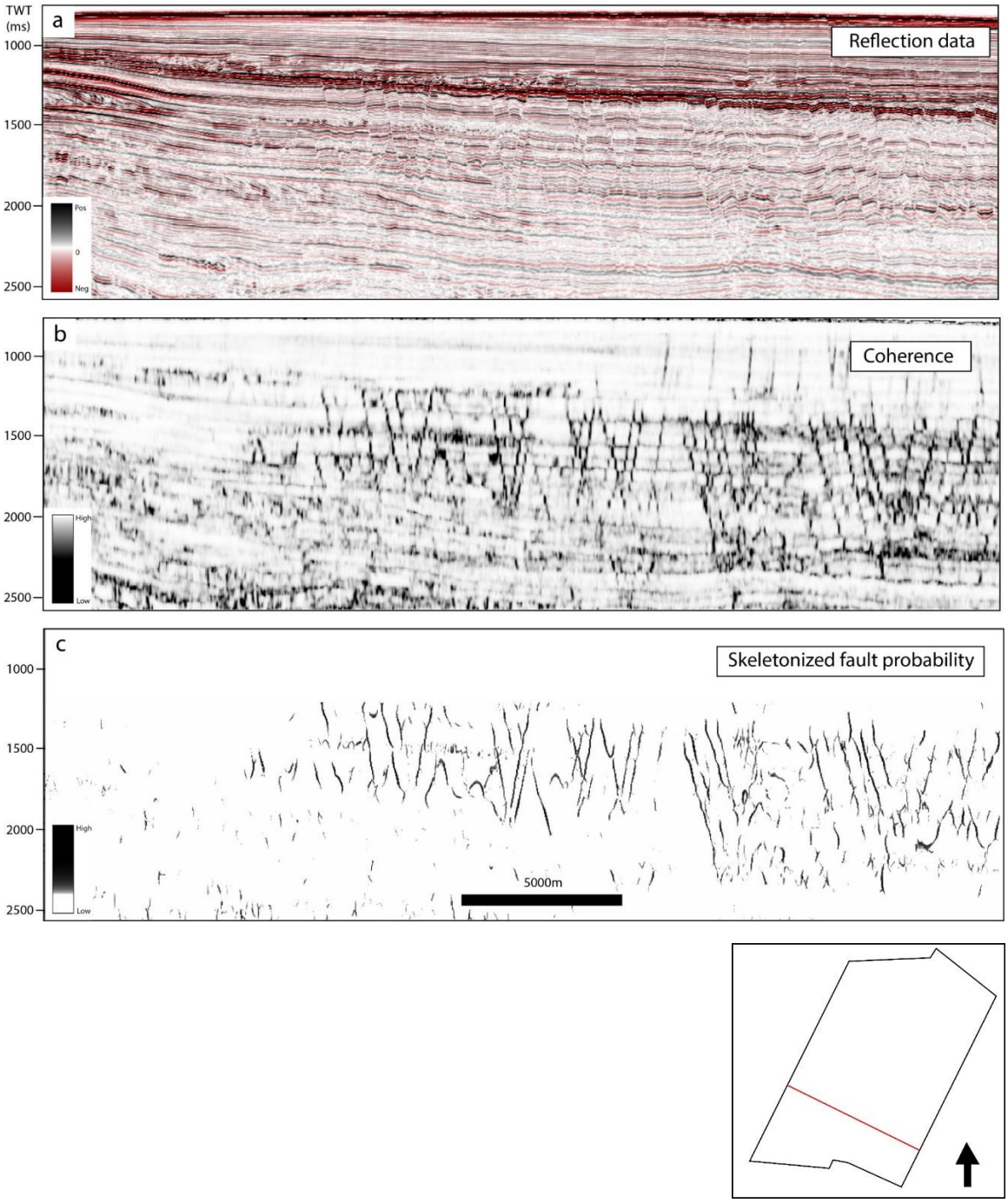


Figure 4.4. Vertical sections through (a) seismic amplitude, (b) original coherence, and (c) skeletonized fault probability volumes.

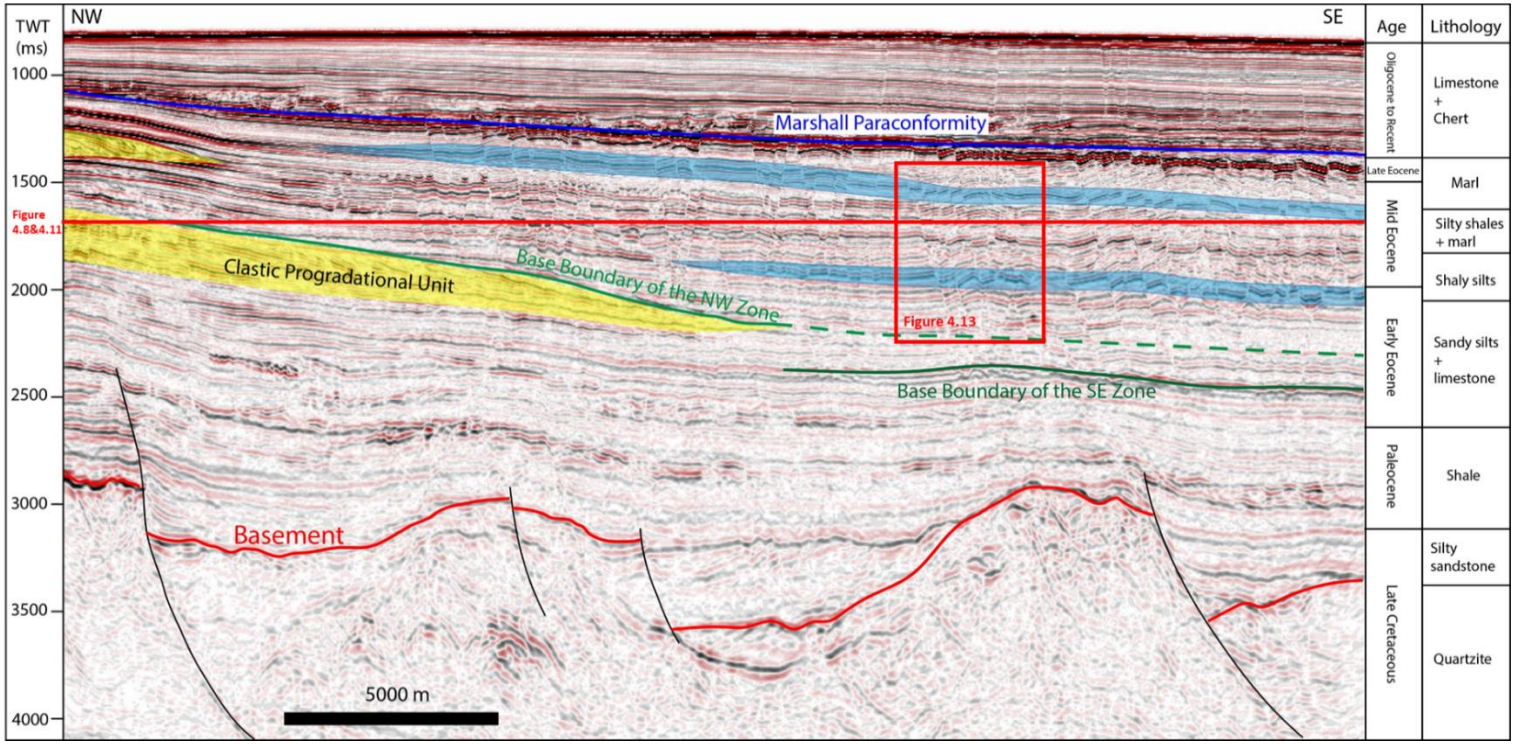


Figure 4.5. Seismic crossline section showing major structural and stratigraphic features in the GSB associated with elements associated the polygonal fault system. Dark blue = Marshall paraconformity. Green = Base boundary of the NW fault zone. Dark green = Base boundary of the SE fault zone. Red = top of the Cretaceous basement. Light blue = High amplitude reflections within the PFS, which may correspond to preferred locations of maximum opal-A/CT transition. Yellow = Clastic progradational unit. Age and lithology profiles are summarized from Pakaha-1 well tie and modified from Morley et al. (2017).

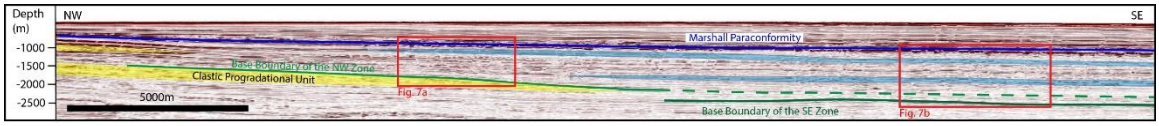


Figure 4.6. Seismic depth crossline derived from depth conversion of partial time profile in Figure 4.5 showing the polygonal fault systems in depth domain.

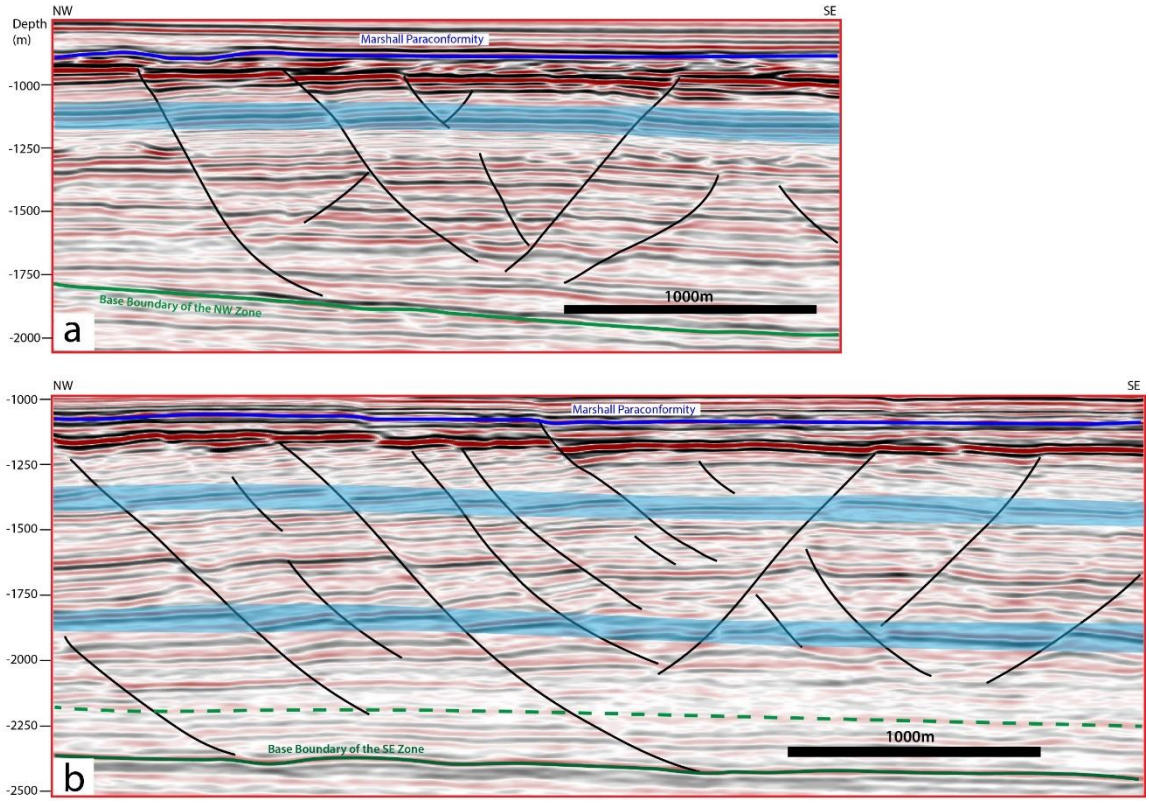


Figure 4.7. Interpretation of polygonal faults on seismic section (depth domain): (a) faults in the NW fault zone; (b) faults in the SE fault zone. See Figure 4.6 for locations.

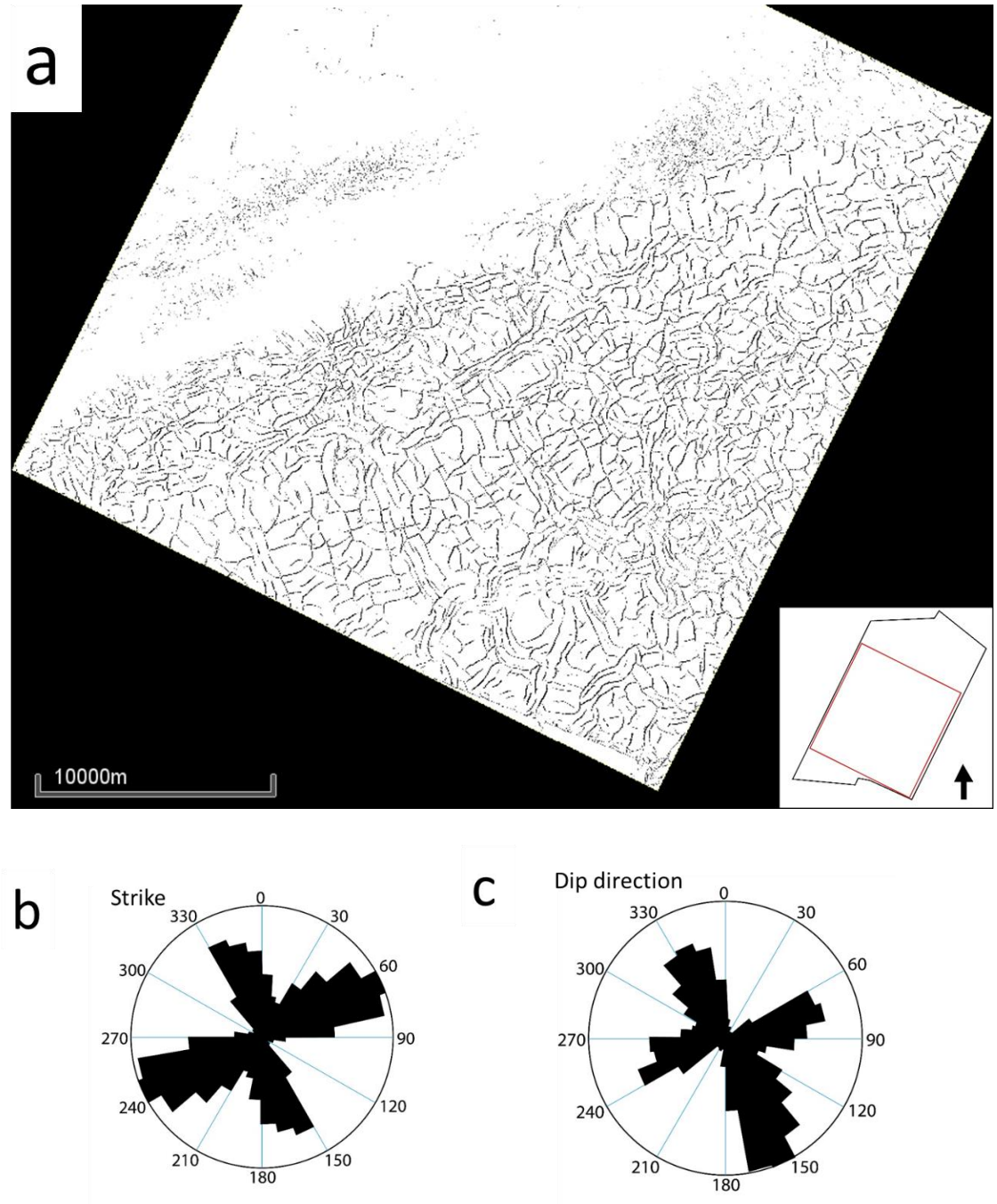


Figure 4.8. (a) The time slice (1656ms) through the skeletonized fault probability volume (see Figure 4.5 for location). (b) Rose diagram showing strikes of the polygonal faults in the study area. (c) Rose diagram showing dip directions of the polygonal faults in the study area.

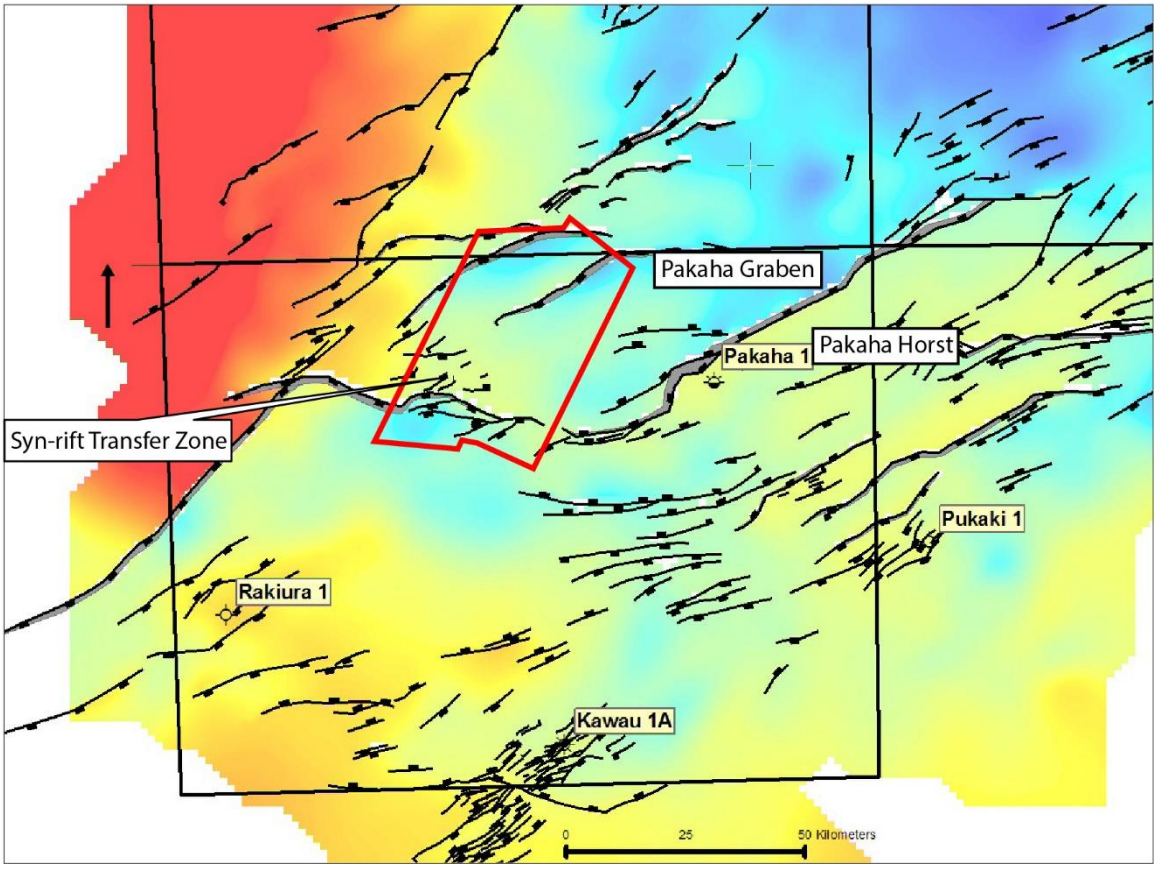


Figure 4.9. Structural elements map showing Pakaha Graben, convergent transfer Zone, Pakaha Horst, and the location of the GSB 3D seismic survey (modified from ExxonMobil Exploration Company, 2010).

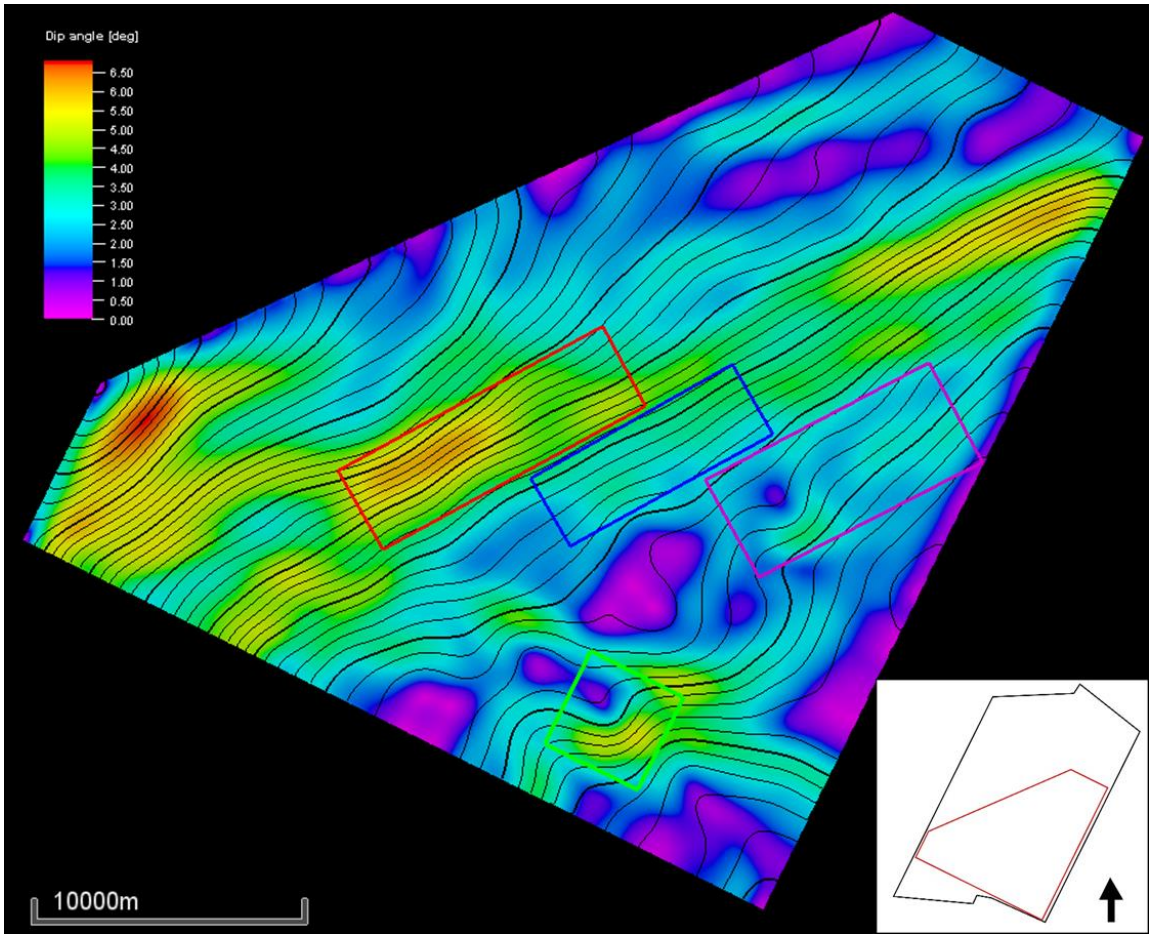


Figure 4.10. Slope map of the base boundary of the NW fault zone. See Figure 4.5 for location. The red box marks an area with relatively high slopes. The purple box bounds an area with relatively low slopes. The blue box bounds the area with intermediate slopes.

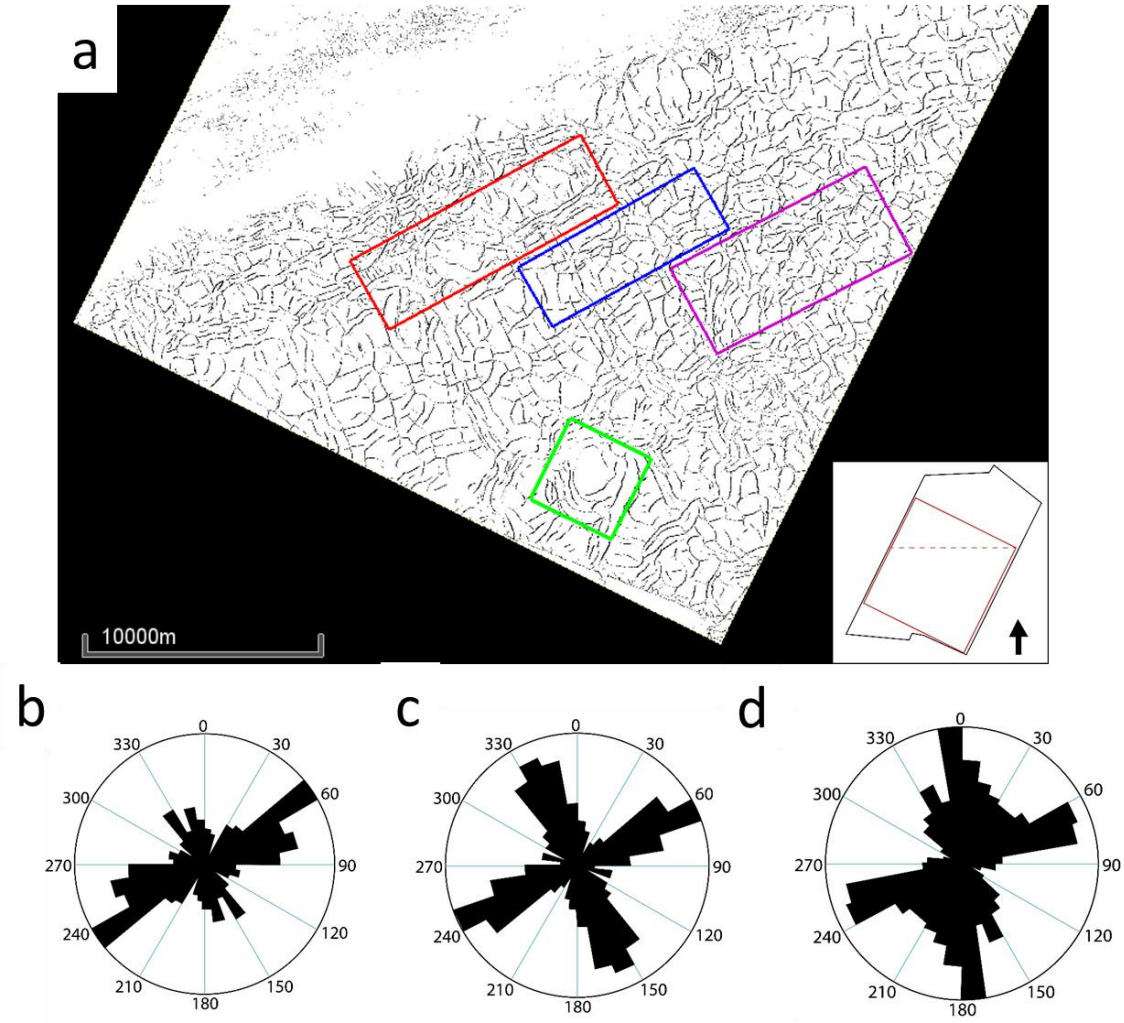


Figure 4.11. (a) The time slice (1656ms) through the skeletonized fault probability volume (see Figure 4.5 for location) showing three representative locations of different patterns: linear (red box), orthogonal (blue box), randomly oriented (purple box). The green box is showing the location of the peripheral faults. Rose diagrams (b-d)) of strikes of the faults in the red box, blue box, and purple box, respectively.

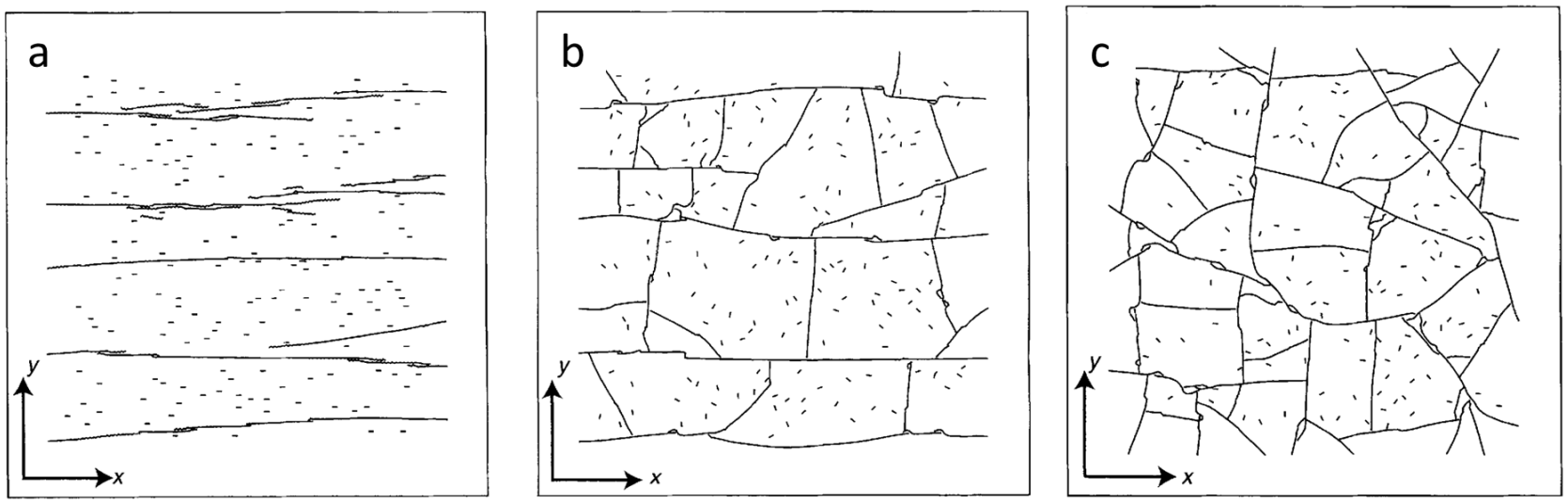


Figure 4.12. Modeled fracture patterns generated under (a) strong initial horizontal stress anisotropy, (b) moderate initial horizontal stress anisotropy, and (c) isotropic initial horizontal stresses (modified from Olson et al., 2007).

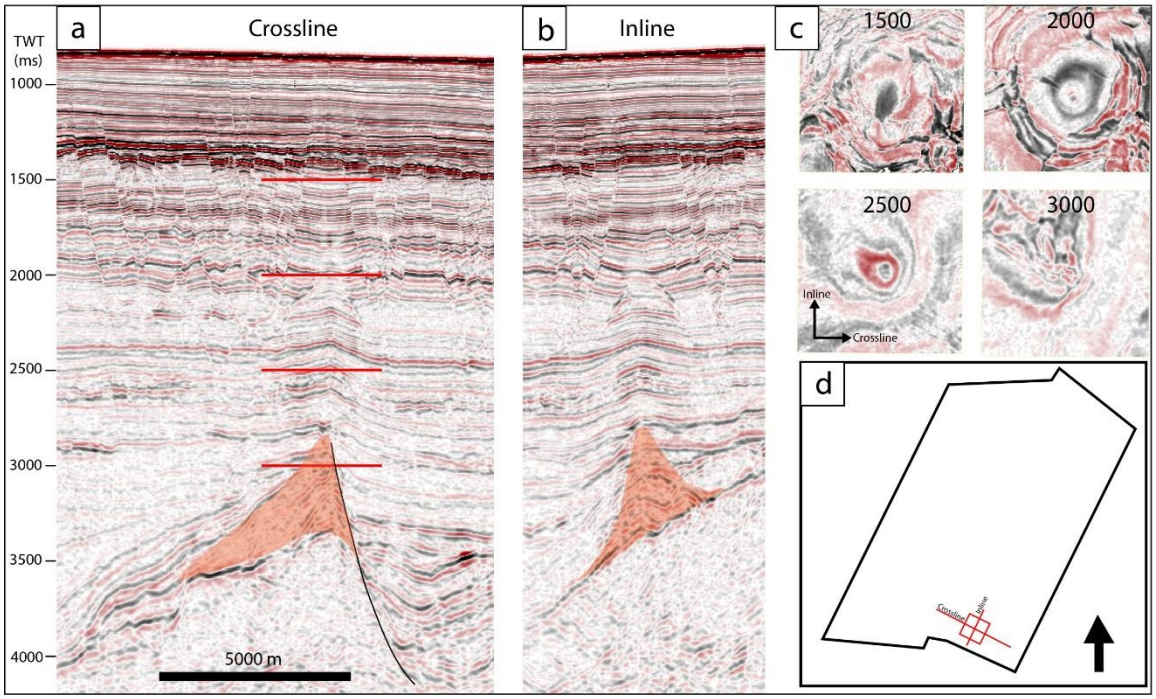


Figure 4.13. (a) The crossline seismic profile crossing the igneous complex (orange). (b) The inline seismic profile crossing the igneous complex. (c) Four time slices of the igneous feature at different depths. See (a) for the location. (d) Index map showing the location of the time sections and time slices.

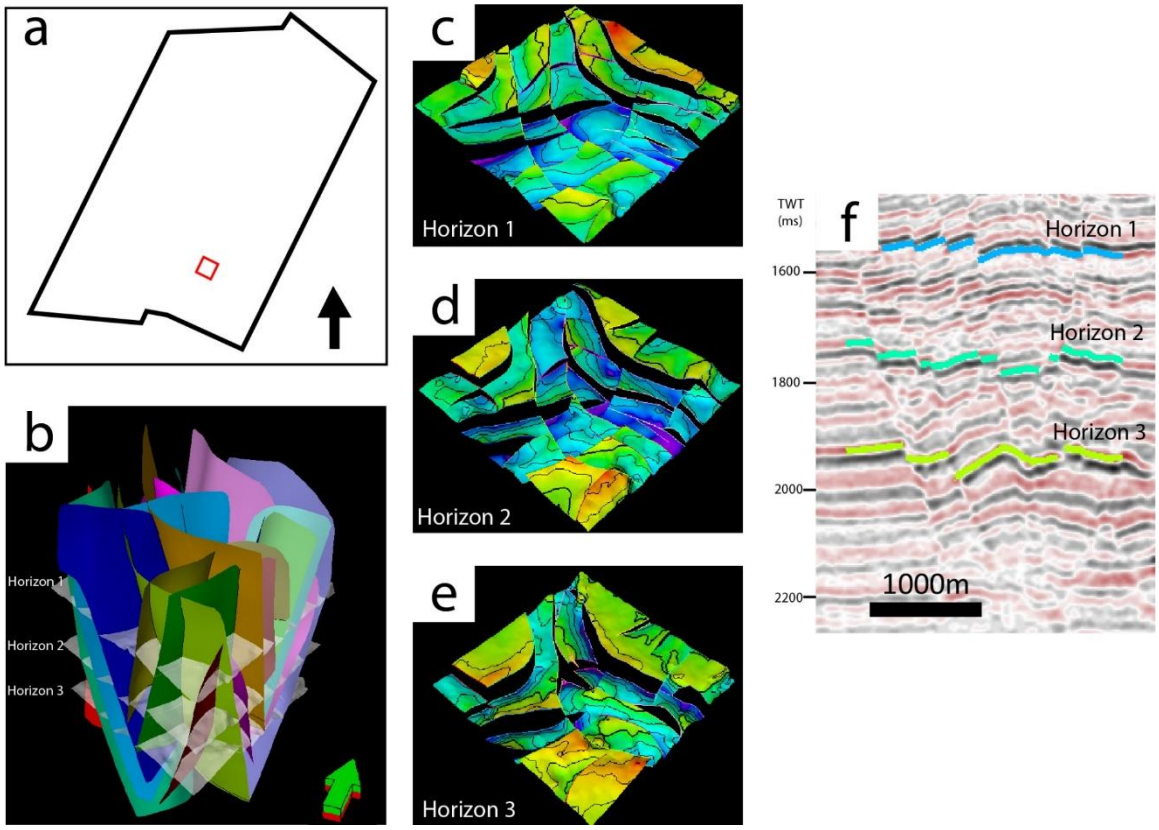


Figure 4.14. 3D structural model of the polygonal faults in a selected area. (a) Map showing the location of the model. (b) The 3D structural model including the faults and three horizons. (c) Horizon 1 fault patterns. (d) Horizon 2 fault patterns. (e) Horizon 3 fault patterns. (f) The locations of the horizons on seismic section. See Figure 4.5 for location.

## REFERENCES


Bai, T., Maerten, L., Gross, M. R., & Aydin, A. (2002). Orthogonal cross joints: do they imply a regional stress rotation?. Journal of Structural Geology, 24(1), 77-88.

Barnett, J. A., Mortimer, J., Rippon, J. H., Walsh, J. J., & Watterson, J. (1987). Displacement geometry in the volume containing a single normal fault. AAPG Bulletin, 71(8), 925-937.

Carter, R. M. (1988). Post-breakup stratigraphy of the Kaikoura Synthem (Cretaceous-Cenozoic), continental margin, southeastern New Zealand. New Zealand journal of geology and geophysics, 31(4), 405-429.

Cartwright, J. T., & Dewhurst, D. N. (1998). Layer-bound compaction faults in fine-grained sediments. Geological Society of America Bulletin, 110(10), 1242-1257.

Cartwright, J., James, D., & Bolton, A. (2003). The genesis of polygonal fault systems: a review. Geological Society, London, Special Publications, 216(1), 223-243.

Cartwright, J. (2011). Diagenetically induced shear failure of fine-grained sediments and the development of polygonal fault systems. Marine and Petroleum Geology, 28(9), 1593-1610.

Chen, D., Wu, S., Wang, X., & Lv, F. (2011). Seismic expression of polygonal faults and its impact on fluid flow migration for gas hydrates formation in deep water of the South China Sea. Journal of Geological Research, 2011.

Clausen, J. A., Gabrielsen, R. H., Reksnes, P. A., & Nysaether, E. (1999). Development of intraformational (Oligocene–Miocene) faults in the northern North Sea: influence of remote stresses and doming of Fennoscandia. Journal of Structural Geology, 21(10), 1457-1475.

Clough, C. T., Maufe, H. B., & Bailey, E. B. (1909). The cauldron-subsidence of Glen Coe, and the associated igneous phenomena. Quarterly Journal of the Geological Society, 65(1-4), 611-678.

Davies, R. J., Ireland, M. T., & Cartwright, J. A. (2009). Differential compaction due to the irregular topology of a diagenetic reaction boundary: a new mechanism for the formation of polygonal faults. Basin Research, 21(3), 354-359.

ExxonMobil Exploration Company (2010) Great South Basin 3D/2D seismic interpretation report, PEP 50117, Ministry of Economic Development New Zealand Unpublished Petroleum Report PR4233.

Gay, A., Lopez, M., Cochonat, P., & Sermondadez, G. (2004). Polygonal faults-furrows system related to early stages of compaction-upper Miocene to recent sediments of the Lower Congo Basin. Basin Research, 16(1), 101-116.

Ghisetti, F. / OMV New Zealand Ltd (2010) Seismic interpretation, prospects and structural Analysis, Great South Basin, Ministry of Economic Development New Zealand Unpublished Petroleum Report PR4173.

Goulty, N. R. (2008). Geomechanics of polygonal fault systems: a review. Petroleum Geoscience, 14(4), 389-397.

Gudmundsson, A. (2008). Magma-chamber geometry, fluid transport, local stresses and rock behaviour during collapse caldera formation. Developments in Volcanology, 10, 313-349.

Guerin, G., & Goldberg, D. (1996). Acoustic and elastic properties of calcareous sediments across a siliceous diagenetic front on the eastern US continental slope. Geophysical Research Letters, 23(19), 2697-2700.

Hale, D. (2013). Methods to compute fault images, extract fault surfaces, and estimate fault throws from 3D seismic images. Geophysics, 78(2), O33-O43.

Hansen, D. M., Shimeld, J. W., Williamson, M. A., & Lykke-Andersen, H. (2004). Development of a major polygonal fault system in Upper Cretaceous chalk and Cenozoic mudrocks of the Sable Subbasin, Canadian Atlantic margin. Marine and Petroleum Geology, 21(9), 1205-1219.

Harding, T. P. (1984). Graben hydrocarbon occurrences and structural style. AAPG Bulletin, 68(3), 333-362.

Hayes, D. E., & Ringis, J. (1973). Seafloor spreading in the Tasman Sea. Nature, 243(5408), 454.

Henriet, J. P., De Batist, M., Van Vaerenbergh, W., & Verschuren, M. (1988). Seismic facies and clay tectonic features of the Ypresian clay in the southern North Sea. Bulletin van de Belgische Vereniging voor Geologie, 97, 457-472.

Higgs, W. G., & McClay, K. R. (1993). Analogue sandbox modelling of Miocene extensional faulting in the Outer Moray Firth. Geological Society, London, Special Publications, 71(1), 141-162.

Isaacs, C. M. (1982). Influence of rock composition on kinetics of silica phase changes in the Monterey Formation, Santa Barbara area, California. Geology, 10(6), 304-308.

Jeffrey Brinker, C., & Scherer, G. W. (1990). Sol-gel science: the physics and chemistry of sol-gel processing. San Diego: Academic Press, CA, 1-97.

Killops, S. D., Hollis, C. J., Morgans, H. E. G., Sutherland, R., Field, B. D., & Leckie, D. A. (2000). Paleoceanographic significance of Late Paleocene dysaerobia at the

shelf/slope break around New Zealand. Palaeogeography, palaeoclimatology, palaeoecology, 156(1-2), 51-70.

Lonergan, L., & Cartwright, J. A. (1999). Polygonal faults and their influence on deep-water sandstone reservoir geometries, Alba Field, United Kingdom central North Sea. AAPG bulletin, 83(3), 410-432.

Marfurt, K. J., Kirlin, R. L., Farmer, S. L., & Bahorich, M. S. (1998). 3-D seismic attributes using a semblance-based coherency algorithm. Geophysics, 63(4), 1150-1165.

Molnar, P., Atwater, T., Mammerickx, J., & Smith, S. M. (1975). Magnetic anomalies, bathymetry and the tectonic evolution of the South Pacific since the Late Cretaceous. Geophysical Journal International, 40(3), 383-420.

Morley, C. K., Nelson, R. A., Patton, T. L., & Munn, S. G. (1990). Transfer zones in the East African rift system and their relevance to hydrocarbon exploration in rifts (1). AAPG Bulletin, 74(8), 1234-1253.

Morley, C. K., Maczak, A., Rungprom, T., Ghosh, J., Cartwright, J. A., Bertoni, C., & Panpichityota, N. (2017). New style of honeycomb structures revealed on 3D seismic data indicate widespread diagenesis offshore Great South Basin, New Zealand. Marine and Petroleum Geology, 86, 140-154.

O'Brien, G. W., & Woods, E. P. (1995). Hydrocarbon-related diagenetic zones (HRDZs) in the Vulcan Sub-basin, Timor Sea: recognition and exploration implications. The APPEA Journal, 35(1), 220-252.

Olson, J. E., Laubach, S. E., & Lander, R. H. (2007). Combining diagenesis and mechanics to quantify fracture aperture distributions and fracture pattern permeability. Geological Society, London, Special Publications, 270(1), 101-116.

Omosanya, K. O., Johansen, S. E., Eruteya, O. E., & Waldmann, N. (2017). Forced folding and complex overburden deformation associated with magmatic intrusion in the Vøring Basin, offshore Norway. Tectonophysics, 706, 14-34.

Pedersen, S. I., Randen, T., Sonneland, L., & Steen, Ø. (2002). Automatic fault extraction using artificial ants. In SEG Technical Program Expanded Abstracts 2002 (pp. 512-515). Society of Exploration Geophysicists.

Planke, S., Rasmussen, T., Rey, S. S., & Myklebust, R. (2005, January). Seismic characteristics and distribution of volcanic intrusions and hydrothermal vent complexes in the Vøring and Møre basins. In Geological Society, London, Petroleum Geology Conference series (Vol. 6, No. 1, pp. 833-844). Geological Society of London.

Qi, J., Lyu, B., AlAli, A., Machado, G., Hu, Y., & Marfurt, K. (2018). Image processing of seismic attributes for automatic fault extraction. Geophysics, 84(1), O25-O37.

Qi, J., Machado, G., & Marfurt, K. (2017). A workflow to skeletonize faults and stratigraphic features. Geophysics, 82(4), O57-O70.

Roberts, D. T. (2014). A geomechanical analysis of the formation and evolution of Polygonal Fault Systems (Doctoral dissertation, Cardiff University).

Sanada, H., Niunoya, S., Matsui, H., & Fujii, Y. (2009). Influences of sedimentary history on the mechanical properties and microscopic structure change of Horonobe siliceous rocks. Journal of MMIJ, 125(10_11), 521-529.

Schieber, J., Krinsley, D., & Riciputi, L. (2000). Diagenetic origin of quartz silt in mudstones and implications for silica cycling. Nature, 406(6799), 981.

Shin, H., Santamarina, J. C., & Cartwright, J. A. (2008). Contraction-driven shear failure in compacting uncemented sediments. Geology, 36(12), 931-934.

Sun, Q., Wu, S., Lü, F., & Yuan, S. (2010). Polygonal faults and their implications for hydrocarbon reservoirs in the southern Qiongdongnan Basin, South China Sea. Journal of Asian Earth Sciences, 39(5), 470-479.

Sun, Q., Wu, S., Cartwright, J., Wang, S., Lu, Y., Chen, D., & Dong, D. (2014). Neogene igneous intrusions in the northern South China Sea: Evidence from high-resolution three dimensional seismic data. Marine and Petroleum Geology, 54, 83-95.

Walter, T. R., & Troll, V. R. (2001). Formation of caldera periphery faults: an experimental study. Bulletin of Volcanology, 63(2-3), 191.

Watterson, J., Walsh, J., Nicol, A., Nell, P. A. R., & Bretan, P. G. (2000). Geometry and origin of a polygonal fault system. Journal of the Geological Society, 157(1), 151-162.

Wu, X., & Hale, D. (2016). 3D seismic image processing for faults. Geophysics, 81(2), IM1-IM11.

Wu, X., Shi, Y., Fomel, S., Liang, L., Zhang, Q., & Yusifov, A. Z. (2019). FaultNet3D: Predicting Fault Probabilities, Strikes, and Dips with a Single Convolutional Neural Network. IEEE Transactions on Geoscience and Remote Sensing.

# CHAPTER 5: SUMMARY

Chapter 2 and Chapter 3 systematically studied the seismic appearance of the common fold-thrust structures. Seismic modeling followed by pre-stack time migration (PSTM) is a good method to build synthetic seismic of those structures and study the pitfalls and artifacts associated with the PSTM seismic data. Listed below are some of the key takeaways from Chapter 2 and Chapter 3.

1. Be careful when observing "structures" below the fold-thrust structures for PSTM seismic data. Those "structures" can be artifacts that are caused by lateral velocity variances. For fault-bend folds, there might be anticlinal "pull-ups" under the crest. In terms of fault-propagation folds, the "pull-ups" can be more dramatic and forming normal-fault-like steps under the front limb. For detachment folds, the "pull-ups" and "push-downs" are directly related to the thickness of the ductile unit, therefore identifying the repetitive correlation between the fake structures and the ductile unit thickness is the key to differentiate the artifacts from the real structures.

2. For steep limbs of fold-thrust structures, bands of low-reflectivity can be observed together with the thrust-fault-like dislocations of the limbs. Those low-reflectivity bands might alternatively be interpreted as thrust faults or pure steep limbs and kink bands. In real seismic, traces of fault planes would help solidify the thrust fault interpretation, otherwise, steep-limb causes are highly possible.

3. One of the experiences we acquired from detachment fold models is that a quick seismic velocity comparison between the ductile unit and the shallow uneroded strata can help predict the possible "pull-up" or "push-down" artifacts. We used this trick to estimate the seismic velocity of the Salina Group underneath the Appalachian Plateau. This method

can be used to other cases as well to perform an early-stage quality control on the interpretation.

4. Base on the velocity error analysis, we can conclude that the PSTM is very sensitive to the correctness of the stacking velocity. Normally, structural geologists only conduct structural interpretation on the migrated seismic data assuming the seismic data is correctly migrated. However, our models proved that a small amount of error in picking the stacking velocity can lead to different structural geometries. Therefore, good communication between seismic interpreters and seismic processors is necessary for a correct structural interpretation.

5. For future works, the effects of other migration parameters on the fold-thrust structures in the PSTM seismic data can be studied. In addition, lateral velocity anisotropy can be added into the velocity models to reproduce field structures better. For more complex fold-thrust structures in 3D, 3D seismic modeling can be conducted.

Chapter 4 presented a case-study applying an advanced fault detection attribute and fault extraction method. We observed two preferred orientations that are perpendicular to each other: NE and NW. These regional preferred orientations may be related to passive draping of the sedimentary packages over a convergent transfer zone within the Cretaceous fault system. In addition, the fault patterns are also influenced by the slope of the underlying units which induced horizontal stress anisotropy within the faulted units. The workflow of analyzing the polygonal fault patterns in this study can be applied to other complex fault systems as well.